Radio Science Bulletin

ISSN 1024-4530

INTERNATIONAL
UNION OF
RADIO SCIENCE

UNION
RADIO-SCIENTIFIQUE
INTERNATIONALE

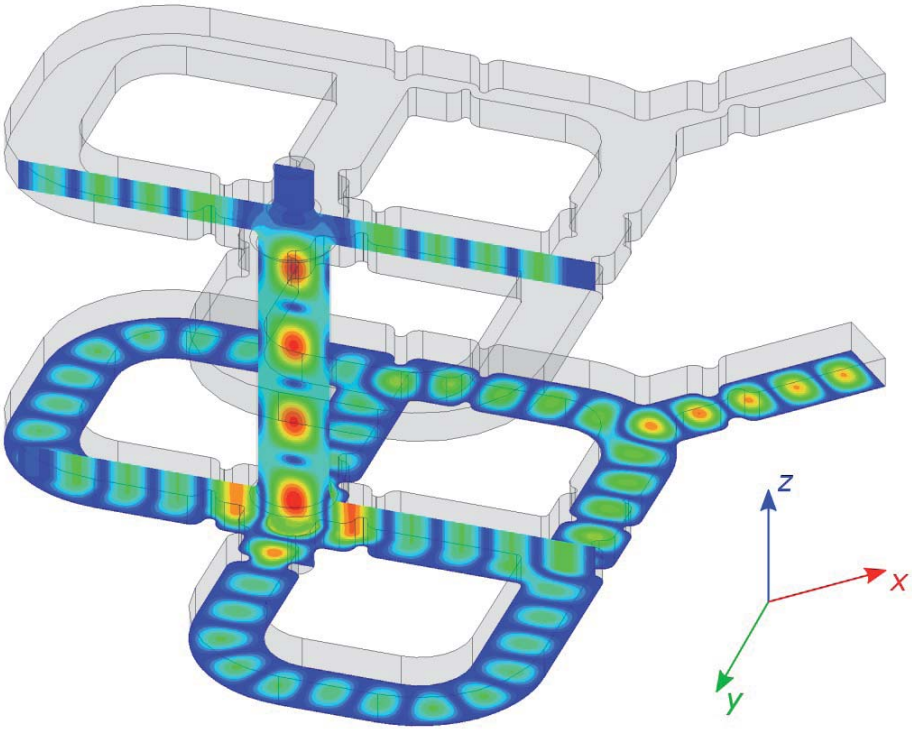

Vol. 2020, No. 373
June 2020

URSI, c/o Ghent University (INTEC)
Technologiepark - Zwijnaarde 126, B-9052 Gent (Belgium)

Contents

Radio Science Bulletin Staff 3
URSI Officers and Secretariat 6
Editor's Comments 8
Introduction to the Italian URSI Annual Meeting 10
2019 Young Scientist Best Paper Award Special Section 10
Phase-Controlled Beamforming Network Intended for Conformal Arrays 12
RF Design and Experimental Test of a Quadrupole-Free X-Band TM_{01} Mode Launcher 22
James Clerk Maxwell Foundation Newsletter Available 27
Electromagnetic Modeling of Scattered Signals of Opportunity: Challenges and Approaches 28
Perturbing the High-Latitude Upper Ionosphere (F Region) with Powerful HF Radio Waves: A 25-Year Collaboration with EISCAT 40
Radiation-Pattern Reconfigurable and Wideband Vector Antenna for 3-D Direction Finding 56
URSI GASS 2021 - Student Paper Competition 63
In Memoriam: Govind Swarup 64
Et Cetera 69
URSI GASS 2021 - Call for Papers 70
Book Review 71
URSI GASS 2021 - YSA Conditions 75
Announcement Commission E Corner in RSB 76
Historical Corner Column 77
The Electrostatic Foundation of the Electrocardiogram 78
An Unexpected Mossotti: His Formula at the Basis of Dielectrophoresis in Modern Molecular Biology 83
Telecommunications Health and Safety 86
European School of Antennas 2021 84
Women in Radio Science 90
Report on Italian URSI Annual Meeting 2019 and IEEE RFID-TA 2019 92
URSI Conference Calendar 96
Information for Authors 97
Become An Individual Member of URSI 98

Cover: A three-dimensional model of the back-to-back structure of an X band power coupler that converts the input rectangular mode into a circular mode for use with a particle accelerator. The simulated electric field of the two mode-launcher arms as well as the central circular waveguide section are visible. See the paper by G. Torrisi, G. S. Mauro, G. Sorbello, G. Castorina, L. Celona, L. Faillace, B. Spataro, and V. Dolgashev.

The International Union of Radio Science (URSI) is a foundation Union (1919) of the International Council of Scientific Unions as direct and immediate successor of the Commission Internationale de Télégraphie Sans Fil which dates from 1914.

Unless marked otherwise, all material in this issue is under copyright © 2019 by Radio Science Press, Belgium, acting as agent and trustee for the International Union of Radio Science (URSI). All rights reserved. Radio science researchers and instructors are permitted to copy, for non-commercial use without fee and with credit to the source, material covered by such (URSI) copyright. Permission to use author-copyrighted material must be obtained from the authors concerned.
The articles published in the Radio Science Bulletin reflect the authors' opinions and are published as presented. Their inclusion in this publication does not necessarily constitute endorsement by the publisher.
Neither URSI, nor Radio Science Press, nor its contributors accept liability for errors or consequential damages.

Radio Science Bulletin Staff

Editor

W. R. Stone
Stoneware Limited
840 Armada Terrace
San Diego, CA 92106, USA
Tel: +1-619 222 1915, Fax: +1-619 222 1606
E-mail: r.stone@ieee.org

Editor-in-Chief

P. Van Daele
URSI Secretariat
Ghent University - INTEC
Technologiepark - Zwijnaarde 126
B-9052 Gent, BELGIUM
Tel: +32 9-264 33 20, Fax: +32 9-264 42 88
E-mail: Pet.VanDaele@UGent.be

Production Editor

I. Lievens
URSI Secretariat / Ghent University - INTEC
Technologiepark - Zwijnaarde 126
B-9052 Gent, BELGIUM
Tel: +32 9-264.33.20, Fax: +32 9-264.42.88
E-mail: ingeursi@ugent.be, info@ursi.org

Senior Associate Editors

A. Pellinen-Wannberg
Department of Physics
Umea University
BOX 812
SE-90187 Umea, SWEDEN
Tel: +46 90 786 74 92, Fax: +46 90 786 66 76
E-mail: asta.pellinen-wannberg@umu.se

O. Santolik
Institute of Atmospheric Physics
Academy of Sciences of the Czech Republic
Bocni II
1401, 141 31 Prague 4, CZECH REPUBLIC
Tel: +420 267 103 083, Fax +420 272 762 528
E-mail os@ufa.cas.cz, santolik@gmail.com

Associate Editors, Commissions

Commission A

Nuno Borges Carvalho
Instituto de Telecomunicaçoes
Universidade de Aveiro, Campus Universitario
3810-193 Aveiro, Portugal
Tel: +351 234377900, Fax: +351 234377901
E-mail: nbcarvalho@ua.pt

Pedro Miguel Cruz
Rua Sao Sebastiao
n34 Hab 33
4520-250 Santa Maria da Feira, Aveiro, PORTUGAL
Tel: +351 225898410
E-mail: pedro.cruz@controlar.pt

Tian Hong Loh
National Physical Laboratory
Hampton Road
Teddington TW11 0LW, United Kingdom
Tel: +44 020 8943 6508
E-mail: tian.loh@npl.co.uk

Nosherwan Shoaib
School of Electrical Engineering and Computer Science (SEECS)
National University of Sciences and Technology (NUST)
NUST Campus H-12, Islamabad, Pakistan
Tel: 051 90852561
E-mail: nosherwan.shoaib@seccs.edu.pk

Commission B

Andrea Michel
Department of Information Engineering
Università di Pisa
Pisa, Italy
E-mail: andrea.michel@iet.unipi.it

John Volakis
College of Engineering and Computing
Florida International University
10555 W. Flagler Street, EC2477
Miami, FL 33174, USA
Tel: +1 305 348 2807
E-mail: jvolakis@fiu.edu

Commission C

Yves Louet
CS 47601, SUPELEC
Avenue de Boulaie
F-35576 Cesson-Sévigné, France
Tel: +33 2 99 84 45 34, Fax: +33 2 99 84 45 99
E-mail: yves.louet@supelec.fr

Commission D

Naoki Shinohara
RISH
Kyoto University
Uji 611-0011, Japan
Tel: +81 774 38 3807 Fax: +81 774 31 8463
E-mail: shino@rish.kyoto-u.ac.jp

Commission E

Virginie Deniau
IFSTTAR
20. rue Elisée Reclus BP 70317
F-59666 Villeneuve d'Ascq Cedex, France
Tel: +33 03 20438991
E-mail: virginie.deniau@ifsttar.fr

Commission F

Haonan Chen
Earth System Research lab, Physical Sciences Division
NOAA
325 Broadway, Boulder, CO 80305, USA
Tel: +1 303 497 4616
E-mail: haonan.chen@noaa.gov

Tullio Tanzi
Télécom ParisTech - LabSoC, c/o EURECOM
Campus SophiaTech Les Templiers
450 route des Chappes 06410 Biot, FRANCE
Tel: +33 0 4 93008411, Fax: 33 0 493008200
E-mail: tullio.tanzi@telecom-paristech.fr

Commission G

Giorgiana De Franceschi
Dept. Arenonomy, Istituto Nazionale di Geofi sica e Vulcanology
Via di Vigna, Murata 605
00 143 Roma, Italy
Tel: +39 06 51860307, Fax: +39 06 51860397
E-mail: giorgiana.defranceschi@ingv.it

Commission H

Jyrki Manninen
Sodankylä Geophysical Observatory
Tähteläntie 62
FIN-99600 Sodanskylä, Finland
Tel: +358 400 151503, Fax +358 16 610248
E-mail: Jyrki.Manninen@oulo.fi

Commission J

Jacob W. Baars
Max Planck Institute for Radio Astronomy
Auf dem Hügel 69
53121 Bonn, Germany
Tel: +49 228 525303
E-mail: jacobbaars@arcor.de

Commission K

Kensuke Sasaki
Applied EM Research Institute
NICT
Koganei, Tokyo, Japan
E-mail: k_sasaki@nict.go.jp

Associate Editors, Columns

Book Reviews

G. Trichopoulos
Electrical, Computer & Energy Engineering ISTB4 555D
Arizona State University
781 E Terrace Road, Tempe, AZ, 85287 USA
Tel: +1 (614) 364-2090
E-mail: gtrichop@asu.edu

Historical Papers

J. D. Mathews
Communications and Space Sciences Lab (CSSL)
The Pennsylvania State University
323A, EE East
University Park, PA 16802-2707, USA
Tel: +1(814) 777-5875, Fax: +1 814 863 8457
E-mail: JDMathews@psu.edu

Et Cetera

T. Akgül
Dept. of Electronics and Communications Engineering
Telecommunications Division
Istanbul Technical University
80626 Maslak Istanbul, TURKEY
Tel: +90 212 285 3605, Fax: +90 212 285 3565
E-mail: tayfunakgul@itu.edu.tr.

Women in Radio Science

A. Pellinen-Wannberg
Department of Physics and Swedish Institute of Space Physics
Umeå University
S-90187 Umeå, Sweden
Tel: +46 90 786 7492
E-mail: asta.pellinen-wannberg@umu.se

Ethically Speaking

R. L. Haupt
Colorado School of Mines
Brown Building 249
1510 Illinois Street, Golden, CO 80401 USA
Tel: +1 (303) 273 3721
E-mail: rhaupt@mines.edu

A. J. Shockley
E-mail: aj4317@gmail.com

Solution Box

Ö. Ergül
Department of Electrical and Electronics Engineering
Middle East Technical University
TR-06800, Ankara, Turkey
E-mail: ozgur.ergul@eee.metu.edu.tr

Telecommunications Health & Safety

J. C. Lin
University of Illinois at Chicago
851 South Morgan Street, M/C 154
Chicago, IL 60607-7053 USA
Tel: +1 312 413 1052, Fax: +1 312 996 6465
E-mail: lin@uic.edu

Historical Column

G. Pelosi
Department of Information Engineering
University of Florence
Via di S. Marta, 3, 50139 Florence, Italy
E-mail: giuseppe.pelosi@unifi.it

Early Career Representative Column

S. J. Wijnholds
Netherlands Institute for Radio Astronomy
Oude Hoogeveensedijk 4
7991 PD Dwingeloo, The Netherlands
E-mail: wijnholds@astron.nl

Education Column

Madhu Chandra
Microwave Engineering and Electromagnetic Theory
Technische Universität Chemnitz
Reichenhainerstrasse 70
09126 Germany
E-mail: madhu.chandra@etit.tu-chemnitz.de

URSI Officers and Secretariat

Current Officers triennium 2017-2020

President

M. Ando
Senior Executive Director
National Institute of Technology
701-2, Higashi Asakawa, Hachioji,
Tokyo 193-0834, Japan
Tel:+81-42-662-3123,
Fax: +81-42-662-3131
E-mail: ando@kosen-k.go.jp,
mando@antenna.ee.titech.ac.jp

Vice President

O. Santolik
Institute of Atmospheric Physics
Electrical Eng. Dept
Academy of Sciences of the Czech Republic
Bocni II, 1401
141 31 Prague 4, CZECH REPUBLIC
Tel: +420 267 103 083
Fax: 420 272 762 528
E-mail: os@ufa.cas.cz, santolik@gmail.com

Past President

P. S. Cannon
Gisbert Kapp Building
University of Birmingham
Edgbaston , Birmingham, B15 2TT,
UNITED KINGDOM
Tel: +44 (0) 7990 564772
Fax: +44 (0)121 414 4323
E-mail: p.cannon@bham.ac.uk

Vice President

A. Sihvola
Electronic Science Department
Aalto University
School of Electrical Engineering
PO Box 13000
FI-00076 AALTO
FINLAND
Tel: +358 50 5871286
E-mail: Ari.Sihvola@aalto.fi

Secretary General

P. Van Daele
URSI Secretariat
Ghent University - INTEC
Technologiepark - Zwijnaarde 126
B-9052 Gent
BELGIUM
Tel: +32 9-264 33 20
Fax: +32 9-264 42 88
E-mail: Pet.VanDaele@UGent.be

Vice President

P. L. E. Uslenghi
Dept. of ECE (MC 154)
University of Illinois at Chicago 851
S. Morgan Street
Chicago, IL 60607-7053
USA
Tel: +1 312 996-6059
Fax: +1 312 996 8664
E-mail: uslenghi@uic.edu

Vice President

W. Baan
Astron
Asserweg 45
9411 LP Beilen
THE NETHERLANDS
Tel: +31 521-595 773/100
Fax: +31 521-595 101
E-mail: baan@astron.nl

URSI Secretariat

Secretary General

P. Van Daele
URSI Secretariat
Ghent University - INTEC
Technologiepark - Zwijnaarde 126
B-9052 Gent
BELGIUM
Tel: +32 9-264 33 20
Fax: +32 9-264 42 88
E-mail: Pet.VanDaele@UGent.be

Assistant Secretary General AP-RASC

K. Kobayashi
Dept. of Electr and Commun. Eng,
Chuo University
1-13-27 Kasuga, Bunkyo-ku
Tokyo, 112-8551, JAPAN
Tel: +81 3 3817 1846/69
Fax: +81 3 3817 1847
E-mail: kazuya@tamacc.chuo-u.ac.jp

Assistant Secretary General

Stefan J. Wijnholds
Netherlands Institute for
Radio Astronomy
Oude Hoogeveensedijk 4
7991 PD Dwingeloo
The Netherlands
E-mail: wijnholds@astron.nl

Executive Secretary

I. Heleu
URSI Secretariat
Ghent University - INTEC
Technologiepark - Zwijnaarde 126
B-9052 Gent
BELGIUM
Tel. +32 9-264.33.20
Fax +32 9-264.42.88
E-mail info@ursi.org

Assistant Secretary General Publications & GASS

W. R. Stone
840 Armada Terrace
San Diego, CA 92106
USA
Tel: +1-619 222 1915
Fax: +1-619 222 1606
E-mail: r.stone@ieee.org

Administrative Secretary

I. Lievens
URSI Secretariat
Ghent University - INTEC
Technologiepark - Zwijnaarde 126
B-9052 Gent
BELGIUM
Tel: +32 9-264.33.20
Fax: +32 9-264.42.88
E-mail: ingeursi@ugent.be

Editor's Comments

W. Ross Stone
Stoneware Limited
840 Armada Terrace
San Diego, CA 92106, USA
Tel: +1-619 222 1915, Fax: +1-619 222 1606
E-mail: r.stone@ieee.org

Special Section on the 2019 Italian URSI Annual Meeting Young Scientist Best Paper Awards

We have three invited papers from the 2019 Italian URSI annual meeting Young Scientist Best Paper Awards in this issue. The paper by Valentina Palazzi was the Best Paper Award winner. The papers by Giuseppe Torrisi and by Davide Comite received Honorary Mention. There is a separate introduction to the special section from the organizers of the annual meeting.

The paper by Valentina Palazzi describes a reconfigurable 1×4 network that provides beamforming for conformal arrays. Selection of the output ports is performed by controlling only the phase of four variable phase shifters. Either a single output port or pairs of adjacent output ports can be activated. Where a pair of output ports is activated, the phase relationship between the ports can be controlled. The beamforming network was implemented using a combination of variable phase shifters and a modified Butler-matrix circuit. A prototype built to operate in the frequency range of 3.4 GHz to 3.8 GHz was used to provide beamforming with an array of four antenna elements, each element located on one face of a cube. Eight beams, equally spaced in azimuth, were formed with maxima in their broadside directions, and an additional four equally spaced beams were formed with nulls in their broadside directions.

The paper by G. Torrisi, G. S. Mauro, G. Sorbello, G. Castorina, L. Celona, L. Faillace, B. Spataro, and V. Dolgashev presents the design and testing of a novel X-band power coupler that converts the input rectangular TE_{10} mode into a circular TM_{01} mode for use with a particle accelerator. The design of the coupler was carried out using an optimizing process involving simulations to minimize the quadrupole components of the structure. An experimental version of the coupler was fabricated by milling aluminum blocks, permitting low-power RF testing to be done. The results were quite good. An oxygen-free high-conductivity copper version of the device is being manufactured for high-power and ultra-high-vacuum tests that are planned to be conducted at the Stanford Linear Accelerator Center (SLAC).

The use of scattering from signals from the Global Navigation Satellite System (GNSS) as signals of opportunity in remote sensing is the topic of the paper by Davide Comite, Laura Dente, Leila Guerriero, and Nazzareno Pierdicca. The paper focuses on the work done at the Sapienza and Tor Vergata universities of Rome. The authors begin with a general explanation of how GNSS reflectometry can be used for remote sensing. They then provide a comprehensive overview of studies that have been carried out using this method. The variety of modeling approaches used to interpret the data are reviewed. A closed-form model based on coherent scattering, developed by the authors, is then explained. The characterization of the received power of the scattered signal including both the coherent and incoherent contributions is discussed. The correlations between the features of the scattered field and the parameters of the scattering surface are analyzed. Finally, upgrades to the Soil and Vegetation Reflection Simulator (*SAVERS*) are described. This paper provides an excellent introduction to the topic of the use of signals of opportunity for remote sensing.

Our Other Papers

In an invited paper, Nataly F. Blagoveshchenskaya brings us a review of 25 years of collaboration between the Arctic and Antarctic Research Institute (AARI) and the European Incoherent Scatter (EISCAT) Scientific Association on studies of high-latitude F-region heating of the ionosphere. Most of these experiments involved extraordinary (X-mode) HF pump waves. They resulted in many new phenomena being observed for the first time,

and these are reviewed in this paper. The author also shares her career in radio science with us in the Women in Radio Science column in this issue.

J. Duplouy, C. Morlaas, H. Aubert, P. Potier, and P. Pouliguen describe a novel antenna for direction finding over the three-dimensional upper half-space. The antenna covers a bandwidth from 1 GHz to 8.2 GHz, and is sensitive to both horizontally and vertically polarized electromagnetic fields. The antenna consists of three circular (or half-circular) arrays of Vivaldi antennas, arranged and connected in such a manner as to permit the measurement of all six Cartesian components of the incident electric and magnetic fields. The field measurements are derived from the received signals weighted by coefficients associated with the ability to reconfigure the radiation pattern of the antenna. The antenna is relatively compact, fitting within a half-sphere with a radius that is less than one-half wavelength at the lowest operating frequency. The results achieved by the antenna were impressive.

Our Other Contributions

George Trichopoulos has provided us with a review by Jacob Baars of the book *Open Skies: The National Radio Astronomy Observatory and its impact on US Radio Astronomy*. This is a fascinating book, and it is also a fascinating book review. The reviewer was associated with much of the history reported in the book, and his commentary is well worth reading. The book is available as a free downloadable electronic version, or in hard copy for a charge.

Tayfun Akgul has provided some timely commentaries on the coronavirus in cartoon form in his Et Cetera column.

Giuseppe Pelosi's Historical Corner has two contributions. The first, by Stefano Maddio, describes the development of the electrocardiogram by Willem Einthoven. The second contribution, by Federico Carpi, Stefano Maddio, and Benedetta Pelosi, presents some of the significant milestones in the history of dielectrophoresis.

Jim Lin's Telecommunications Health and Safety column examines the possibility of microwave radiation from radars producing spatial disorientation effects in military pilots. There is a new US Defense Advanced Research Projects Agency (DARPA) study that will deal with this topic.

Asta Pellinen Wannberg's Women in Radio Science column brings us some reflections from Nataly Blagoveshchenskaya on her career in radio science. This is a nice companion to Dr. Blagoveshchenskaya's paper in this same issue.

The New Year

This issue will reach most of our readers early in 2021. That makes it appropriate to remind readers that the URSI XXXIVth General Assembly and Scientific Symposium will be held August 28 - September 4, 2021, at the Sapienza Faculty of Engineering, Sapienza University, Rome, Italy. The deadline for paper submission is January 31, 2021. Further details can be found at www.URSI2021.org.

My very best wishes for a most happy, healthy, safe, and prosperous New Year!

Introduction to the Italian URSI Annual Meeting 2019 Young Scientist Best Paper Award Special Section

The Italian National URSI Committee Meeting was organized in Pisa on September 26, 2019, and collocated with the IEEE RFID-TA conference. It was attended by more than thirty researchers working in universities and research institutes. The 2019 Young Scientist Best Paper Award was organized by the URSI Italian National Committee for Young Scientists doing research on topics belonging to all of the URSI Commissions. It was financially supported by URSI.

To qualify for the award, the Young Scientist applicants were required to be less than 35 years old on September 15th, 2019. Applicants were also required to submit a paper three to four pages in length, of which the Young Scientist was the principal author.

A total of 11 Young Scientists applied for the Young Scientist Best Paper Award. Three papers were selected for the final session, which was centered on their presentations. The judging committee was composed of Dr. Giorgiana De Franceschi (URSI Commission G), Dr. Simonetta Paloscia (URSI Commission F), Prof Giuliano Manara (URSI Commission B), and Prof. Carlo Carobbi (URSI Commission E).

After careful consideration, the judging committee decided on the following ranking (see Figure 1):

Young Scientist Best Paper Award Winner
Valentina Palazzi (University of Perugia), "Phase-Controlled Beamforming Network Intended for Conformal Arrays"

Young Scientist Best Paper Award Honorary Mention
Giuseppe Torrisi (INFN-LNS), "RF Design and Experimental Test for a Quadrupole-Free X-Band TM01 Mode Launcher"

Davide Comite (Sapienza University of Rome), "Electromagnetic Modeling of Scattered Signals of Opportunity"

Figure 1a. Prof. Giuliano Manara (University of Pisa) (r) presented the 2019 Italian URSI National Meeting Young Scientist Best Paper Award to Dr. Valentina Palazzi.

Figure 1b. Prof. Manara (l) presented an Honorary Mention to Dr. Davide Comite.

Figure 1c. Prof. Manara (l) presented an Honorary Mention to Dr. Giuseppe Torrisi.

Figure 2a. Dr. Giorgiana De Franceschi and Prof. Carlo Carobbi announced the recipients of Honorary Mention to the participants to the Young Scientist Best Paper Award Poster Session.

Figure 2b. Juliana Garrido Damaceno, one of the Young Scientists who presented their posters in the special URSI Poster Session, on the stage with Prof. Giuliano Manara.

Figure 2c. Carolina Miozzi and Simone Nappi, two of the Young Scientists who presented their posters in the special URSI Poster Session, on the stage with Prof. Giuliano Manara.

Furthermore, due to the high quality of the submitted papers, the committee offered to the Young Scientists who did not have access to the finals the possibility of presenting a paper in an URSI Poster Session. They were also given certificates of participation by the Italian URSI National Committee. The certificates were delivered by Dr. Giorgiana De Franceschi and by Prof. Carlo Carobbi, as members of the judging committee of the 2019 Italian URSI Committee Young Scientist Best Paper Award (see Figure 2).

URSI Poster Session

Juliana Garrido Damaceno (Istituto Nazionale di Geofisica e Vulcanologia, INGV), "Improvement of a Regional Short-Term Forecasting Model to Predict the Total Electron Content Over Brazil"

Carolina Miozzi (University of Rome "Tor Vergata") "Self-Tuning Thin-Wire RFID Epidermal Antennas for Worldwide UHF Band Coverage"

Simone Nappi (University of Rome "Tor Vergata"), "RF Detection of Micro-Cracks in Orthopedic Implants by Conformal Space Filling Curves"

The URSI award and the honorary mentions were announced at the Italian URSI National Meeting 2019 and IEEE RFID-TA 2019 gala dinner. The dinner was organized at the Grand Hotel "Principe di Piemonte," in the city of Viareggio, 30 km from Pisa.

The URSI Italian National Committee believed that the Young Scientist Best Paper Award was successful, and they are very thankful to the members of the judging committee for their hard work during the selection process.

We also would like to express our appreciation to the three finalists who contributed to this special issue of the *Radio Science Bulletin* with their extended papers.

Roberto Sorrentino
President of the Italian National Committee of URSI
Deceased

Carlo Carobbi
Secretary of URSI Italian Committee
E-mail: carlo.carobbi@unifi.it

Giuliano Manara
URSI representative at IEEE RFID-TA 2019
and IEEE RFID-TA 2019 TPC Chair
E-mail: giuliano.manara@unipi.it

Andrea Michel
URSI Commission B ECR
and IEEE RFID-TA 2019 TPC Vice-Chair
E-mail: giuliano.manara@unipi.it

Paolo Nepa
IEEE RFID-TA General Chair
E-mail: paolo.nepa@unipi.it

Phase-Controlled Beamforming Network Intended for Conformal Arrays

Valentina Palazzi

Department of Engineering
University of Perugia
Perugia, Italy
E-mail: valentina.palazzi@unipg.it

Abstract

This work describes a reconfigurable 1 × 4 network able to provide beamforming capabilities to conformal antenna arrays. In particular, the proposed feed network is able to activate either single output ports or couples of adjacent output ports of a four-element array. The output-port selection is achieved by controlling only the phase of four variable phase shifters. In the case where two output ports are activated, the network is also able to control the phase relationship between the signals, enabling in-phase and 180°-out-of-phase signal configurations. To test the developed theory, a prototype in microstrip technology, designed to operate in the recently released sub-6 GHz 5G 3.4 GHz to 3.8 GHz band, was manufactured, confirming adequate behavior of the network. The proposed circuit was then connected to a four-element antenna cube where it was used to generate twelve different beams: eight equally-spaced beams over 360° with maximum gain in their broadside direction, which enabled a uniform coverage of the azimuthal plane, and four equally-spaced beams with nulls in their broadside direction, useful in applications such as interference removal and radio localization.

1. Introduction

As the number of wireless connected devices rapidly increases, the resources of current telecommunication systems are sufficient to meet all traffic needs [1-3]. A shortage of available frequency bands and interference issues may cause trouble for communications, thereby threatening connection reliability. To solve these issues and to improve the capacity of the network, upcoming communication standards are being designed to include countermeasures, such as new broader transmission bands and beamforming capabilities.

Since most of the upcoming 5G systems, including base stations, handheld devices, and hotspots, will be equipped with beam-steering and beamforming techniques, an impending need for reconfigurable transponders has emerged [4]. Such techniques allow front-ends to transmit a given signal only toward the desired recipients, reducing both interference and the transmitted power needed for a given transmission range [5]. Broadband microwave components are also being developed to take advantage of the new released bands and to guarantee higher transmission speeds.

Well-known beamforming-circuit configurations, such as the Butler matrix, are attracting renewed attention [6, 7]. However, most of the available studies were intended for linear arrays with an angular coverage lower than 180°, while complex multilayer topologies are required to achieve spatial scanning [8, 9]. At the same time, research is also focusing on reconfigurable power dividers, which can be used, among other things, to perform beamforming for conformal arrays [10-12].

This work describes the design, the theoretical analysis, and the experimental validation of a feed network intended for antenna topologies with radiating elements placed on the lateral sides of polygons (square in the specific case). The network is able to guarantee homogeneous 360° beam-steering in the azimuthal plane, while keeping control of the shape of the generated radiation patterns. This feed network was firstly presented in [13]. Here, the circuit is theoretically analyzed and tested in a more comprehensive way. The circuit design is described in Section 2, while the performance and experimental results of the fabricated prototype are discussed in Section 3.

2. Circuit Design

Figure 1 shows a conformal array composed of four radiating elements placed on the lateral sides of a cube and oriented according to the cardinal directions, i.e., north (N), east (E), south (S), and west (W), where the distance among radiating elements is lower than one wavelength in their operating band. When the antennas are individually fed, their radiation patterns have a maximum in the respective broadside directions (see radiation patterns N, S, E, W in Figure 1a). Moreover, additional radiation patterns are obtained when couples of adjacent radiating elements are simultaneously fed, with the following characteristics:

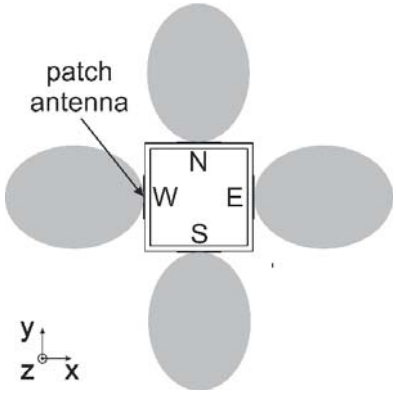

Figure 1a. A sketch of the proposed antenna system: radiation patterns (in gray) generated by single radiating elements. The four radiating elements are marked with their corresponding cardinal directions: N, E, S, and W.

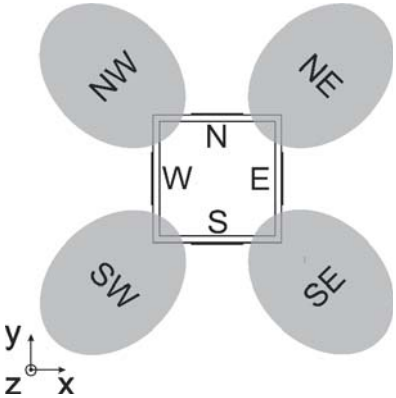

Figure 1b. A sketch of the proposed antenna system: radiation patterns generated by couples of radiating elements fed with in-phase equal-magnitude signals.

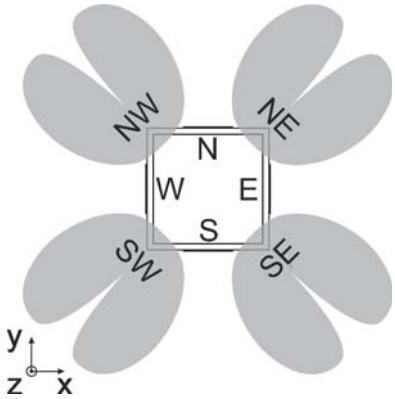

Figure 1c. A sketch of the proposed antenna system: radiation patterns generated by couples of radiating elements fed with 180° out-of-phase equal-magnitude signals.

- In the case where adjacent couples are excited with in-phase equal-magnitude signals, radiation patterns with maxima in the intermediate directions NE, SE, SW, and NW and antenna gains and beamwidths almost similar to the single radiating elements are obtained (see Figure 1b);

- In the case where adjacent antennas are fed with 180° out-of-phase signals, radiation patterns with nulls in the directions NE, SE, SW, and NW are obtained (see Figure 1c).

The first type of radiation patterns can be used to pursue a more homogeneous coverage of the azimuthal plane. Indeed, the H-plane 3-dB beamwidth of common radiating elements, such as patch antennas, is usually lower than 90°. This means that the gain of single antennas in the intermediate directions between adjacent radiating elements is lower than their maximum gain by more than 3 dB. Feeding both single antennas and couples of adjacent antennas with in-phase equal-magnitude signals, the number of steerable directions is doubled (from four to eight), thereby achieving a more homogeneous coverage without increasing the number of radiating elements of the array.

The second type of radiation patterns with a zero in the broadside direction (that can be obtained by feeding couples of adjacent radiating elements with equal-magnitude 180° out-of-phase signals) can profitably be used in many application scenarios, including interference removal in radio receivers (i.e., the zero can be oriented in the direction of the interference) and radio localization (i.e., the zero can be used to finely estimate the direction of arrival of a given radio signal). These additional features broaden the scope of the proposed array and improve its reliability.

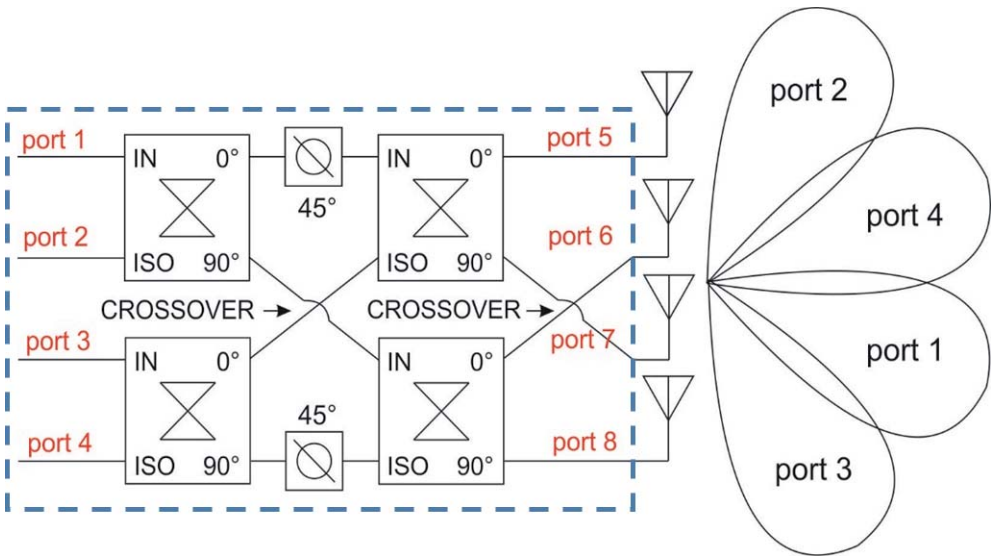

Figure 2. A schematic of a 4 × 4 Butler matrix.

Table 1. The 4 × 4 Butler matrix: relative phase difference among output ports as a function of activated input port.

Activated Input Port y	$\angle S_{x,y} - \angle S_{x+1,y}$ for $x = 5,...,8$
1	–45°
2	135°
3	–135°
4	45°

The goal of this paper is to develop a reconfigurable feed network for such a conformal array that is able to switch among the following states:

- Feed all single radiating elements;
- Feed all couples of adjacent radiating elements with equal-magnitude in-phase signals;
- Feed all couples of adjacent radiating elements with equal-magnitude 180° out-of-phase signals.

Traditional approaches, based on feed networks equipped with RF switches, are not applicable in this case, since each radiating element must be fed either individually or coupled to different adjacent elements without spoiling the matching conditions of the other elements, and this would lead to very tangled networks. We therefore decided to adopt an original approach, inspired by the Butler matrix topology [14]. The Butler matrix is an $N \times N$ circuit used to implement beam-steering (by way of example, Figure 2 shows the scheme of the 4 × 4 Butler matrix). Its working principle is as follows: one of the N input ports is selected and activated; the input power is equally divided by the network among the N output ports, and a constant phase difference is imposed among adjacent ports, where the latter difference varies with the selected input port (Table 1 reports the phase differences corresponding to the activated input ports for the 4 × 4 network).

Since the matrix is reciprocal, its output ports can be logically exchanged with the input ports. This means that if we feed all input ports using signals with equal magnitude and specific phase differences, the input power can be combined toward a single output port (the activated output port depends on the selected phase differences). In the present work, we investigated whether we could modify the Butler-matrix architecture and find phase relations among the input signals so that we could combine the input power not only toward single output ports, but also toward couples of adjacent output ports.

The scheme of the proposed feed network (patent pending) is shown in Figure 3. The input signal at port 1 is divided into four equal parts by a four-way power divider. Each signal is then phase shifted by a variable phase shifter (the phase variables are marked with the Greek letters α, β, γ and δ). Finally, the obtained signals enter the 4 × 4 matrix, so that the desired output ports are activated. The matrix is composed of four 90° hybrid couplers like the 4 × 4 Butler matrix, while the two 45° phase shifters are replaced by two 90° phase shifters.

Assuming all components and interconnections are ideal, the S-parameter matrix of the network can be easily calculated as follows:

$$[S] = \begin{bmatrix} 0 & S_{21} & S_{31} & S_{41} & S_{51} \\ S_{21} & 0 & 0 & 0 & 0 \\ S_{31} & 0 & 0 & 0 & 0 \\ S_{41} & 0 & 0 & 0 & 0 \\ S_{51} & 0 & 0 & 0 & 0 \end{bmatrix}$$

The transmission coefficients of the network S_{k1}, where $k = 2,...,5$, are composed of four terms that combine to determine the selected output signals of the network based on the values of the phase variables α, β, γ, and δ, as follows:

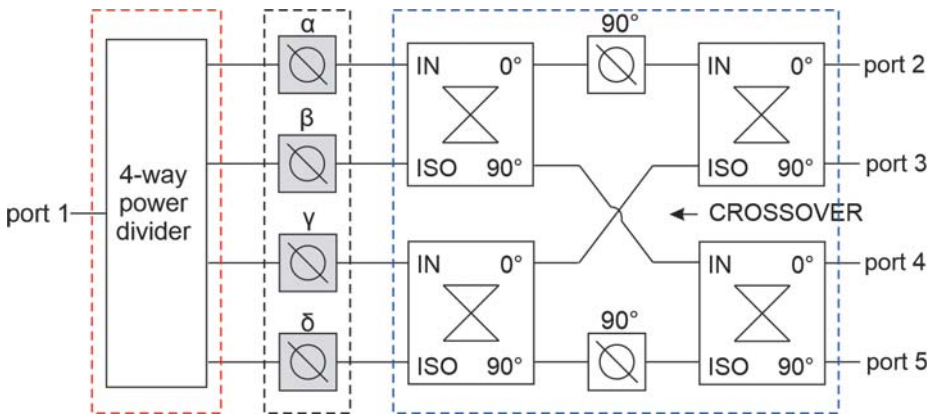

Figure 3. A schematic of the proposed 1 × 4 reconfigurable feed network.

$$S_{21} = \frac{1}{4}\left(-je^{-j\alpha} - e^{-j\beta} - je^{-j\gamma} - e^{-j\delta}\right), \quad (1)$$

$$S_{31} = \frac{1}{4}\left(-e^{-j\alpha} + je^{-j\beta} + e^{-j\gamma} - je^{-j\delta}\right), \quad (2)$$

$$S_{41} = \frac{1}{4}\left(-je^{-j\alpha} + e^{-j\beta} + je^{-j\gamma} - e^{-j\delta}\right), \quad (3)$$

$$S_{51} = \frac{1}{4}\left(-e^{-j\alpha} - je^{-j\beta} - e^{-j\gamma} - je^{-j\delta}\right). \quad (4)$$

From Equations (1)-(4), the squared magnitudes of the transmission coefficients can be expressed as follows:

$$|S_{21}|^2 = \frac{1}{4} + \frac{1}{8}(a+b), \quad (5)$$

$$|S_{31}|^2 = \frac{1}{4} + \frac{1}{8}(a-b), \quad (6)$$

$$|S_{41}|^2 = \frac{1}{4} + \frac{1}{8}(-a+c), \quad (7)$$

$$|S_{51}|^2 = \frac{1}{4} + \frac{1}{8}(-a-c), \quad (8)$$

where auxiliary variables are introduced to simplify the analysis:

$$a = \sin(x) + \sin(y), \quad (9)$$

$$b = \cos(z) + \sin(z+y) - \sin(z-x) + \cos(z+y-x) \quad (10$$

$$c = -\cos(z) + \sin(z+y) - \sin(z-x) - \cos(z+y-x) \quad (11)$$

$$x = \alpha - \beta, \quad (12)$$

$$y = \gamma - \delta, \quad (13)$$

$$z = \alpha - \gamma. \quad (14)$$

The phases of the transmission coefficients can be expressed as functions of x, y, and z as follows:

$$\angle S_{21} = \tan^{-1}\left[\frac{-\cos(\alpha) + \sin(\alpha - x) - \cos(\alpha - z) + \sin(\alpha - z - y)}{-\sin(\alpha) - \cos(\alpha - x) - \sin(\alpha - z) - \cos(\alpha - z - y)}\right] \quad (15)$$

$$\angle S_{31} = \tan^{-1}\left[\frac{\sin(\alpha) + \cos(\alpha - x) - \sin(\alpha - z) - \cos(\alpha - z - y)}{-\cos(\alpha) + \sin(\alpha - x) + \cos(\alpha - z) - \sin(\alpha - z - y)}\right] \quad (16)$$

Table 2. The relationships among output signal configurations and auxiliary variables.

$\|S_{21}\|^2$	$\|S_{31}\|^2$	$\|S_{41}\|^2$	$\|S_{51}\|^2$	a	b	c	x	y	z	**Phase Diff.**
1	0	0	0	2	4	0	90°	90°	0°	/
0	1	0	0	2	–4	0	90°	90°	180°	/
0	0	1	0	–2	0	4	270°	270°	180°	/
0	0	0	1	–2	0	–4	270°	270°	0°	/
½	½	0	0	2	0	0	90°	90°	270° 90°	0° 180°
0	0	½	½	–2	0	0	270°	270°	90° 270°	0° 180°
½	0	0	½	0	2	–2	180° 0°	180° 0°	0°	0° 180°
0	½	½	0	0	–2	2	0° 180°	0° 180°	180°	0° 180°

$\angle S_{41} =$

$$\tan^{-1}\left[\frac{-\cos(\alpha)-\sin(\alpha-x)+\cos(\alpha-z)+\sin(\alpha-z-y)}{-\sin(\alpha)+\cos(\alpha-x)+\sin(\alpha-z)-\cos(\alpha-z-y)}\right] \quad (17)$$

$\angle S_{51} =$

$$\tan^{-1}\left[\frac{\sin(\alpha)-\cos(\alpha-x)+\sin(\alpha-z)-\cos(\alpha-z-y)}{-\cos(\alpha)-\sin(\alpha-x)-\cos(\alpha-z)-\sin(\alpha-z-y)}\right] \quad (18)$$

We therefore first determine the auxiliary variables *a*, *b*, and *c*, corresponding to the magnitude configurations of interest, according to Equation (5)-(8). We then find the corresponding values of *x*, *y*, and *z*. We finally obtain the phase relationships between the activated signals according to Equations (15)-(18).

The results are shown in Table 2. In cases corresponding to one-port activations (i.e., the first four cases in Table 2), a unique solution for *x*, *y*, and *z* is obtained for each triplet *a*, *b*, and *c*. On the other hand, in cases corresponding to two-port activations, two *x*, *y*, and *z* solutions are found for each triplet *a*, *b*, and *c*: one corresponding to in-phase output signals and the other to 180° out-of-phase signals. It is worth mentioning that since the network is intended to be utilized in circular arrays, port 2 is considered to be adjacent to port 5.

The last step is to determine the phase variables α, β, γ, and δ, corresponding to the auxiliary variables *x*, *y*, and *z*. To do so, we need to solve the system of Equations (12)-(14) comprised of three linear equations with four unknowns. Such a system has infinite solutions: this means that the value of one of the four phase shifters can be arbitrarily set, and that multiple phase combinations can lead to the same output signal configuration.

One representative phase solution is reported in Table 3 for each output signal configuration. All phase variables were multiples of 90°. Therefore, they could be implemented using two-bit phase shifters. A progressive number, *N*, was associated with each phase configuration for future reference.

The final system presented one RF input port, four RF output ports, and the relevant control pins for the variable phase shifters. The proposed feed network not only made it possible to activate couples of adjacent output ports with in-phase signals (see rows for $N = 5,...,8$ in Table 3), but also with 180° out-of-phase signals (see rows for $N = 9,...,12$ in Table 3). It therefore provided the system with additional beamforming capabilities that will further improve the system's ability to be reconfigured and its field of applications.

3. Experimental Results

A prototype of the proposed feed network in microstrip technology was designed, manufactured, and tested (see Figure 4). The main parts of the circuit were surrounded by three rectangles, corresponding to those shown in Figure 3:

- A fixed four-way power divider (red rectangle), composed of three cascaded two-way Wilkinson dividers;
- A bank of four variable phase shifters (black rectangle): each block consisted of a two-bit switched-line phase shifter. Commercial voltage-controlled single-pole double-through switches (AS179-92LF model from Skyworks [15]) were used to select the desired path. Each switch introduced an insertion loss of 0.5 dB, thereby leading to an overall phase-shifter insertion loss of about 2 dB. The control pins of the switches were connected to the power supply through wires.

Table 3. The relationships among phase variables and activated output ports.

N	α	β	γ	δ	Output Ports	Phase Diff.
1	90°	0°	90°	0°	2	/
2	90°	0°	270°	180°	3	/
3	180°	270°	0°	90°	4	/
4	0°	90°	0°	90°	5	/
5	90°	0°	180°	90°	2-3	0°
6	0°	180°	180°	0°	3-4	0°
7	90°	180°	0°	90°	4-5	0°
8	0°	0°	0°	0°	2-5	0°
9	180°	90°	90°	0°	2-3	180°
10	0°	0°	180°	180°	3-4	180°
11	0°	90°	90°	180°	4-5	180°
12	0°	180°	0°	180°	2-5	180°

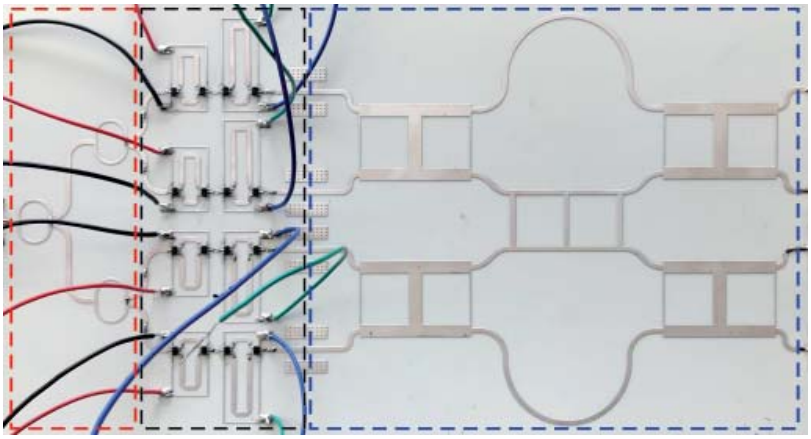

Figure 4. The prototype of the complete feed network: (l-r) four-way power divider (red rectangle), two-bit phase shifters (black rectangle) and 4 × 4 matrix (blue rectangle). The visible wires are for switching control. The active area was 20 cm² × 10 cm² (after [13]).

- A Butler-like 4 × 4 matrix (blue rectangle): the four 90° hybrid couplers and the crossover of the matrix were implemented with "double-box" 3 dB and 0 dB branch-line couplers, respectively. The "double-box" configuration was chosen to improve the operating bandwidth of the system. The two 90° fixed phase shifters were implemented with quarter-wave line sections.

The prototype was designed to operate in the sub-6 GHz 5G band (3.4 GHz to 3.8 GHz: i.e., 11% bandwidth around 3.6 GHz), and the substrate adopted was 0.5-mm-thick Roger 4350B substrate ($\varepsilon_r = 3.66$, $\tan\delta = 0.004$).

The three parts of the circuit were first separately studied. The four-way power divider and the bank of phase shifters were designed by performing schematic simulations within *Advanced Design Suite* (*ADS*), while full-wave simulations were used for the Butler-like 4 x 4 matrix (the FEM simulator of *CST Studio Suite* was used). Finally, the *S* parameters of the latter part were imported within *ADS* and the whole circuit was simulated (co-simulation approach).

The *S* parameters of the manufactured feed-network prototype were measured with a vector network analyzer (VNA, FieldFox N9981A model). The transmission coefficients obtained for the output signal configurations of interest are shown in Figure 5-7 and compared to simulation results. A good agreement was observed in all cases.

Figure 5 shows the magnitude of the transmission coefficients in the single-port activation configurations, i.e., for $N = 1,..,4$. The magnitude of the transmission coefficients of the activated ports was around -3.7 dB in all four cases, accounting for both the insertion loss of the switches (around 2 dB) and the line loss (which resulted in about 1.7 dB). It was significantly flat in all the band of interest, with a very small maximum variation of 0.5 dB. The transmission coefficients of the deactivated ports were below -19 dB.

On the other hand, the magnitude of the transmission coefficients of the activated ports in the two-port activation configurations with in-phase signals was around 3 dB below the single-port configurations. This was due to the fact that the input power was split between two ports, as shown in Figures 6a and 6c. A still satisfactory maximum

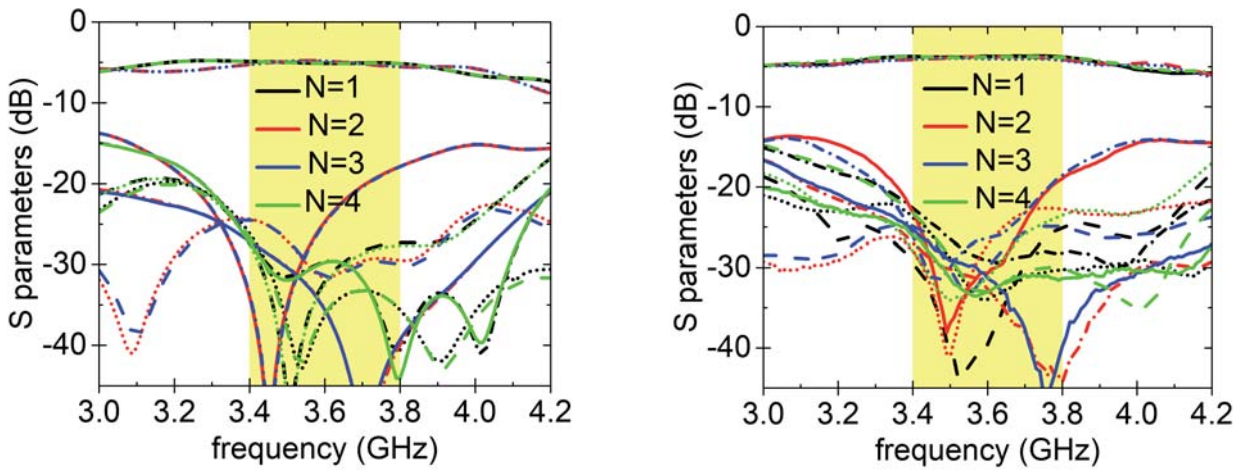

Figure 5. The simulated (a) and measured (b) magnitudes of the transmission coefficients of the complete 1 × 4 network as functions of frequency for single-port activation. The solid line refers to $|S_{21}|$, the dashed line to $|S_{31}|$ the dotted line to $|S_{41}|$, and the dashed dotted line to $|S_{51}|$ (after [13]).

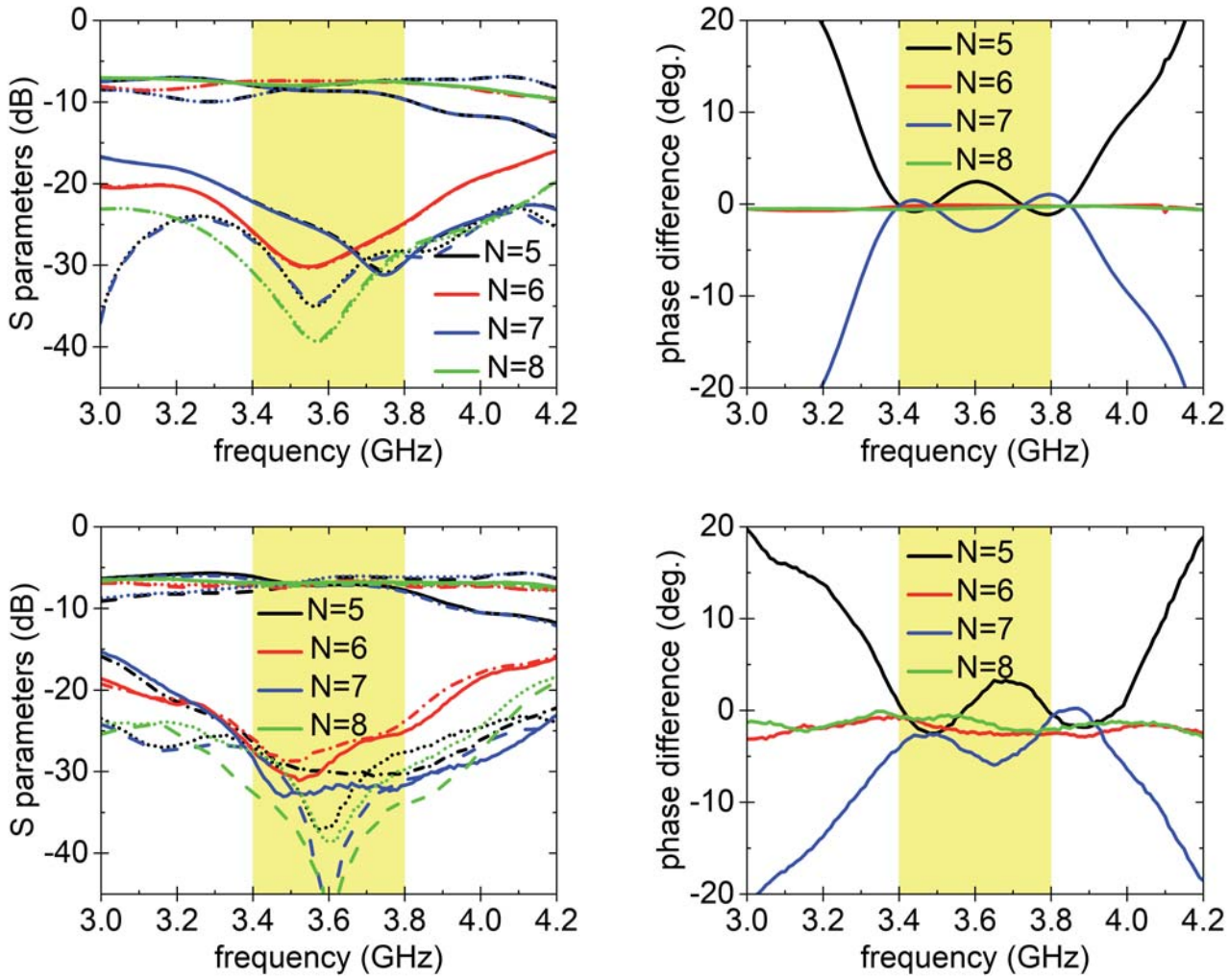

Figure 6. The magnitudes (a)-(c) and phase differences (b)-(d) of the transmission coefficients of the complete 1 × 4 network as functions of frequency for the cases $N = 5,...,8$. Plots (a)-(b) report simulation results and (c)-(d) show measurements. The solid line refers to $|S_{21}|$, the dashed line to $|S_{31}|$, the dotted line to $|S_{41}|$, and the dashed dotted line to $|S_{51}|$ (after [13]).

variation of less than 2 dB (i.e., transmission coefficient between -6.1 dB and -8 dB) was experienced in the band of interest. The transmission coefficients of the deactivated ports were below -24 dB.

Figures 6b and 6d illustrate the phase difference between the transmission coefficient of adjacent ports for cases $N = 5,...,8$. The measured phase differences between the two activated ports, ideally in phase, were below 6° in all cases in the whole band.

Finally, the magnitudes and phase differences of the transmission coefficients for $N = 9,...,12$ are shown in Figure 7. The magnitudes of the activated ports were on the same level as the in-phase cases shown in Figure 6, with a maximum variation lower than 2.2 dB in all the band. The transmission coefficients of the deactivated ports were below -21 dB. Concerning phase relationships, the signals corresponding to each couple of activated output ports were 180° out of phase, with a phase error lower that 8° in the band of interest.

Finally, an experiment was performed in a laboratory room to assess the beamforming capabilities of the designed network, as shown in Figure 8. Four square patch antennas, arranged on the sides of a cube, were designed and manufactured by using a 1.6 mm-thick low-cost FR4 substrate ($\varepsilon_r = 4.7$, $\tan\delta = 0.011$), to implement the antenna topology illustrated in Figure 1. The four patch antennas, placed on a rotating platform, were connected to the output ports of the proposed feed network by means of four identical flexible coaxial cables, while the input port of the feed network was connected to a vector network analyzer. The second port of the vector network analyzer was connected to a single patch antenna (right side of Figure 8). Both the single patch and the antenna cube were aligned and placed at a distance of 50 cm, so that they operated in their far-field regions.

The H-plane radiation patterns of the cube corresponding to the signal configurations of interest were finally evaluated (see Figures 9-11). The measurements were performed in an open-air environment without special

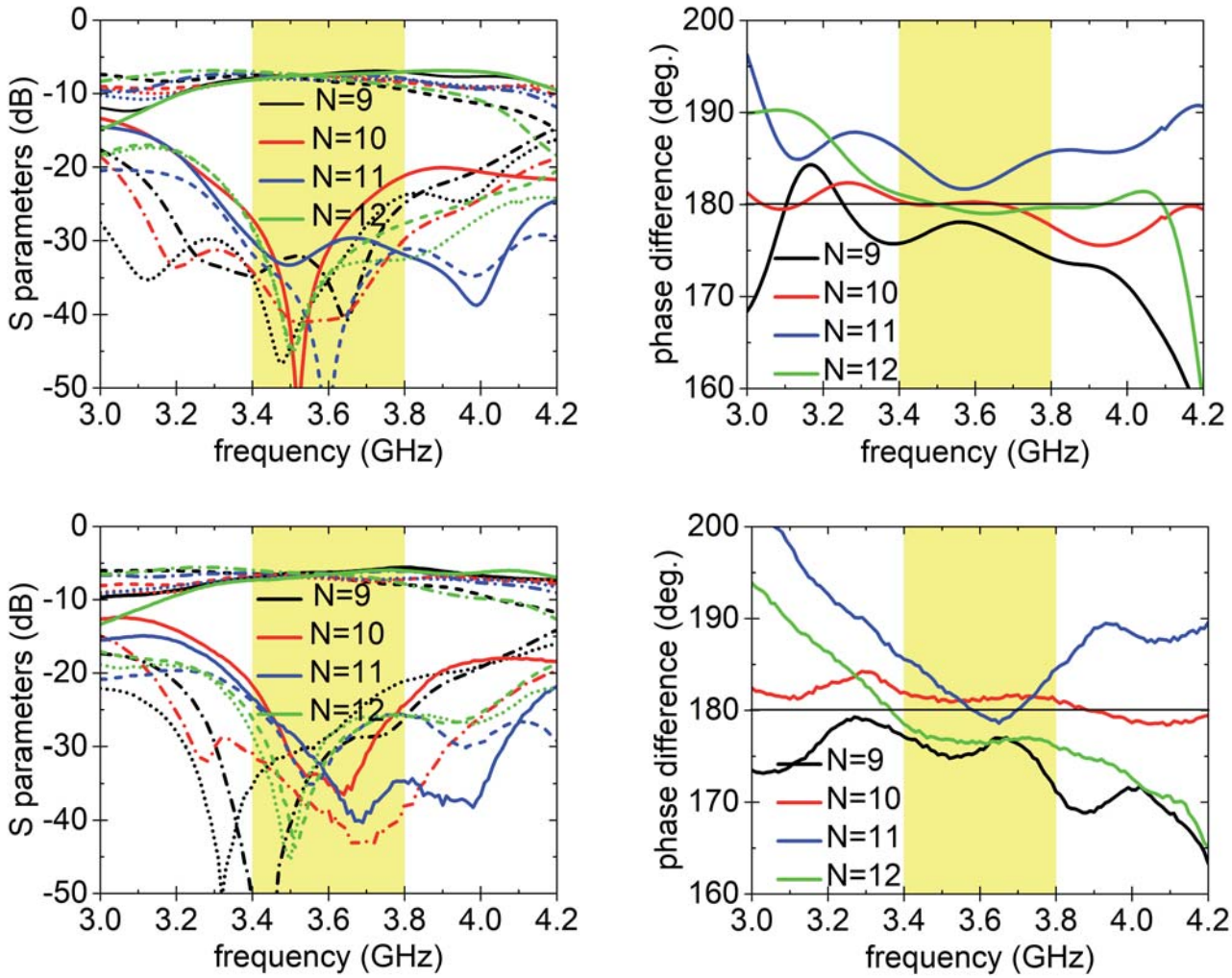

Figure 7. The magnitudes (a)-(c) and phase differences (b)-(d) of the transmission coefficients of the complete 1 × 4 network as functions of frequency for the cases $N = 9,...,12$. Plots (a)-(b) report simulation results and (c)-(d) show measurements. The solid line refers to $|S_{21}|$, the dashed line to $|S_{31}|$, the dotted line to $|S_{41}|$, and the dashed dotted line to $|S_{51}|$.

anechoic provisions, and were compared to the simulation results. Despite the impact of the measurement setup, there was a good agreement with the simulations, thus confirming the adequate behavior of the system. The absolute level of the received power along the directions of the maxima was fairly independent of the selected configuration (maximum measured difference below 1.1 dB among all cases).

In Figure 12, a comparison between the radiation patterns obtained with the signal configurations $N = 6$

Figure 8. A photo of the complete system, including the antenna topology and the beamforming network. The side of the cube was 45 mm, while the side of the square patch was 19.3 mm.

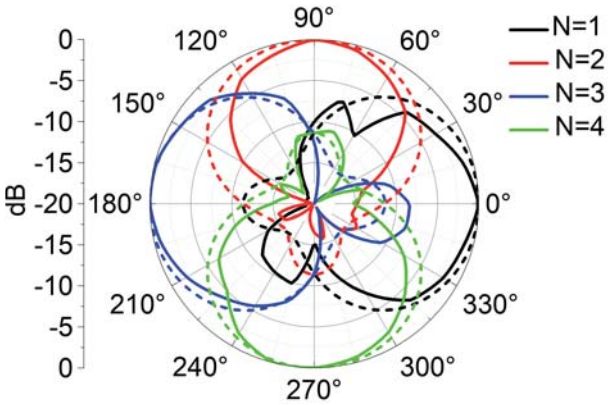

Figure 9. A comparison between simulated (dashed) and measured (solid) H_θ -plane (xy-plane) radiation patterns as a function of phase configurations. The input phases were configured for single-port activation (after [13]).

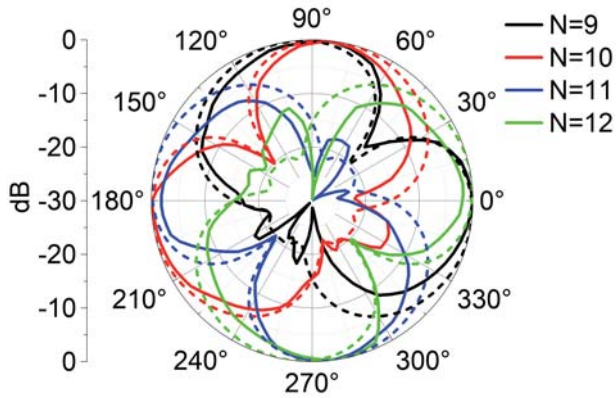

Figure 11. A comparison between simulated (dashed) and measured (solid) H_θ -plane (xy-plane) radiation patterns as a function of phase configurations. The input phases were configured for 180° out-of-phase two-port activation (after [13]).

and $N = 10$ are shown, corresponding to the cases where the same two output ports were activated (i.e., ports 3 and 4), either in-phase or 180° out of phase. For $N = 10$ a null was obtained, corresponding to the direction of maximum radiation for $N = 6$: the gain of the antenna in the broadside direction for $N = 10$ was more than 20 dB lower than the gain obtained for $N = 6$. This suggested that the feed network provided the antenna with additional beamforming capabilities that could be useful in many applications, such as, for instance, radio localization.

4. Conclusion

A phase-controlled 1 × 4 beamforming network for conformal arrays, able to feed either single antennas or a couple of adjacent radiating elements simultaneously, was described and theoretically analyzed. A single-layer feed-network prototype was fabricated, operating in the frequency range 3.4 GHz to 3.8 GHz, and featuring satisfactory performance throughout the band of interest. The feed network was connected to a four-element antenna

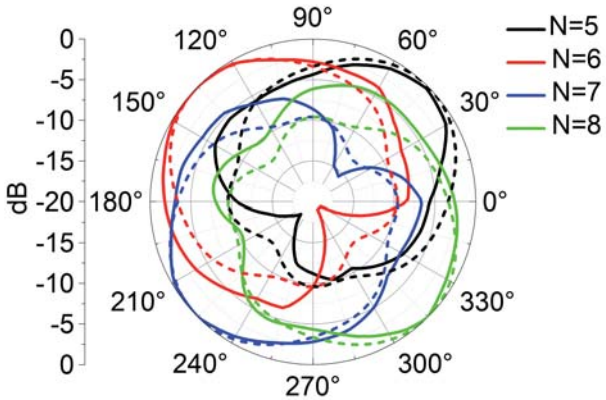

Figure 10. A comparison between simulated (dashed) and measured (solid) H_θ -plane (xy-plane) radiation patterns as a function of phase configurations. The input phases were configured for in-phase two-port activation (after [13]).

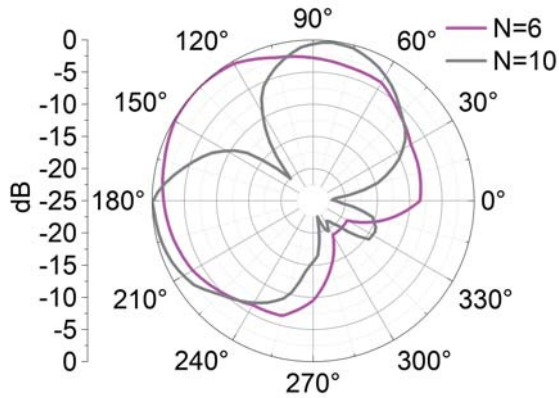

Figure 12. The measured radiation patterns for $N = 6$ and $N = 10$.

topology, demonstrating its capability to steer beams with a 45° step in the azimuthal plane. Additional beamforming configurations, characterized by the presence of notches, were also demonstrated. These are important for applications such as interference suppression and radio localization, thereby showing the versatility of the proposed feed network. This circuit opens the door to a new class of reconfigurable feed networks for conformal arrays, particularly relevant for next-generation reconfigurable front-ends.

5. References

1. G. A. Akpakwu, Bruno J. Silva, G. P. Hancke, and A. M. Abu-Mahfouz, "A Survey on 5G Networks for the Internet of Things: Communication Technologies and Challenges," *IEEE Access*, **6**, 2018, pp. 3619-3647.

2. TE connectivity, "White Paper: Mass Connectivity in the 5G Era," https://www.te.com/usa-en/trends/iot-5g-ai/insights/mass-connectivity-5g-era.html, accessed October 2020.

3. J. G. Andrews, S. Buzzi, W. Choi, S. V. Hanly, A. Lozano, A. C. K. Soong, and J. C. Zhang, "What Will 5G Be?," *IEEE Journal on Selected Areas in Communications*, **32**, 6, June 2014, pp. 1065-1082.

4. W. Roh, J.-Y. Seol, J. Park, B. Lee, J. Lee, Y. Kim, J. Cho, K. Cheun, and F. Aryanfar, "Millimeter-Wave Beamforming as an Enabling Technology for 5G Cellular Communications: Theoretical Feasibility and Prototype Results," *IEEE Communications Magazine*, **52**, 2, February 2014, pp. 106-113.

5. S. Sun, T. S. Rappaport, R. W. Heath, A. Nix, and S. Rangan," MIMO for Millimeter Wave Wireless Communications: Beamforming, Spatial Multiplexing, or Both?," *IEEE Communications Magazine*, **52**, 12, December 2014, pp. 110-121.

6. H. Ren, B. Arigong, M. Zhou, J. Ding, and H. Zhang," A Novel Design of 4 × 4 Butler Matrix with Relatively Flexible Phase Differences," *IEEE Antennas and Wireless Propagation Letters*, **15**, 2016, pp. 1277-1280.

7. L. Zhong, Y. Ban, J. Lian, Q. Yang, J. Guo and Z. Yu, "Miniaturized SIW Multibeam Antenna Array Fed by Dual-Layer 8 × 8 Butler Matrix," *IEEE Antennas and Wireless Propagation Letters*, **16**, 2017, pp. 3018-3021.

8. J. Lian, Y. Ban, Q. Yang, B. Fu, Z. Yu and L. Sun, "Planar Millimeter-Wave 2-D Beam-Scanning Multibeam Array Antenna Fed by Compact SIW Beam-Forming Network," *IEEE Transactions on Antennas and Propagation*, **AP-66**, 3, March 2018, pp. 1299-1310.

9. C.-H. Hsieh, Y.-T. Lin, H.-C. Jhan, and Z.-M. Tsai," Application of a Two-Dimensional Butler Matrix Antenna Array For Tile-Based Beamforming," *IEICE Electronics Express*, **16**, 11, 2019, pp. 1-6.

10. A. Ocera, P. Farinelli, F. Cherubini, P. Mezzanotte, R. Sorrentino, B. Margesin, and F. Giacomozzi," A MEMS-Reconfigurable Power Divider on High Resistivity Silicon Substrate," 2007 IEEE/MTT-S International Microwave Symposium, Honolulu, HI, 2007, pp. 501-504.

11. H. Tae, K. Oh, H. Lee, W. Son and J. Yu, "Reconfigurable 1 × 4 Power Divider with Switched Impedance Matching Circuits," *IEEE Microwave and Wireless Components Letters*, **22**, 2, February 2012, pp. 64-66.

12. H. Fan, X. Liang, J. Geng, L. Liu, and R. Jin, "An N-Way Reconfigurable Power Divider," *IEEE Transactions on Microwave Theory and Techniques*, **65**, 11, November2017, pp. 4122-4137.

13. V. Palazzi, P. Mezzanotte, and L. Roselli, "A Novel Agile Phase-Controlled Beamforming Network Intended for 360° Angular Scanning in MIMO Applications," 2018 IEEE/MTT-S International Microwave Symposium-IMS, Philadelphia, PA, 2018, pp. 624-627.

14. J. Butler, "Beam-Forming Matrix Simplifies Design of Electronically Scanned Antennas," *Electronic Design*, **9**, 8, April 1961, pp. 170-173.

15. Skyworks®, "AS179-92LF: 20 MHz to 4.0 GHz GaAs SPDT Switch," https://www.skyworksinc.com/-media/D73E805A9AC8424980010E10BE76C5DF.pdf.

RF Design and Experimental Test of a Quadrupole-Free X-Band TM_{01} Mode Launcher

G. Torrisi[1], G. S. Mauro[1,2], G. Sorbello[3,1], G. Castorina[4], L. Celona[1], L. Faillace[4], B. Spataro[4], and V. Dolgashev[5]

[1]Istituto Nazionale di Fisica Nucleare
Laboratori Nazionali del Sud (INFN-LNS)
Via S. Sofia 62, 95123 Catania, Italy
E-mail:giuseppe.torrisi@lns.infn.it

[2]Dipartimento di Ingegneria dell'Informazione,
delle Infrastrutture e dell'Energia Sostenibile
Università degli Studi Mediterranea di Reggio Calabria
Salita Melissari
89124 Reggio Calabria RC

[3]Dipartimento di Ingegneria Elettrica, Elettronica e Informatica
Università degli Studi di Catania
Viale Andrea Doria 6, 95125, Catania, Italy

[4]Istituto Nazionale di Fisica Nucleare
Laboratori Nazionali di Frascati (INFN-LNF)
Via Enrico Fermi, 40, 00044 Frascati RM Italy

[5]SLAC National Accelerator Laboratory
Menlo Park, USA

Abstract

In this work, we present a low-power RF characterization of a novel TM_{01} X-band mode launcher for the new generation of high-brightness RF photo-injectors. The proposed structure employs a fourfold symmetry in order to minimize both the dipole and the quadrupole fields that could cause an emittance growth in the early stages of the acceleration process. A "cold" model aluminum structure, comprising two mode launchers connected by a central 62 mm-long circular waveguide, was fabricated by milling aluminum blocks, assembled and measured in back-to-back configuration. The low-power RF test, performed at the Istituto Nazionale di Fisica Nucleare Laboratori Nazionali del Sud (INFN-LNS), validated both the numerical simulations and the quality of the fabrication. An oxygen-free high-conductivity copper version of the device is being manufactured for high-power and ultra-high-vacuum tests that are planned to be conducted at the Stanford Linear Accelerator Center (SLAC).

1. Introduction and Motivation

High-gradient radio-frequency (RF) devices will be crucial for innovative accelerating structures to increase brilliance of accelerated bunches. Accelerating gradients up to 250 MV/m can be achieved using cryogenically cooled copper accelerating structures [2, 1]. High brilliance and high field quality are required in the RF photo guns and in its power coupler.

This work presents a novel power coupler, working at X band, which is able to convert the input rectangular TE_{10} mode into a circular TM_{01} mode that can be used for particle acceleration. The device employs a fourfold symmetry in order to minimize the undesired RF components that can arise in the mode-launching section, causing an undesired emittance growth during the first stages of the accelerating process [7]. In particular, the work was focused on the low-power RF tests performed on an aluminum prototype, consisting of two identical mode

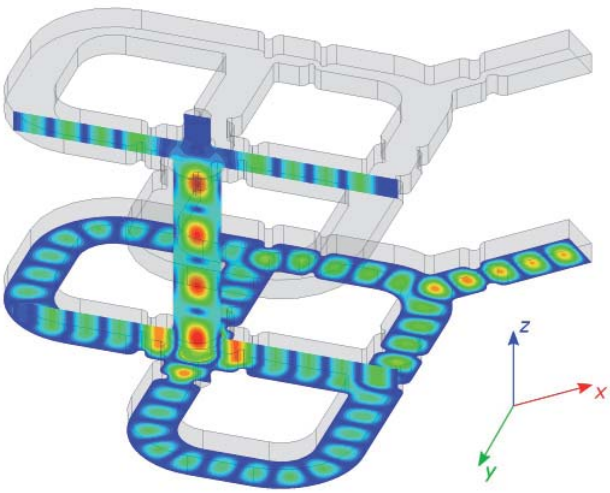

Figure 1. A three-dimensional model of the back-to-back structure. The simulated electric field of the two mode launcher arms as well as the central circular waveguide section are visible.

launchers joined through a central circular waveguide. This back-to-back configuration allowed us to characterize the structure in terms of *S* parameters, and also permitted measuring the electric field along the circular waveguide axis and along the azimuthal coordinate at a fixed radius through the bead-pull technique.

2. Mode Launcher RF Design

The presented mode launcher, working at X band, uses four symmetric sidewall coupling apertures of proper dimensions that, being fed with equal amplitude in-phase signals, excite the TM_{01} mode. The geometry of the branching network reduces the overall structure dimensions and allows the on-axis power coupling of the azimuthally symmetric accelerating mode. Thanks to the previously mentioned fourfold symmetry, the structure is able to minimize the undesired quadrupole modes [6]. Figure 1 shows the three-dimensional model of the structure in back-to-back configuration: the two mode-launcher sections with fourfold symmetry and the central circular waveguide with the TM_{01} mode are visible.

2.1 Mode-Launcher Feeding Layout Design

Details on the TM_{01} mode-launcher feeding layout, the delay line to match the phase at the sidewall coupling apertures, and matching bumps can be found in [7]. The H-plane branching network was optimized with a quasi-two-dimensional model [5] that took advantage of the field-translational symmetry to use a reduced computational domain. The TE_{10} rectangular waveguide branching line, shown in Figure 1, was studied taking advantage of the y invariance of the TE_{10}-mode fields. This allowed very fast two-dimensional simulation compared to a full-wave three-dimensional model. However, two-dimensional models (except for the case of ideal PEC waveguides) fail to correctly evaluate the waveguide losses. It is possible to restore the correct attenuation by introducing a fictitious conductivity, σ', for the top/bottom a-wide side of the waveguide:

$$\sigma' = CF\sigma = \left(\frac{b}{b'}\right)^2 \sigma , \tag{1}$$

where the correction factor $CF = (b/b')^2$, is given by the ratio between the initial three-dimensional height, b, and the reduced height, b', of the quasi-two-dimensional model. Thanks to the correction factor on the top/bottom waveguide walls of the reduced b' height model, the correct attenuation loss can be accurately predicted.

The correction introduced above is valid for H-plane devices supporting TE_{p0} modes. However, to the extent the waveguide height, b, is kept low, higher TE_{pq} with $q \neq 0$ are not supported by the structure. Standard waveguide devices usually fulfill this requirement.

By taking advantage of the fast simulations, the branching network of Figure 1 was optimized. After the optimization, full-height three-dimensional simulations were carried out to model the side coupling in the four rectangular-to-circular side-aperture transitions.

2.2 Computation of Multipole Component Coefficients

The accelerating voltage inside the circular waveguide can be expressed as [7]

$$V_{\pm} = \int_{z_0}^{z_f} E_z(r,\theta,z) e^{\pm ik_0 z} dz , \tag{2}$$

Table 1. The discrete Fourier coefficients for the presented fourfold device compared to the simulated single and dual port devices

	Single Port	Dual Port	Quad Port
M_0	23.25	21.30	21.05
M_1	0.266	1.923×10^{-4}	2×10^{-3}
M_2	0.0714	0.0925	2.697×10^{-4}

where r, θ, and z are respectively the radial, azimuthal, and axial coordinates of the circular waveguide section. k_0 is the wavenumber of the RF input power, and z_0, z_f are the starting and the ending points of the linear path through which the axial voltage is being integrated.

The multipole components of the structure were calculated through the discrete Fourier transform of the accelerating voltage, given by [4]

$$M_{\pm,s}(r) = \frac{1}{\sqrt{n}} \sum_{j=1}^{n} V_{\pm}\left(r,\theta_j\right) e^{2\pi i(j-1)s/n}, \qquad (3)$$

where n is the number of the calculated azimuthal variations, $M_{\pm,s}$ is the calculated mode with index s (M_0 for monopolar, M_1 for dipolar, M_2 for quadrupolar component).

In order to verify the minimization of the quadrupole components obtained with the presented structure, two other mode-launching structures operating at 11.424 GHz were simulated, in back-to-back configuration, in Ansys *HFSS*. These are not reported here for the sake of brevity. One was a device that converts the TE_{10} into the TM_{01} by using a single rectangular waveguide. The other was a device that converts the TE_{10} into the TM_{01} by using two rectangular waveguides. Table 1 reports the discrete Fourier coefficients, calculated through Equation (3), for the three devices discussed and with the following parameters: $r = 4$ mm, $\theta \in [0;360]$ degrees, $z_f - z_0 = 88$ mm (i.e., the total length of the circular waveguide section comprising the thickness of the aluminum walls).

From Table 1, it can be seen that the structure presented minimized the quadrupolar component of about two orders of magnitude with respect to the simulated single and dual-port structures.

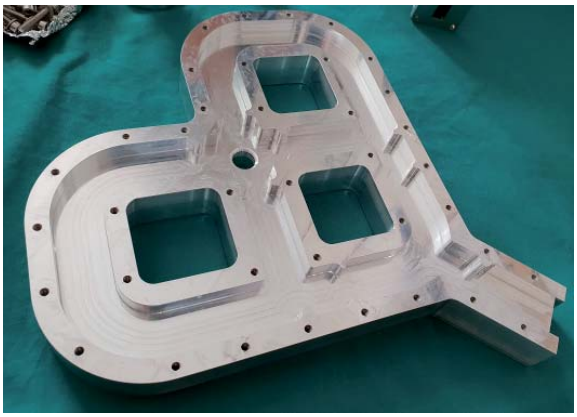

Figure 2a. A photo of the manufactured aluminum mode launcher for low-power-RF tests: the slotted plane of the mode launcher.

3. Fabrication and Low-Power-Microwave Tests

Figures 2a and 2b respectively show an internal view of the mode-launcher structure and the final assembled identical mode launchers. The figures also show the central junction on which the circular waveguide section was connected.

The mode-launcher structure was composed of two aluminum halves: a milled plate where the waveguide branching was machined (see Figure 2a) and a plane cover that closed the assembly. The milling of aluminum blocks was done using a tolerance of 10 μm and a surface roughness of 100 nm. Because the "low-power-microwave test" aluminum structure was based on two pieces, it required a large number of screws, properly positioned in order to ensure good RF contact between the two parts.

Two identical aluminum prototypes (Figure 2b) were fabricated in order to perform the experimental RF characterization. These two prototypes were joined together through a 62 mm-long circular waveguide.

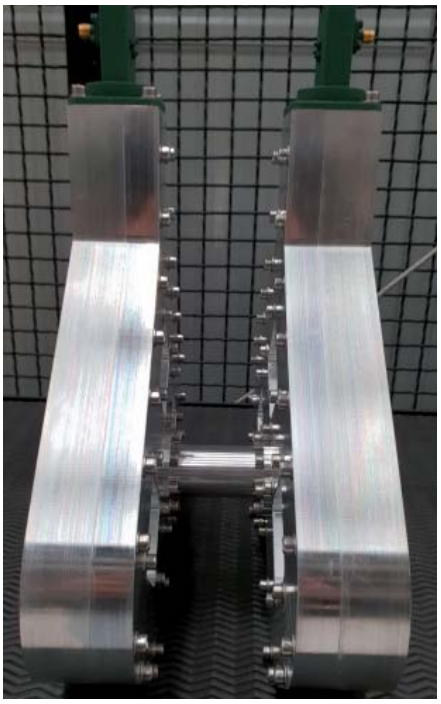

Figure 2b. Photos of two identical fabricated mode launchers for the back-to-back measurement.

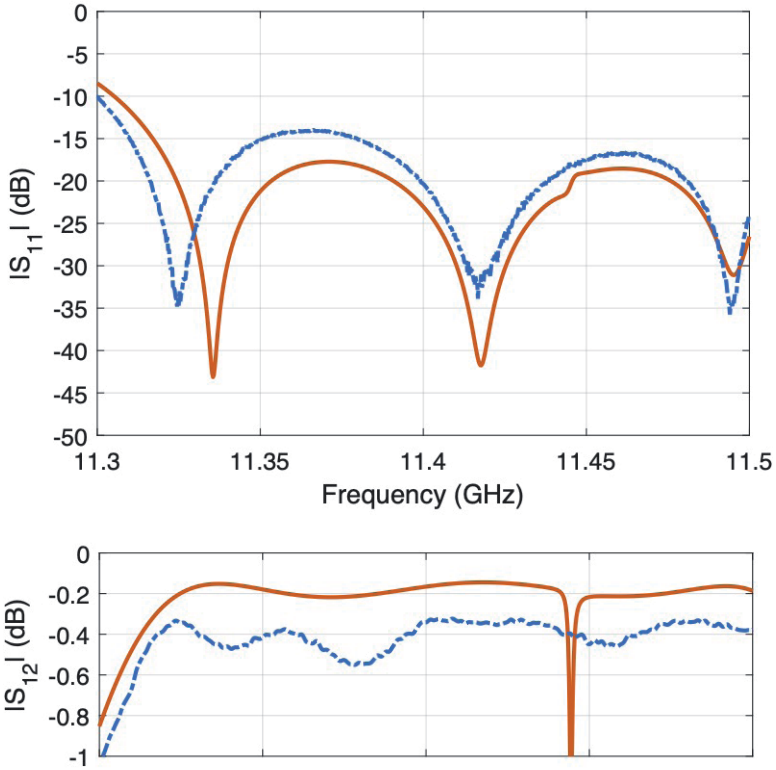

Figure 3. A comparison of the measured (blue dash-dotted curve) and simulated (orange curve) reflection and transmission coefficients, $|S_{11}|$ and $|S_{12}|$, for the full device in back-to-back configuration. At the working frequency of 11.42 GHz, the measured $|S_{11}|$ was about -30 dB while the $|S_{12}|$ was about -0.3 dB.

3.1 Measurement of *S* Parameters

A vector network analyzer was connected to the input and output rectangular waveguide sections of the full structure. Figure 3 shows the comparison between the simulated and experimental scattering parameters $|S_{11}|$ and $|S_{12}|$, respectively) of the assembled prototype.

The device was well matched into the interval of 11.3 GHz to 11.5 GHz: at the operating frequency of 11.42 GHz, the measured $|S_{11}|$ had values below -30 dB, while the measured $|S_{12}|$ was about -0.3 dB. A back-to-back measurement showed that the averaged loss of the mode launcher was about 0.2 dB higher than the value predicted by the simulation. This was likely due to the losses resulting from imperfect electrical contact in this non-brazed low-power-microwave test prototype.

3.2 Measurement of Electric Field Through Nonresonant Perturbation Technique

The electric field of the structure was measured through the use of the bead-pull technique. The adopted technique made use of the Steele non-resonant perturbation theory [3], employable when the measurement was performed on a traveling-wave structure such that presented in this paper. In the bead-pull technique, a small (in our case, dielectric) bead, attached to a nonconductive wire, was moved along the structure (in our case, along the waveguide axis), and the S_{11p} value was acquired at each sampled point. The electric field was proportional to the quantity $\Delta S_{11} = S_{11p} - S_{11np}$, where S_{11np} is the unperturbed value, i.e., the value when the bead was outside of the structure. When using the Steele theorem for the field measurement, the values at each sample point were acquired at a fixed frequency. In our case, we performed the measurements at the main resonant frequency, that is, 11.42 GHz.

A sketch of the experimental setup used for the bead-pull measurements is shown in Figure 4a. It was composed of a main metallic plate that held the stepping motor, necessary for the movement of the dielectric wire, and the device under test. A weight was attached at the wire end in order to maintain its tension.

Figure 4b shows a photo of the experimental setup. We used a two-port Agilent N5230A PNA-L microwave network analyzer that was interfaced to the stepping motor through a *LabView* script, able to command the wire movement as well as the sample rate. For the axial field measurement, an interval of 100 mm was chosen, with a sampling rate of 1 mm. The starting point was chosen at the circular waveguide's cutoff aperture. We chose a bead made of glue with a diameter of $\simeq 1$ mm as the perturbing object.

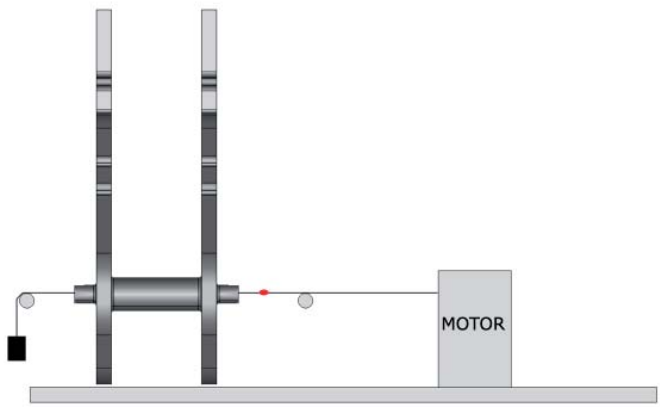

Figure 4a. A sketch of the bead-pull setup on the mode launcher. The perturbing dielectric bead is shown in red.

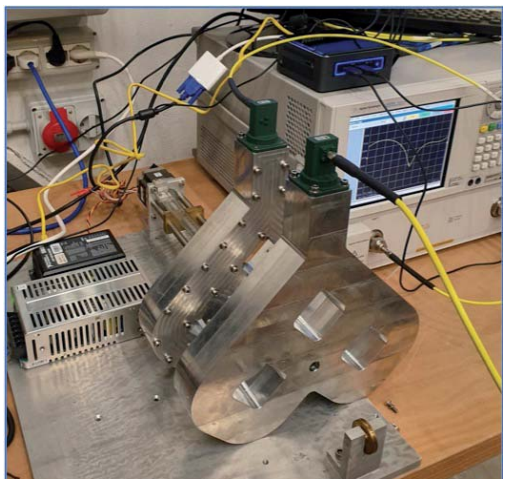

Figure 4b. A photograph of the bead-pull setup used for the E-field measurements on the mode launcher circular waveguide longitudinal axis.

Figure 5 shows the axial measurement of $\Delta|S_{11}|$ as a function of bead position performed on the device in back-to-back configuration, and the corresponding electric field *HFSS* simulation. Both curves were normalized with respect to their maxima. The two curves resulted in good agreement with each other.

The $\Delta|S_{11}|$ values were also measured inside the circular waveguide, along a circumference of radius $r = 4$ mm at the axial position $z = 90$ mm (i.e., at a position of electric-field maximum). For the azimuthal $|S_{11}|$ measurement, a circular flange was employed. The flange was rotated with a 10° step and a constant $\Delta|S_{11}|$ was measured. This further confirmed the field symmetry and the absence of competing quadrupolar modes.

4. Conclusion

A novel RF power coupler for an RF photoinjector, designed for high-brightness applications, has been presented. The design was partially automated by taking advantage of an ad hoc developed two-dimensional model with reduced simulation time. The proposed mode launcher was an X-band TM_{01} waveguide mode launcher that minimized dipole and quadrupole field components. A low-power-microwave version of the mode launcher was fabricated and successfully tested. This launcher features good back-to-back performance. We plan to test a brazed version of this mode launcher for a high-power test at SLAC.

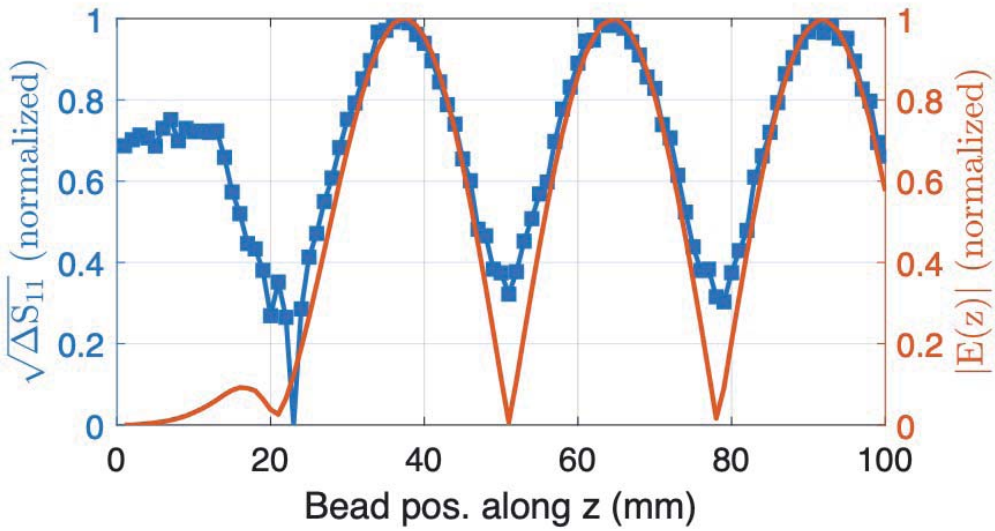

Figure 5. The measured $|S_{11}|$ values as a function of bead position (blue curves) and a comparison with the *HFSS* electric-field simulations (red curves).

5. References

1. D. Alesini et al., "Design of High Gradient, High Repetition Rate Damped C-Band RF Structures," *Phys. Rev. Accel. Beams*, **20**, March 2017, p. 032004.

2. A. D. Cahill, J. B. Rosenzweig, V. A. Dolgashev, S. G. Tantawi, and S. Weathersby, "High Gradient Experiments with X-Band Cryogenic Copper Accelerating Cavities," *Phys. Rev. Accel. Beams*, **21**, October 2018, p. 102002.

3. C. W. Steele, "A Nonresonant Perturbation Theory," *IEEE Trans. Microw. Theory Techn.*, **14**, February 1966, pp. 70-74.

4. A. Cahill, M. Dal Forno, and V. A. Dolgashev, "TM01 Mode Launcher for Use in High Brightness Photoguns," 7th International Particle Accelerator Conference, IPAC16, 2016, pp. 491-493.

5. G. Castorina, G. Torrisi, G. Sorbello, L. Celona, and A. Mostacci, "Conductor Losses Calculation in Two-Dimensional Simulations of H-Plane Rectangular Waveguides," *J. of Electromagnet. Wave*, 2019, pp. 1-10.

6. T.-H. Chang, C.-H. Li, C.-N. Wu, and C.-F. Yu, "Generating Pure Circular TE_{mn} Modes Using Y-Type Power Dividers," *IEEE Trans. Microw. Theory Techn.*, **58**, 6, 2010, pp. 1543-1550.

7. G. Castorina et al., "TM_{01} Mode Launcher with Quadrupole Field Components Cancellation for High Brightness Applications," *J. Phys.: Conf. Ser.*, 2018, p. 1067 082025.

James Clerk Maxwell Foundation *Newsletter* Available

The Winter 2020 edition of the *Newsletter* of the James Clerk Maxwell Foundation is available for free download at http://www.clerkmaxwellfoundation.org/Newsletter_2020_Winter.pdf. This edition contains an article by T. G. Mackay, "New Electromagnetic Waves: Voigt Surface Waves."

Electromagnetic Modeling of Scattered Signals of Opportunity: Challenges and Approaches

Davide Comite[1], Laura Dente[2], Leila Guerriero[2], and Nazzareno Pierdicca[1]

[1]Sapienza University of Rome
Italy
E-mail: davide.comite@uniroma1.it

[2]Tor Vergata University of Rome
Italy

Abstract

The possibility of exploiting signals of opportunity such as navigation signals for remote-sensing applications has been the object of extensive scientific research. Over the years, the potential of this technique has been mainly investigated for wind scatterometry and sea-surface altimetry, resulting in mission concepts and prototypes currently in orbit or under study. More recently, the potential of the Global Navigation Satellite System (GNSS) has attracted significant scientific and industrial interest, especially for land applications. The possibility of retrieving soil moisture and vegetation biomass by means of GNSS reflections, originally demonstrated through theoretical models and simulations, has been confirmed through the analysis of ground-based and airborne measurements. Even if these campaigns significantly contributed to consolidating the physics that is behind the interaction between navigation signals and some important geophysical parameters of the illuminated surface, a complete understanding of the experiments still needs further scientific efforts, especially for satellite observations.

In this work, we review the main progress that has recently been made at two universities of Rome, Sapienza and Tor Vergata, as well as by some other research groups. Current challenges and modeling approaches are summarized, focusing the attention on the potential offered by GNSS reflectometry with respect to more established passive and active remote-sensing techniques.

An electromagnetic model and the corresponding numerical simulator designed to characterize the field scattered under bistatic illumination and for the study of the signal at the receiver generated by sources of opportunity are reviewed and summarized.

1. Introduction

Global Navigation Satellite System reflectometry (GNSS-R) is an emerging technique potentially capable of enhancing or complementing more classical approaches for the remote sensing of the Earth. It can be generally viewed as a bistatic radar exploiting the illumination of the GNSS transmitter, thus offering the possibility of acquiring several simultaneous reflections by deploying a single passive system [1]. The GNSS-R technique was originally conceived for ocean mesoscale altimetry and scatterometry [2-5], and it was then extended to other fields. Several experiments carried out from aircraft, towers, and balloons, indeed preliminary demonstrated good sensitivity of GNSS-R observations to soil moisture and vegetation biomass (see, e.g., [6-10] and references therein).

The bistatic GNSS signal can be characterized by means of an integral radar equation and – among other parameters related to the system and the geometry of the observation – it depends on the electromagnetic properties of the illuminated surface [1, 5, 9, 11]. The scattered field is generated by the superposition of an incoherent and a coherent field, and it is thus described by introducing the bistatic normalized radar cross section (NRCS) and the surface reflectivity [12, 13]. Their relative contributions generally depend on whether the scattering mechanisms are coherent (e.g., generated by a smooth surface, determining reflections the phase of which is not random and can still be potentially tracked), or incoherent (e.g., generated by a very rough surface, the phase of the scattered signal being random and thus based on the same physical mechanisms as the conventional monostatic observations) [12].

Electromagnetic-modeling approaches simulating GNSS-R observations over land can represent a valuable

tool for improving and supporting the understanding of the main physical mechanism that contributes to the formation of the forward-scattered signal, which originates on the illuminated surface around the specular direction, and it is collected by a down-looking receiving antenna. Models can also provide efficient tools for the investigation of physical effects connected to bio- and geo-physical parameters of the surface under analysis, and to give both a synoptical and local view of the main potentialities and limitations for their retrieval.

We present a review of the research activity and space missions recently developed to understand and characterize the potentialities of the GNSS-R technique. This is focused on land applications and on the activities developed at the Sapienza and Tor Vergata universities in the framework of scientific projects funded by the European Space Agency (ESA).

2. An Overview of GNSS-R Space Missions and Research Activities

Over the years, the potential of the GNSS-R technique was mainly investigated for wind scatterometry [4, 5] and sea-surface altimetry [14]. Industrial and academic efforts resulted in mission concepts and technical demonstrators, which are currently closed, in progress, or under study (e.g., TechDemoSat-1, Cyclone Global Navigation Satellite System, GNSS reflectometry, Radio Occultation and Scatterometry onboard the International Space Station). The potential of GNSS-R to measure soil moisture and vegetation biomass, initially demonstrated through theoretical models and simulators designed for low-altitude platforms, was confirmed through the analysis of ground-based and airborne measurements [15-22]. These campaigns contributed to enhancing and consolidating the physical understanding of the measurement as well as to establishing and validating the background theoretical models.

In the last few years, a number of scientific experiments have been funded by ESA, NASA, and industry to promote the use GNSS-R data from spaceborne platforms. TechDemoSat-1 (TDS-1), in particular, was designed to enhance the understanding of the characteristics and capabilities of GNSS-R satellite signals for ocean and land applications [23-25]. The TDS-1 mission provided unprecedented access to a large set of spaceborne GNSS-R data, with complete latitude coverage, including the polar areas. Thanks to ESA support, the relevant dataset was made freely and publicly available through the MERRByS dissemination portal (www.merrbys.co.uk). At the time of writing, this effort had resulted in more than one hundred high-impact journal papers being published by researchers around the world, spanning a wide range of applications, including oceans and land targets (see, e.g., [24-26]).

Based on TDs-1 data, in [28] the capability of spaceborne GNSS reflections to retrieve changes in the soil moisture was investigated. The analysis showed a variation of the collected power up to 7 dB when observing signals reflected from land regions having different soil-moisture content.

From a different perspective, the research activities on ocean applications mentioned above have enabled advanced investigations of non-geophysical effects, giving the unique opportunity to design, implement, and test corrections and mitigation strategies to improve the GNSS-R measurement calibration.

The experiment GEROS-ISS – which stands for GNSS reflectometry, radio occultation, and scatterometry onboard the International Space Station (ISS) – was also successfully proposed to ESA by a group of industrial and research partners [29, 30]. The experiment was designed to again exploit reflected signals from the GNSS L-band constellation for the remote sensing of the Earth, mainly focusing on the study of climate change. The two primary objectives of the mission consist in the determination of the altimetric sea-surface height of the oceans and of the ocean surface's mean-square slope, which, as is well known, are related to ocean roughness and wind speed.

Some secondary goals have also been designed, including atmosphere/ionosphere sounding using refracted GNSS signals (i.e., radio occultation, GNSS-RO), and the remote sensing of land surfaces using the reflected signal.

The NASA Cyclone Global Navigation Satellite System (CYGNSS) mission, launched in December 2016, carries onboard a GNSS-R receiver payload with analogue characteristics such as those carried by the TDS-1 mission. However, CYGNSS was conceived as a demonstrator mission for the monitoring of the fast dynamics of tropical cyclones and storms [31]. To this aim, it was designed to meet a different set of mission parameters. As a matter of fact, to achieve its objectives (i.e., number of observatories, accurate onboard attitude control, accurate antenna characterization, etc.), the mission was conceived to operate through a constellation of eight small satellites. This makes CYGNSS the largest satellite GNSS-R available recording at the time of writing, providing dense measurements in the ±35° latitude band with an average repetition time of a few hours.

Different research groups worldwide (the University of Michigan, the United States National Oceanic and Atmospheric Administration, and the Jet Propulsion Laboratory, among others) have been developing and testing retrieval algorithms for both marine and land remote-sensing applications [31-35]. However, to date significant discrepancies have been found between CYGNSS wind-performance estimates reported by different teams and different observatories. Among other factors and technical aspects, these inaccuracies possibly suggest the presence of unresolved technical issues, mainly related to the calibration of the GNSS-R returns.

Based on CYGNSS data, in [35] the authors proposed an empirical study to characterize the effects of topographic parameters on the waveform associated with GNSS reflections.

As GNSS-R technology goes on evolving and new future missions are being envisaged and proposed, undoubtedly all possible aspects related to measurement calibration will require a new and accurate phase of study to achieve a satisfactory level of measurement accuracy. This is even more important when satellite constellations are involved, which require additional accurate inter-calibration strategies to achieve data consistency across different observations. In the authors' opinion, these goals cannot be satisfactorily met without a theoretical study of the electromagnetic scattering in a GNSS-R system.

In the last two years, land applications of GNSS-R have been investigated by the Sapienza and Tor Vergata universities in conjunction with other industrial and academic partners in the framework of a project funded by ESA. The main outcomes of the project to date are still being published (more information can be found in [27, 36, 37]).

We can anticipate that in general, previous observations about the sensitivity of the GNSS reflections to land bio-geophysical parameters, i.e., the soil moisture and the forest biomass, were confirmed. Thanks to this study, which corroborated the findings of other work from the literature, the sensitivity to the target parameters can be now considered to be established and to be generally satisfactory in the case of satellite observations, even though further studies are needed to accurately quantify the expected performance.

The ESA project supported the design of an ad-hoc numerical simulator (the main scheme of which is summarized in the upcoming sections). The activity demonstrated that the *average* behavior of the signal (i.e., its dynamic as a function of the target parameters once other effects are properly filtered out) is well reproduced by model. As a matter of fact, the study highlighted that the increase of reflectivity with soil moisture, and its decrease for increasing forest biomass, could be reproduced by models if the coherent and incoherent terms contributing to the scattering signals as well as the effect of topography were properly modeled and taken into account [35].

As far as the spatial resolution of the GNSS-R is concerned, it is currently assumed to be of the order of kilometers for flat surfaces, when the signal can be considered mainly coherent. However, it can significantly degrade as the scattering becomes incoherent. Some interesting studies focused on both ocean and land targets were proposed (see, e.g., [36, 38, 39]). More investigations are needed to enhance the understanding of this important aspect, accounting for the characteristics of the illuminated surface and the radar system in a systematic way.

One important technical aspect that can theoretically limit the accuracy of the retrieval in GNSS-R is the sparse nature of the measurements, which is an intrinsic characteristic of the technique. A GNSS-R dataset cannot provide an image of the illuminated area, whilst the relevant acquisition strategy cannot be characterized by a fixed repetition cycle. As a consequence, some sort of data-aggregation strategy in both space and time must be carried out to come out with a product that provides the desired raster (i.e., gridded) format. This procedure necessarily reduces the spatial resolution of the final product, which becomes dependent on the scattering features of the illuminated area. As a matter of fact, noisier (i.e., variable and fluctuating) data are expected to require a longer temporal averaging scheme, the process for which has an unavoidable detrimental effect on the resolution.

In other words, the main drawback of the GNSS-R technique can be represented by the need of ancillary data for retrieving the target parameters, mainly to compensate for the effect of intrinsic features of the scattering phenomenology, including the topography of the illuminated area and the inhomogeneous nature of the Earth's surfaces. It should be mentioned that the topography (typically described by digital elevation models), is in general not an issue for airborne observations, where the illuminated area is not enough large to be affected by this type of spatial variations. Instead, satellite applications, even if they can provide global coverage with enhanced repetitions, cannot ignore this type of variation [37].

As mentioned above, the satellite GNSS-R technique can be affected by poor coverage and temporal resolution. A constellation must be considered to overcome this problem. More importantly, not only do many parameters determine the response of the illuminated area, but in general conditions, the observations (i.e., the pattern of the specular points along the track of the satellite) are not regularly repeated over subsequent observations (as can be the case for conventional image radars). In addition, observing a set of points lying within inhomogeneous areas can determine large fluctuations, even where the signal could be expected to be prevalently *coherent* (i.e., as generated by an essentially flat region).

To summarize, many sources of signal fluctuations can be observed due to the non-systematic sampling over time and space of an inhomogeneous Earth's surface and due to the influence of the topography. These effects have to be mitigated by implementing an ad-hoc incoherent integration process. Only by accurately characterizing these intrinsic variabilities of the GNSS reflections can one can expect to achieve enhanced retrieval performance of the target quantities with respect to other, well-established, passive and active remote-sensing approaches.

The preliminary attempts at retrieval approaches, essentially based on average quantities (in time or space), revealed a certain capability of estimating the

target's parameters (such as the soil moisture). However, the comparison of retrieval approaches based on non-averaged observations with reference data was generally not satisfactorily. Mitigating the impact of the nuisance parameters affecting the reflected signal should in fact be considered a priority, but this can only be performed by studying the effect of roughness and theoretically characterizing the dynamics of the scattered signal.

On this basis, the availability of accurate but general and flexible modeling approaches looks very important. The state-of-art of the proposed techniques will be briefly reviewed in the following sections. The modeling approaches developed by our research group will also be summarized.

3. Modeling Approaches

GNSS-R observations are typically presented in the form of delay Doppler maps (DDM), which essentially describe the power at the output of the signal correlator [1]. From a theoretical viewpoint, the delay Doppler map is evaluated by solving the bistatic scattering equation, originally proposed in [5], and revised in [11] to account for the transition between coherent and incoherent scattering. This approach has been used by different authors, but mainly to describe GNSS reflection by the ocean.

Based on the bistatic radar equation, several modeling approaches have been proposed in the last decade, which will be summarized in the following. It is worth mentioning that in the case of space-borne GNSS-R observations, the area contributing to the collected power can be much larger than for low-altitude sensors. In this case, some aspects become particularly relevant, such as the low magnitude reached by the reflected signal (that results in limited signal-to-noise ratios), the effect of the topography, as well as of the land-cover inhomogeneity.

To demonstrate the potentiality of GNSS-R in monitoring forest biomass, a set of theoretical simulations of the specular scattering coefficient of a forested area was presented in [40].

An end-to-end performance simulator was proposed in [41]. The software considered both the ionospheric and the tropospheric effects, as well as the system noise. It was also updated to include the effect of the topography [42], although with a non-electromagnetic approach. Among other features, the tool can simulate the transmission and reception at satellite orbits; locate the specular reflection point and the glistening zone (see [1] for a definition of this concept); include the antenna's features and the signal correlator; and generate the sea-surface scattering coefficient and the delay Doppler map over the considered area.

In [43], a GNSS-R simulator was designed for the study of the role of the polarization and of forest canopy. A well-established bistatic scattering model, based on the first-order radiative transfer model, was implemented. An open-source software library, *WAVPY*, was proposed in [44]. The library provided a set of object-oriented classes used to characterize a realistic GNSS-R scenario, and it implemented most of the functionalities required for GNSS-R data processing.

The response of vegetated terrains was modeled in [45], where the authors presented a detailed analysis of the scattering generated during the growing season of corn. The simulator was based on the coherent bistatic-scattering model described by the same group in [46]. The software was used to study the effects of the soil moisture and surface roughness on the GNSS reflection and to analyze the sensitivity to various land parameters. It was demonstrated that specular reflections can dominate the diffusely scattered contribution in the presence of moderate roughness, regardless of the corn-field's row structure or the polarization of the incident field.

A closed-form model for the coherent normalized radar cross section (NRCS) in general conditions and accounting for the sphericity of the wavefront of the impinging wave was proposed by the authors in [36]. The model provided a tool to efficiently simulate the power at the receiving antenna, even in the presence of inhomogeneous media. As the model relied on the definition of a coherent normalized radar cross section [12, 47], it did not provide information on the phase of the scattered signal.

To study both the amplitude and phase of the reflected signal, also accounting for the topography of the illuminated areas (i.e., of multiple elevations), a full-wave solution of the scattering was proposed in [48, 49], applying the Kirchoff approximation (KA) of the scattering [12]. The results showed that the phase of the first Fresnel zone can be random under certain conditions. The power contributed by the first Fresnel zone was a small fraction of that over a zone having a size of 10 × 10 km, which was assumed to be the region mainly contributing to the collected power. It was also observed that the power ratios of the numerical simulations were larger than those of the incoherent geometric-optics model, and smaller than the coherent model for small heights of the surface.

The Soil and Vegetation Reflection Simulator (*SAVERS*) was originally proposed in [9] for the simulation of low-altitude receivers (that do not need to introduce a digital elevation model, or DEM, to describe the illuminated area). The model exploited the definition of coherent normalized radar cross section [36, 47] to numerically retrieve the power of the reflected GNSS-R signal and the delay Doppler maps of the illuminated area. The scattering problem was solved through the integral bistatic radar equation, following [9], weighting the contributions of all scatterers on the surface by the Woodward ambiguity function. The performance of the software was tested using the data collected in the Land Monitoring with Navigation

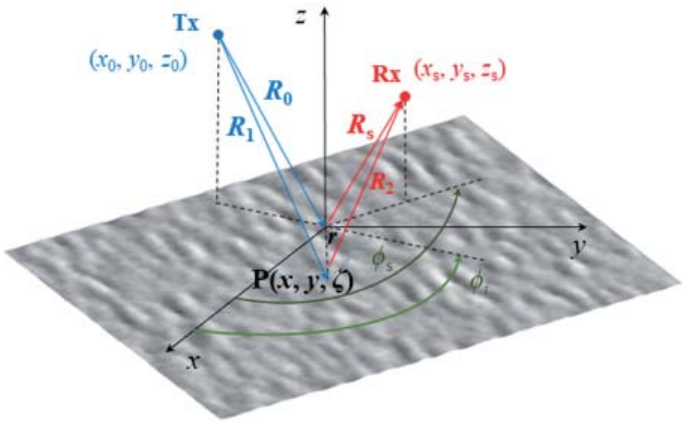

Figure 1. The essential geometry of the bistatic scattering. T_x and R_x represent the arbitrary positions of the transmitting and receiving antennas. A forward-scattering alignment convention was assumed (backscattering $\varphi_s = 180°$, specular $\varphi_s = 0°$). The azimuth incident angle was set to 0°.

signals (LEiMON) campaign by a ground-based sensor, and in the GNSS Reflectometry Analysis for biomaSS (GRASS) campaign by an airborne sensor [15, 16]. Overall, it was demonstrated that the simulator could be a valuable tool for an accurate interpretation of GNSS-R measurements over bare, agricultural, and forested areas. *SAVERS* was recently updated to model the signal collected at satellite altitudes, thus including the effect of topography. The software was preliminary presented in [37]. The updated version of *SAVERS* included the contributions of both the coherent component of the mean soil surface, as well as the incoherent component due to vegetation volume and rough soil scattering.

4. Coherent Scattering: A Closed-Form Model for GNSS-R

To efficiently simulate the signal at the receiving point in the presence of realistic topography (i.e., the soil spatial variations described by a digital elevation model) and inhomogeneous media, a closed-form expression for normalized radar cross section was proposed by some of the authors in [36].

An incident plane wave or a plane wave confined within a finite area *A* (controlled by the antenna footprint) are both conditions that cannot be reproduced in real experiments. As a matter of fact, in practice, the impinging wave is produced by an antenna with a spherical wave front (locally plane in the far field), and a power density angular distribution determined by the antenna pattern. The coherent scattering accounting for such realistic conditions was originally proposed in [47], but introducing a closed-form solution only for directions very close to the nadir. To characterize the GNSS signal or any geometry described by a source of opportunity, we extended the scattering solution to the most general case [36], thus considering the receiving antenna placed in an arbitrary position (x_s, y_s, z_s).

The essential geometry of the problem is reported in Figure 1, where R_1, R_2 represent the path lengths from an arbitrary point on the surface, indicated by the position vector $\mathbf{r}$, to the transmitting and receiving antennas placed at heights z_t and z_r, respectively. The antenna beams are Gaussian, with half beamwidths $\beta_i\,(i = 0, s)$, and the distance from the origin to the transmitting and receiving antennas are R_0 and R_s, respectively. For simplicity, the transmitting antenna is placed in the xz plane, and it illuminates along a zenith direction θ_0 an area on the surface having an approximate size equal to $R_0\beta_0/\cos\theta_0$. Under the Kirchoff-approximation formulation, in the presence of a spherical incident wave $E_i = e^{-jk_0R_1}/R_1$ and with a Gaussian tapering for the beams [13, 47], the scattered field, E_s, is given by

$$E_s = \frac{-j}{4\pi}\int_{-\infty}^{+\infty}\int_{-\infty}^{+\infty} F_{pp}(\mathbf{r})\,k_0\,(\mathbf{n}\bullet\mathbf{q})\,\frac{e^{-jk_0(R_1+R_2)}}{R_1R_2}$$

$$e^{-g_0^2\left(a_0x^2+y^2\right)}e^{-g_s^2\left(a_sx^2+b_sy^2+c_sxy\right)}dxdy\,, \qquad (1)$$

with $\mathbf{n}$ being the unit vector normal to the surface and $\mathbf{q} = -k_0\nabla(R_1+R_2)$; $g_i = 1/R_i/\beta_i$, with $i = 0, s$; $a_0 = \cos^2\theta_0$. Similarly, a_s, b_s, c_s are elementary trigonometric expressions that are a function of the scattering direction, calculated by projecting the Gaussian antenna pattern onto the horizontal xy surface. These expressions are not reported for brevity, but they can be found in [36]. Starting from the formulation in Equation (1), to achieve a closed-form expression, a higher-order expansion was proposed for $R_{1,2}$ that was different from what was done in [47], where the expansion was limited to the first two terms since, in that case, only directions very close to the nadir were considered. On this basis, assuming small slopes and considering Equation (1), a closed-form expression for the squared magnitude of the coherent field scattered by the rough surface can be achieved. Such an expression allows for simple characterization of the normalized radar cross section of the coherent component for arbitrary extensions of the illuminated area *A*, given by the following compact equation [36]:

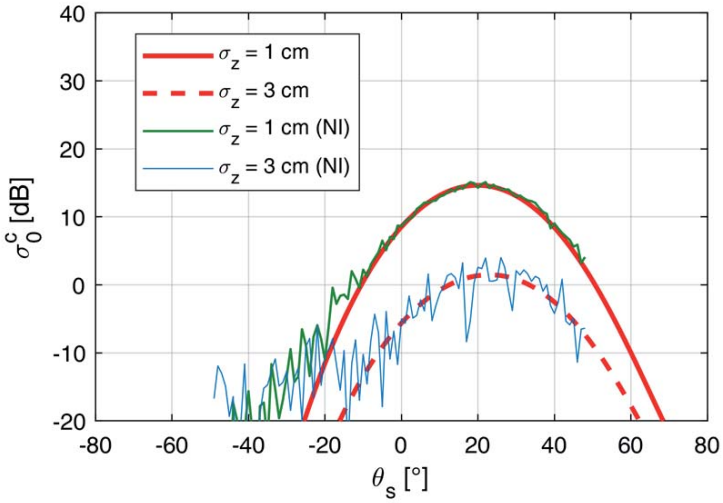

Figure 2. A comparison between the coherent normalized radar cross section within the plane of incidence obtained with Equation (2) and with the numerical integral (NI) given by Equation (1) for $\beta_{0,s} = 10°$, $\theta_0 = 20°$. Two rms heights were considered for the surface profile $\zeta(x,y)$ with correlation length L equal to 12 cm (from [36]).

$$\sigma_{pp}^{\circ C}(\theta_0,\theta_s,\varphi_s) = \frac{4\pi R_s^2 \left\langle E_s E_s^* \right\rangle_{n=0}}{\left|E_t\right|^2 A}$$

$$= \frac{k^2 \left|a_{pp}\right|^2}{4\sqrt{a_3 a_4}} e^{-k_{dc}^2 \sigma_z^2} e^{-\frac{k_{dy}^2}{4a_3}} e^{-\frac{k_{dx}^2}{4a_4}} e^{-\frac{k_{dy}^2 \delta^2}{16 a_3 a_4}} e^{\frac{k_{dx} k_{dy} \delta}{2 a_3 a_4}} . \qquad (2)$$

In Equation (2), the expressions for a_1, a_2, a_3, a_4 and δ are simple but lengthy trigonometric expressions depending on the incident and scattering angles [36]. They can be derived after some algebra by substituting the approximated expression of R_1 and R_2 in Equation (1). The propagation vector components associated with the linear phase term in Equation (2) are given by $k_{dx} = k_0(\sin\theta_s \cos\varphi_s - \sin\theta_0)$ $k_{dy} = k_0(\sin\theta_s \sin\varphi_s)$, and $k_{dz} = k_0(\cos\theta_0 + \cos\theta_s)$. They represent the differences between the impinging and the scattering propagation vectors pointing to and originating from the origin, respectively. As discussed in [47], for antennas placed at a finite distance from the surface, plane-wave illumination can be achieved only for very small beamwidths. This is because large beams determine large footprints, making the quadratic phase of the illumination not negligible.

We should mention that the integration area in Equation (1) becomes larger for increasing values of R_0 and R_s. When a satellite geometry is considered (R_0 and R_s of the order of 500 km to 600 km or more), a numerical solution of the integral could therefore become extremely lengthy and inconvenient, and parallel computing should be implemented [48]. In this respect, the closed-form expression proposed in [36] can be very useful for an efficient simulation of the power at the receiving antenna.

The accuracy of the formula in Equation (2) was numerically validated in [36]. Figure 2 reports a comparison among the bistatic normalized radar cross sections within the plane of incidence for a metallic rough surface, setting the incidence angle equal to 20°. The numerical solution of the integral in Equation (1) was carried out by means of a Monte Carlo approach based on 30 realizations of a Gaussian surface. Very good agreement with Equation (2) was visible for both values of the surface roughness standard deviation (see the figure legend). As expected, the normalized radar cross section exhibited the maximum value at the specular direction, which was the region mainly contributing to the power at the receiving antenna in GNSS-R systems.

5. Characterization of the Received Power

The expression given by Equation (2) can be included within the radar equation for a distributed target by defining an effective beamwidth, β_c, for the transmitting and receiving antennas [50]. A similar test was experimentally done in [51] for a ground-based configuration looking close to nadir. It was approached numerically in [36] for a metallic surface by connecting the power predicted by the radar equation and the power dictated by the image theory (more details on this aspect can be found in [36]).

This approach requires the definition of an effective beam for the antenna that is used to test the surface. Once such an optimum value of β_c is identified, through Equation (2) it is possible to define an active area on the surface (shown in Figure 3) that represents the portion of the illuminated surface actually contributing to the coherent field collected at the receiver point. Such an active area can collapse into a single point (i.e., the specular point predicted by the conventional Fresnel coefficient) when the illuminated surface is not truncated and the wavefront of the impinging wave is plane.

In other words, Equation (2) provides the definition of the *radiation pattern* of an illuminated area having a size determined by the actual beamwidth of the transmitting antenna (i.e., β_0), observed by the receiving antenna

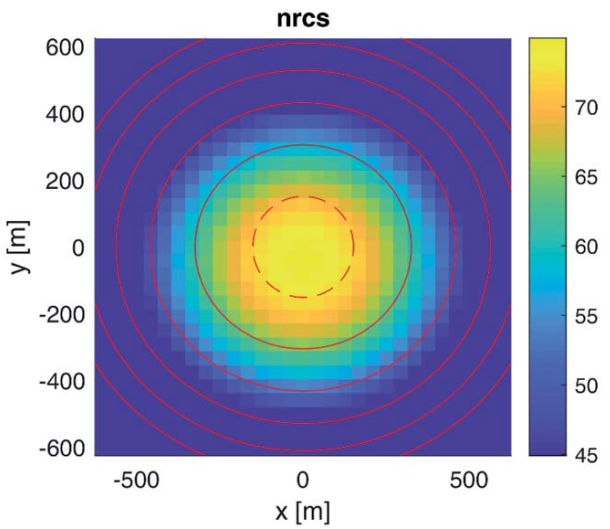

Figure 3a. The pattern of the coherent normalized radar cross section over a gentle illuminated surface ($L_z = 6$ m, $\sigma_z = 10$ cm). The active area was determined by setting β_c to satisfy the image theory. A reasonable correspondence was found among the size of the first Fresnel zones (solid red circles) and the -3 dB isoline of the coherent normalized radar cross section (dashed circles).

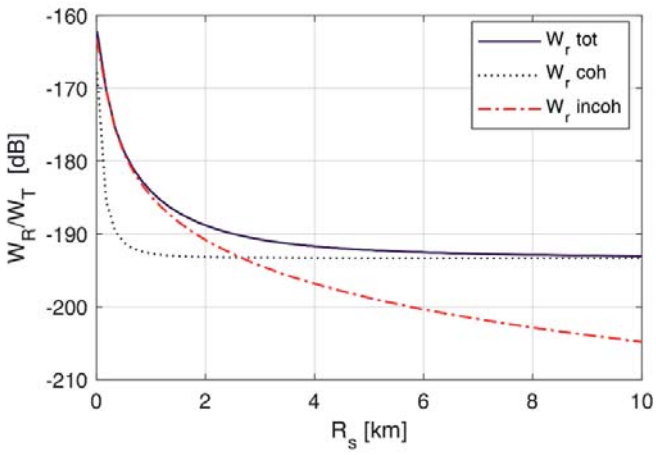

Figure 3b. The received power by applying the radar equation for distributed targets: the total power as well as the coherent and incoherent powers are reported as functions of the receiver height. The actual beamwidths of the antennas were equal to 20°.

having an actual beamwidth β_s. The pattern defined by Equation (2) can be profitably used in a simulator based on the bistatic radar equation [5], even in the presence of a digital elevation model, which is the case of the updated version of *SAVERS*.

By including both the coherent and incoherent contributions (under the Kirchoff approximation) within the radar equation, it is indeed possible to conveniently describe the power at the receiver and to analyze the relative contributions between the two components. Figure 3b reports the power as a function of the receiver height for $R_0 = 20\,000$ km. As is visible due to the different dependence from $R_{0,s}$ [9], one can observe a change of scattering regime. This demonstrated that an accurate modeling of the coherent component is very important for a correct prediction of the receiving power in GNSS-R applications.

6. Inhomogeneous Media and Spatial Decorrelation

Both the normalized radar cross section and the reflectivity are typically achieved by assuming scattering by *frozen* surfaces, i.e., with antennas placed in a certain position, neglecting the movement. Their definitions also require homogeneity of the electromagnetic features. In this condition, the scattering far from the surface presents *phase coherence* [4, 13]. However, the relative movements of the transmitter and receiver, as well as the random nature of the illuminated surface, can significantly affect the coherence of the scattered field. In addition, the presence of inhomogeneities within the illuminated area can determine fluctuations of the received power. Losses of *spatial coherence* determine an autocorrelation function broadening over time [52, 53]. This can be problematic for integration of the echoes at the receiver.

Since the geometry of the GNSS-R is intrinsically bistatic, and the transmitted power is not comparable with that of a monostatic radar system, to increase the SNR the receiving system performs a coherent integration (i.e., a cross-correlation with a clean replica) of the scattered signal over a certain time interval [1, 9]. An incoherent integration for the reduction of intrinsic fluctuations of the collected signals is also implemented [23]. These operations should be performed on a time interval properly sized to account for the coherence features of the phenomenon under observation.

When looking at real GNSS reflections, a strong variability of the signal can indeed be observed, even over areas where the scattered field would be expected quite stable. For instance, this is the case for flat and homogeneous steady surfaces (e.g., flat soils), where the coherent component is expected to be dominant [54]. In the limiting case of perfectly plane surfaces, excluding noise and instrument factors, the purely coherent signal reflected in the specular direction should not exhibit any random variability.

To characterize the coherent features of the GNSS-R signal, a full-wave analysis of the *spatial decorrelation* experienced by the field scattered around the forward direction was preliminary developed by the authors in [55]. The scattering model was again based on the Kirchoff

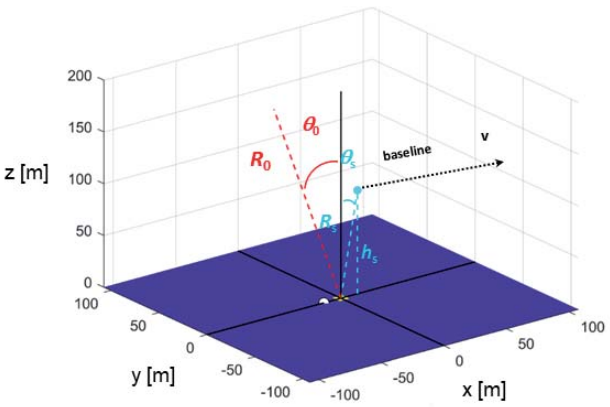

Figure 4a. The geometry of the bistatic observation.

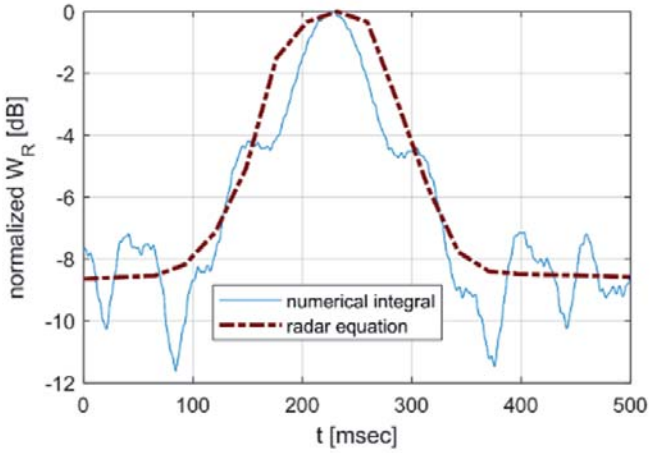

Figure 4b. The power received from an inhomogeneous flat surface.

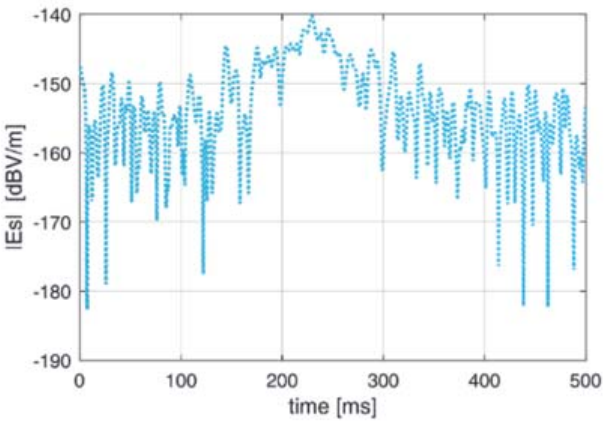

Figure 4c. The power received from an inhomogeneous rough surface.

approximation (see Equation (1)), including again the wavefront sphericity [30, 48] and a shaping factor for the radiation patterns of the antennas (which should not necessarily be a Gaussian function; a rectangular window can also be included in a first approximation).

The geometry of the problem is depicted in Figure 4a, where the receiver is now moving at a constant velocity in a direction parallel to the soil interface. $\theta_0, \varphi_0, \theta_s, \varphi_s$ indicate the pairs of zenith and azimuth angles identifying the incident and scattering directions, respectively; $R_{0,s}$ are the distances of the two antennas from the origin of the reference system; and the white spot is the position of the specular point. We performed an *L*-band solution of the Kirchoff approximation integral extended over the intersection of the illuminated area and the receiver discrimination capability (i.e., the receiver beam of the delay/Doppler discrimination). The receiver was in movement at a constant height h_s, thus defining a variable θ_s at an altitude ranging from 100 m, as for the airborne case, to hundreds of kilometers for the spaceborne case. The transmitter was steady and placed at 20,000 km, as for GNSS. Depending on the speed, v, of the receiver, the scattered field was evaluated over a certain baseline, starting from zero up to B_{max}. The solution was carried out setting $\theta_0 = 15°$, $h_0 = 100$ m,, $v = 60$ m/s, with a field amplitude at the source equal to 1 V/m.

6.1 Modeling Inhomogeneous Media

Based on the geometry depicted in Figure 4a, we illustrated here how the normalized radar cross section introduced in Equation (2) could be exploited to include the presence of inhomogeneous media within the illuminated area (more information can be found in [36]). A metal patch at the center of the illuminated surface, surrounded by the dielectric media, was therefore considered in Figure 4a. A full-wave numerical solution (which was computationally manageable in this case since the receiving antenna was placed at low altitudes) was compared with the solution given by Equation (2) in conjunction with the radar equation (see [36]). This approach essentially provided a way to introduce a *local* characterization of the coherent scattering (contrasted with the *global* description necessarily introduced by the Fresnel coefficient).

The power at the receiver as a function of the time (or, equivalently, as a function of the position of the moving receiver) is reported in Figures 4b and 4c, considering a flat and a rough dielectric surface surrounding the metal. Figure 4b also reports the power achieved by applying the solution based on Equation (2), which presented a smooth behavior that nicely approximated the rigorous solution. The non-approximated solution presented a fluctuating behavior due to the interference of Fresnel zones encompassing the dielectric/conductive materials, with a maximum occurring when the specular point crossed the patch's center. This fluctuation could not be described by the model based on the definition of the normalized radar cross section [36], which was anyway computationally much more efficient, since it did not require a full-wave solution of the scattering.

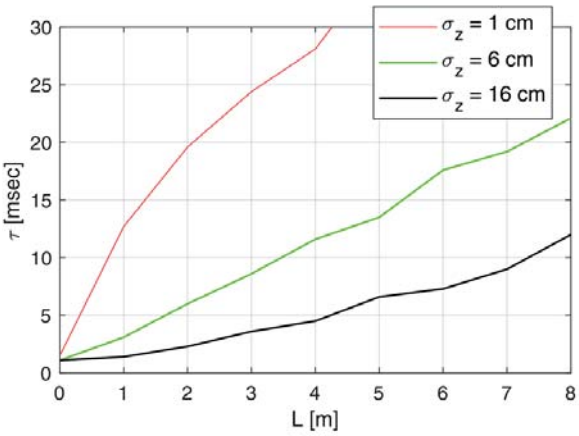

Figure 5. The estimated τ for a rough surface with different rough profiles (see legend); an exponential fitting was also generated. More information can be found in [55].

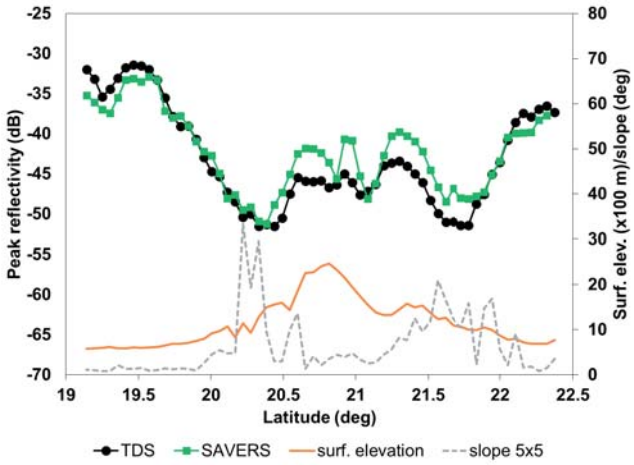

Figure 6. A comparison between observed peak reflectivity (black) along a TDS-1 descending pass over Tibesti and the simulated peak reflectivity (green) (from [37]).

6.2 Spatial Decorrelation of the Scattering

To analyze the impact of the surface inhomogeneities as well as of the parameters of the surface random process (i.e., the rms heights, σ_z, and the correlation length, L) on the decorrelation time, τ, of the electric field, the frequency-domain scattered electric field, E_s, was numerically evaluated over a suitable time interval, while the receiver moved along its trajectory (i.e., the baseline in Figure 4a) around the forward direction. The correlation time, τ, can be evaluated by estimating the auto-covariance function of E_s and by considering the corresponding $1/e$ beamwidth [55]. In this condition, by applying the formulas given in [4, 52, 53] (based on simple physical considerations), we expected a correlation time, τ, of about 2.4 ms. Figure 5 reports the numerically achieved τ as a function of L for two values of the surface roughness; one realization of the random process was considered. For $L = 0$, τ corresponds to the theoretical value retrieved with [52]. For increasing roughness correlation lengths, the correlation time of the signal significantly increased. For instance, this means that a surface with elevation changes of about 10 cm in the vertical dimension and L of the order of 5.6 m in the horizontal dimension would produce signal fluctuations with a temporal scale of ~30 ms. This was a case of an almost flat area with gentle roughness, as, for instance, in the case of a flat agricultural plain.

Although the scattering mechanisms can be considered practically *specular* for such a plain surface, signal fluctuations with long correlation time can exist, and they are not effectively smoothed by the incoherent integration because of the small number of independent samples within the incoherent integration time. Further investigations are in progress by our research group, especially considering higher altitudes, which are the case of the GNSS-R geometry of current spatial missions based on satellite platform. This activity can provide important information about the time interval to be selected for the cross-correlation of the received waveforms and useful insights for understanding and improvement of the retrieval of bio-geophysical parameters.

7. SAVERS

In the framework of an ESA-funded project, SAVERS has been recently upgraded in order to simulate GNSS-R observations by space-borne receivers, taking into account the inhomogeneity of the large observed area in terms of topography and land cover. The information provided by a digital-elevation model and a land-cover map is processed by the simulator to determine the local elevation, slope, aspect, and vegetation cover. This allows the simulator to correctly compute the local incidence and scattering angles, and to accurately identify and represent the area in near-specular conditions mainly contributing to the reflected signal. Taking into account the polarization rotation and the down-looking antenna gain, the contribution of each elemental areas is simulated, weighted, and integrated by the radar equation, and the delay Doppler map (DMM) is estimated. The coherent scattering in SAVERS is modeled by using the *radiation pattern* provided by Equation (2), which avoids the full-wave simulation of large areas, the receivers being at about 500 km.

In order to evaluate the simulator's performance in the presence of a complex topography, the upgraded version of SAVERS was validated in [37] against TDS-1 observations over the deserted and volcanic region of Tibesti in Chad. The main result of that work is reported in Figure 6 (please refer to [37] for more details), where the TDS-1 peak reflectivity observed along a pass over the relief is compared to the simulations. The comparison exercise showed that SAVERS can reproduce the strong effect of the topography on the reflectivity, correctly simulating an evident decrease when

the receiver moved from a flat region (beginning and end of the pass shown in Figure 6) to the mountains. The bias between simulations and observation over some areas was mainly due to the lack of knowledge about the small-scale surface-roughness variations along the pass.

8. Conclusion

An overview on the potentialities of the GNSS-R technique has been provided in this paper. Current challenges and research activity have been described and summarized, giving emphasis to the studies developed at two universities of Rome, Sapienza and Tor Vergata.

Efficient modeling approaches for the realistic characterization of the scattering by sources of opportunity have been reviewed, discussing the possibilities of simulating the power at the receiver in the presence of the Earth's topography and inhomogeneous media.

Ongoing investigations on the correlation features of the field scattered by a rough surface have also been briefly summarized. A preliminary analysis on the impact of the surface parameters (i.e., the surface rms heights and the correlation length) has been discussed, demonstrating that the spatial decorrelation of the field can be strongly dependent on the electromagnetic features of the illuminated surface. Further analysis to assess the role of the geometry and of system parameters, also accounting for satellite-borne receivers, as well as studies about the sensitivities of the GNSS reflections to bio-geophysical parameters, are in progress.

These investigations can provide very important information about the phenomenology of the scattering of signals of opportunity, and a powerful tool to make GNSS-R a mature remote-sensing technique.

9. Acknowledgments

This work has been carried out in the framework of the project ESA/ESTEC, CONTRACT n. 4000120299/17/NL/AF/hh.

10. References

1. V. U. Zavorotny, S. Gleason, E. Cardellach, and A. Camps "Tutorial on Remote Sensing Using GNSS Bistatic Radar of Opportunity," *IEEE Geoscience and Remote Sensing Magazine*, 2, 4, December 2014, pp. 8-45.

2. M. Martin-Neira, M. Caparrini, J. Font-Rossello, S. Lannelongue, and C. Serra Vallmitjana, "The PARIS Concept: An Experimental Demonstration of Sea Surface Altimetry Using GPS Reflected Signals," *IEEE Transactions on Geoscience and Remote Sensing*, **39**, 1, January 2001, pp. 142-150.

3. S. T. Lowe, J. L. LaBrecque, C. Zuffada, L. J. Romans, L. E. Young, and G. A. Hajj, "First Spaceborne Observation of an Earth-Reflected GPS Signal," *Radio Science*, **37**, February 2002, pp. 7-28.

4. C. Zuffada, T. Elfouhaily, and S. Lowe, "Sensitivity Analysis of Wind Vector Measurements from Ocean Reflected GPS Signals," *Remote Sens. Environ.*, **88**, 3, May 2003, pp. 341-350.

5. V. U. Zavorotny and A. G. Voronovich, "Scattering of GPS Signals from the Ocean with Wind Remote Sensing Application," *IEEE Transactions on Geoscience and Remote Sensing*, **38**, 2, March 2000, pp. 951-64.

6. D. Masters, V. Zavorotny, S. Katzberg, and W. Emery, "GPS Signal Scattering from Land for Moisture Content Determination," IGARSS'00, 2000, pp. 3090-3092.

7. D. Masters, P. Axelrad, and S. Katzberg, "Initial Results of Land-reflected GPS Bistatic Radar Measurements in SMEX02," *Remote Sensing of Environment*, **92**, 2004, pp. 507-520.

8. S. J. Katzberg, O. Torres, M. S. Grant, and D. Masters "Utilizing Calibrated GPS Reflected Signals to Estimate Soil Reflectivity and Dielectric Constant: Results from SMEX02," *Remote Sensing of environment*, **100**, 2006, pp. 17-28.

9. N. Pierdicca, L. Guerriero, R. Giusto, M. Brogioni, and A. Egido, "SAVERS: A Simulator of GNSS Reflections from Bare and Vegetated Soils," *IEEE Transactions on Geoscience and Remote Sensing*, **52**, 10, October 2014, pp. 6542-6554.

10. H. Carreno-Luengo, A. Camps, J. Querol, and G. Forte, "First Results of a GNSS-R Experiment from a Stratospheric Balloon over Boreal Forests," *IEEE Transactions on Geoscience and Remote Sensing*, **54**, 5, May 2016, pp. 2652-2663.

11. A. G. Voronovich and V. U. Zavorotny, "Bistatic Radar Equation for Signals of Opportunity Revisited," *IEEE Transactions on Geoscience and Remote Sensing*, **56**, 4, December 2017, pp. 1959-1968.

12. F. T. Ulaby, R. K. Moore, and A. K. Fung, *Microwave Remote Sensing Active and Passive-Volume II: Radar Remote Sensing and Surface Scattering and Enission Theory*, Norwood, MA, Artech House Publishers, 1986.

13. P. Beckmann and A. Spizzichino, *The Scattering of Electromagnetic Waves from Rough Surfaces*, Norwood, MA, Artech House, Inc., 1987, p. 511.

14. A. Rius, O. Nogués-Correig, S. Ribó, E. Cardellach, S. Oliveras, E. Valencia, H. Park, J. M. Tarongí, A. Camps, H. van der Marel, and R. van Bree, "Altimetry with GNSS-R Interferometry: First Proof of Concept Experiment," *GPS solutions*, **16**, 2, April 2012, pp. 231-241.

15. A. Egido et al., "Global Navigation Satellite Systems Reflectometry as a Remote Sensing Tool for Agriculture," *Remote Sensing*, **4**, 2012, pp. 2356-2372.

16. A. Egido et al., "Airborne GNSS-R Polarimetric Measurements for Soil Moisture and Above-Ground Biomass Estimation," *IEEE Journal of Selected Topics in Applied Earth Observation and Remote Sensing*, **7**, 5, May 2014, pp. 1522-1532.

17. M. Brogioni, A. Egido, N. Floury, R. Giusto, L. Guerriero, and N. Pierdicca, "A Simulator Prototype of Delay-Doppler Maps for GNSS Reflections from Bare and Vegetated Soils," Proc. IEEE Int. Geoscience and Remote Sensing Symposium, July 2010, pp. 3809-3812.

18. Y. Jia and P. Savi, "Sensing Soil Moisture and Vegetation Using GNSS-R Polarimetric Measurement," *Advances in Space Research*, **59**, 3, February 2017, pp. 858-869.

19. N. Sanchez, A. Alonso-Arroyo, J. Martinez-Fernandez, M. Piles, A. Gonzalez-Zamora, A. Camps, and M. Vall-llosera, "On the Synergy of Airborne GNSSR and Landsat 8 for Soil Moisture Estimation," *Remote Sensing*, **7**, 2015, pp. 9954-9974.

20. E. Cardellach, F. Fabra, O. Nogués-Correig, S. Oliveras, S. Ribó, and A. Rius, "GNSS-R Ground-Based and Airborne Campaigns for Ocean, Land, Ice, and Snow Techniques: Application to the GOLD-RTR Data Sets," *Radio Science*, **46**, 6, December 2011, pp. 1-16.

21. E. Motte, M. Zribi, P. Fanise, A. Egido, J. Darrozes,A. Al-Yaari, N. Baghdadi, F. Baup, S. Dayau, R. Fieuzal, P. L. Frison, "GLORI: A GNSS-R Dual Polarization Airborne Instrument for Land Surface Monitoring," *Sensors*, **16**, 5, May 2016, p. 732-753.

22. M. Zribi, F. Motte, N. Baghdadi, F. Baup, S. Dayau, P. Fanise, D. Guyon, M. Huc, J. Wigneron, "Potential Applications of GNSS-R Observations Over Agricultural Areas: Results from the GLORI Airborne Campaign," *Remote Sensing*, **10**, 8, August 2018, pp. 1245-1262.

23. M. Unwin, P. Jales, J. Tye, C. Gommenginger, G. Foti, and J. Rosello, "Spaceborne GNSS-Reflectometry on TechDemoSat-1: Early Mission Operations and Exploitation," *IEEE Journal Selected Topics on Applied Earth Observation and Remote Sensing*, **9**, 10, September 2016, pp. 4525-4539.

24. G. Foti, C. P. Gommenginger, P. Jales, M. Unwin, A. G. Shaw, Y. C. Robertson, and J. Rosello, "Spaceborne GNSS-Reflectometry for Ocean Winds: First Results from the UK TechDemoSat-1 Mission," *Geophysical Research Letters*, **42**, July 2015, pp. 5435-5441.

25. G. Foti, C. Gommenginger, M. Unwin, P. Jales, L. Tye, and J. Roselló, "An Assessment of Non-Geophysical Effects in Spaceborne GNSS Reflectometry Data from the UK TechDemoSat-1 Mission," *IEEE Journal of Selected Topics in Applied Earth Observations and Remote Sensing*, **10**, 7, July 2017, pp. 3418-3429.

26. A. Camps, M. Vall·llossera, H. Park, G. Portal, and L. Rossato, "Sensitivity of TDS-1 GNSS-R Reflectivity to Soil Moisture: Global and Regional Differences and Impact of Different Spatial Scales," *Remote Sensing*, **10**, 11, November 2018, pp. 1856-1875.

27. N. Pierdicca, A. Mollfulleda, F. Costantini, L. Guerriero, L. Dente, S. Paloscia, E. Santi, and M. Zribi, "Spaceborne GNSS Reflectometry Data for Land Applications: An Analysis of Techdemosat Data," Proceedings of the IEEE International Geoscience and Remote Sensing Symposium, July 2018, pp. 3343-3346.

28. C. Chew, R. Shah, C. Zuffada, G. Hajj, D. Masters, and A. J. Mannucci, "Demonstrating Soil Moisture Remote Sensing with Observations from the UK TechDemoSat-1 Satellite Mission," *Geophysical Research Letters*, **43,** 7, April 2016, pp. 3317-3324.

29. A. Camps, H. Park, I. Sekulic, J. Rius, "GNSS-R Altimetry Performance Analysis for the GEROS Experiment on Board the International Space Station," *Sensors*, **17**, 7, July 2017, pp. 1583-1601.

30. J. Wickert, et al., "GEROS-ISS: GNSS Reflectometry, Radio Occultation, and Scatterometry Onboard the International Space Station," *IEEE Journal of selected Topics in Applied Earth Observations and Remote Sensing,* **9**, 10, October 2016, pp. 4552-4581.

31. C. S. Ruf, C. Chew, T. Lang, M. G. Morris, K. Nave, A. Ridley, and R. Balasubramaniam, "A New Paradigm in Earth Environmental Monitoring with the CYGNSS Small Satellite Constellation," *Scientific Report*, **8**, 1, June 2018, pp. 8782-8788.

32. M. M. Al-Khaldi, J. Johnson, A. J. O'Brien, A. Balenzano, and F. Mattia, "Time-Series Retrieval of Soil Moisture Using CYGNSS," *IEEE Transactions on Geoscience and Remote Sensing*, **57**, 7, July 2019, pp. 4322-4331.

33. M. P. Clarizia and C. S. Ruf, "Wind Speed Retrieval Algorithm for the Cyclone Global Navigation Satellite System (CYGNSS) Mission," *IEEE Transaction Geoscience Remote Sensing*, **54**, 8, August 2016, pp. 4419-4432.

34. C. C. Chew and E. E. Small, "Soil Moisture Sensing Using Spaceborne GNSS Reflections: Comparison of CYGNSS Reflectivity to SMAP Soil Moisture," *Geophysical Research Letter*, **45**, 9, April 2018, pp. 4049-4057.

35. H. Carreno-Luengo, G. Luzi, and M. Crosetto, "First Evaluation of Topography on GNSS-R: An Empirical Study Based on a Digital Elevation Model," *Remote Sensing*, **11**, 21, January 2019, pp. 2556.

36. D. Comite, F. Ticconi, L. Dente, L. Guerriero, and N. Pieridcca "Bistatic Coherent Scattering from Rough Soils with Application to GNSS Reflectometry," *IEEE Transactions on Geoscience and Remote Sensing*, **58**, 1, January 2019, pp. 612-625.

37. L. Dente, L. Guerriero, D. Comite, and N. Pierdicca, "Space-Borne GNSS-R Signal Over a Complex Topography: Modelling and Validation," *Journal of Selected Topics in Applied Earth Observations and Remote Sensing*, **13**, 2020, pp. 1218-1233.

38. M. P. Clarizia and C. S. Ruf, "On the Spatial Resolution of GNSS Reflectometry," *IEEE Geoscience and Remote Sensing Letters*, **13**, 8, June 2016, pp. 1064-1068.

39. A. Camps, "Spatial Resolution in GNSS-R Under Coherent Scattering," IEEE *Geoscience Remote Sensing Letter*, **17**, 1, January 2020, pp 32-36.

40. P. Ferrazzoli, L. Guerriero, N. Pierdicca, and R. Rahmoune, "Forest Biomass Monitoring with GNSS-R: Theoretical Simulations," *Advances in Space Research*, **47**, 10, May 2011, pp.1823-1832.

41. H. Park, A. Camps, D. Pascual, Y. Kang, and R. Onrubia, J. Querol, and A. Alonso-Arroyo, "A generic Level 1 Simulator for Spaceborne GNSS-R Missions and Application to GEROS-ISS Ocean Reflectometry," *IEEE Journal of Selected Topics in Applied Earth Observation and Remote Sensing*, **10**, 10, July 2017, pp. 4645-4659.

42. H. Park, A. Camps, D. Pascual, A. Alonso-Arroyo, J. Querol, and R. Onrubia, "Improvement of PAU/PARIS End-to-End Performance Simulator (P2EPS): Land Scattering Including Topography," Proceedings of the IEEE International Geoscience and Remote Sensing Symposium, July 2016, pp. 5607-5610.

43. X. Wu and S. Jin, "GNSS-Reflectometry: Forest Canopies Polarization Scattering Properties and Modeling," *Advances in Space Research*, **54**, 5, September, 2014, pp. 863-870.

44. F. Fabra, E. Cardellach, W. Li, and A. Rius, "WAVPY: A GNSS-R Open Source Software Library for Data Analysis and Simulation," Proceedings of the IEEE International Geoscience and Remote Sensing Symposium, July 2017, pp. 4125-4128.

45. O. Eroglu, M. Kurum, and J. Ball, "Response of GNSS-R on Dynamic Vegetated Terrain Conditions," *IEEE Journal of Selected Topics in Applied Earth Observations and Remote Sensing*, **12**, 5, May 2019, pp. 1599-1611.

46. M. Kurum, M. Deshpande, A. T. Joseph, P. E. O'Neill, R. H. Lang, and O. Eroglu, "SCoBi-Veg: A Generalized Bistatic Scattering Model of Reflectometry from Vegetation for Signals of Opportunity Applications," *IEEE Transactions on Geoscience and Remote Sensing*, **57**, 2, September 2018, pp. 1049-1068.

47. A. K. Fung and H. J. Eom, "Coherent Scattering of a Spherical Wave from an Irregular Surface," *IEEE Transactions on Antennas Propag*ation, **31**, 1, January 1983, pp. 68-72.

48. W. Gu, H. Xu, and L. Tsang, "A Numerical Kirchhoff Simulator for GNSS-R Land Applications," *Progress In Electromagnetics Research*, **33**, 2019, pp. 164-119.

49. J. Zhu, L. Tsang, and H. Xu, "A Physical Patch Model for GNSS-R Land Applications," *Progress In Electromagnetics Research*, **165**, 2019, pp. 93-105.

50. R. D. De Roo and F. T. Ulaby, "Bistatic Specular Scattering from Rough Dielectric Surfaces," *IEEE Transactions on Antennas and Propagation*, **42**, 2, February 1994, pp. 220-231.

51. F. T. Ulaby, C. T. Allen, and A. K. Fung, "Method for Retrieving the True Backscattering Coefficient from Measurements with a Real Antenna," *IEEE Transactions on Geoscience and Remote Sensing*, **GE-21**, 3, July 1983, pp. 308-313.

52. H. A. Zebker and J. Villasenor, "Decorrelation in Interferometric Radar Echoes," *IEEE Transactions on Geoscience and Remote Sensing*, **30**, 5, September 1992, pp. 950-959.

53. G. Franceschetti, et al., "The Effect of Surface Scattering on IFSAR Baseline Decorrelation," *Journal of Electromagnetic Waves and Applications*, **11**, 3, 1997, pp. 353-370.

54. A. M. Balakhder, M. M. Al-Khaldi, and J. T. Johnson, "On the Coherency of Ocean and Land Surface Specular Scattering for GNSS-R and Signals of Opportunity Systems," *IEEE Transactions on Geoscience and Remote Sensing*, **57**, 12, September 2019, pp. 10426-10436.

55. D. Comite, L. Dente, L. Guerriero, and N. Pierdicca, "Modeling the Coherence of Scattered Signals of Opportunity," Proceedings of the IEEE International Geoscience and Remote Sensing Symposium, 2019, pp. 4819-4822.

Perturbing the High-Latitude Upper Ionosphere (F Region) with Powerful HF Radio Waves: A 25-Year Collaboration with EISCAT

N. F. Blagoveshchenskaya

Arctic and Antarctic Research Institute
38, Bering str.
St. Petersburg, 199397, Russia
E-mail: nataly@aari.nw.ru

Abstract

We present a brief review of experimental investigations concerning the perturbation of the high-latitude upper ionosphere (F region) by powerful HF radio waves (pump waves), carried out by the team from the Arctic and Antarctic Research Institute (AARI) during a 25-year collaboration with the European Incoherent Scatter (EISCAT) Scientific Association. Three types of HF pumping experiments were carried out by the Russian team at EISCAT. The first type of experiments was related to the modification of the ionosphere-magnetosphere coupling by HF pumping into the nightside ionosphere auroral E and F regions. The second type of experiments was concerned with investigations of geophysical phenomena by using the EISCAT HF heating facility and multi-instrument diagnostics. Most of the experiments were closely related to radio science and nonlinear plasma experiments (a third type of experiment). The main attention was paid to the investigation of artificial ionospheric turbulence in the upper ionosphere (F region) induced by the extraordinary (X-mode) HF pump waves. A great number of X-mode experiments, carried out by the Russian team at EISCAT, clearly demonstrated for the first time that an X-polarized HF pump wave was able to produce various HF-induced phenomena in the high-latitude ionospheric F region, which could be even much stronger than the O-mode effects. We found for the first time that the powerful X-mode HF radio waves, injected into the high-latitude ionospheric F2 layer towards the magnetic zenith, were capable of generating artificial field-aligned irregularities, radio-induced optical emissions in the red (630 nm) and green (557.7 nm) lines, strong electron acceleration leading to N_e enhancements, ion-acoustic and Langmuir electrostatic waves, and spectral components in the narrowband stimulated electromagnetic emission observed at a large distance from the HF heater. The features and behavior of the X-mode effects were analyzed and compared with the O-mode effects.

1. Introduction

The space environment forms a natural plasma laboratory for the investigation of various physical processes occurring in a plasma. In addition to naturally occurring phenomena, physical phenomena can be artificially excited by the injection of powerful radio waves (pump waves) into the ionosphere. Ionospheric-modification experiments by the use of ground-based high-frequency (HF) transmitters with high effective radiated power – so-called HF heating facilities – provide controlled detailed studies and understanding of various plasma processes in the ionosphere and magnetosphere. Such investigations are important for radio science, space weather, laser fusion, etc.

During 25 years, the team from the Arctic and Antarctic Research Institute (AARI), headed by me, collaborated with the EISCAT (European Incoherent Scatter) scientific association in conducting ionospheric modification experiments at Tromsø, with the use of the HF heating facility and the UHF incoherent-scatter radar (933 MHz). The largest number of experiments was carried out from 2008 to 2016 in the framework of the agreement between the EISCAT Scientific Association and AARI.

Three types of HF pumping experiments were carried out by the Russian team at EISCAT. The first type of experiment was related to the modification of the ionosphere-magnetosphere coupling by HF pumping into the nightside ionosphere auroral E and F regions towards the magnetic zenith (along the local geomagnetic field line) or near the magnetic field-aligned direction. The main attention here was paid to the search for distinctive features related to the modification of the ionosphere-magnetosphere coupling. We found evidence that HF pump waves injected into an auroral sporadic E layer were able to modify the natural auroral arc and to induce a local spiral-like formation [1-5]. Experimental results from multi-instrument observations

demonstrated that HF pumping into auroral E and F regions can lead to triggering of local auroral activation [1, 3, 5].

The intriguing evidence of the magnetospheric response to HF heater turn on and turn off was found from magnetic pulsation observations over a frequency range up to 5 Hz (the upper frequency limit of the sensitive magnetometer at Kilpisjarvi, located near Tromsø) [2]. The response manifested itself as spikes (main and echoing) in the dynamic frequency spectra. The main spikes were delayed in time by approximately 1 min after the HF heater turning on and off, and could be attributed to HF-induced Alfvén-wave pulses and their echoes seen in pulsation magnetometer data [2]. The ionospheric response to the HF heater turn on and off was presented in [6].

HF pumping into the F region is able to generate HF-induced ion upflows from the ionosphere, which were most pronounced in evening and night hours and were observed both under quiet [7, 8] and disturbed [2, 5] magnetic conditions. Different mechanisms responsible for the generation of ion upflows could be operating under quiet and disturbed background conditions.

The second type of experiments concerned investigations of geophysical phenomena by using the EISCAT HF heating facility and multi-instrument diagnostics [9-12]. The features of the magnetic pulsations in the *Pc*4-5 ranges were investigated in detail [10, 11]. An analysis of the experimental data obtained and numerical calculations demonstrated that depending on the level of the EISCAT/Heating facility power the observed wave activity in the *Pc*4 range was most probably induced by the intensification of natural stable *Pc*4 pulsations and by the generation of an Alfvén wave in a modified ionosphere [11].

We also showed that the combination of an HF-induced target and bistatic HF Doppler radio-scatter observations was a profitable method for probing medium-scale traveling ionospheric disturbances (TIDs) at high and mid-latitudes. HF ionospheric modification experiments provided a way of producing the HF-induced scatter target in a controlled manner at altitudes where the sensitivity to the TIDs was highest [12].

Most of the experiments carried out by the Russian team at Tromsø were closely related to the radio science and non-linear plasma experiments (the third type of experiment). As a general rule, HF pump waves with the ordinary polarization (O-mode) were used for the modification of the ionospheric F region. The ordinary-polarized HF pump waves interacted with the ionospheric plasma most efficiently at the reflection and upper-hybrid resonance altitudes. Nonlinear interaction between O-mode pump waves and the F-region ionospheric plasma produced a large number of phenomena that were successfully studied at all HF heating facilities in the world: see, for example, reviews [13-15] and references therein. The O-mode experiments, carried out by the Russian team, were focused to make up for some gaps in studies and understanding of HF-induced phenomena.

We found for the first time that the O-mode HF pump wave was capable of exciting the stimulated electromagnetic emission (SEE) near the second harmonic of the pump frequency [16]. The results obtained gave new and important information on the stimulated electromagnetic emission processes occurring in the downshifted maximum (DM) range of frequencies, and may guide us in the interpretation of these processes. This is a process that is very similar to that observed in the radio emission from the solar corona.

From multi-instrument observations in the course of an O-mode pumping experiment it was demonstrated that excitation of small-scale artificial field-aligned irregularities (AFAIs) is possible in the nightside auroral ionosphere [17].

The HF long-distance diagnostic tools located in St. Petersburg combined with multi-instrument observations at Tromsø were operated in conjunction with the ionospheric heating facility near Tromsø to examine the heater-induced phenomena in the auroral ionosphere during a magnetospheric substorm [18]. The procedure of ray-tracing simulation of the diagnostic HF signals scattered from artificial field-aligned irregularities was described in [19].

The aspect-angle dependence of O-mode HF pump-induced phenomena were analyzed from multi-instrument observations in the course of EISCAT heating experiments under quiet magnetic conditions. Experimental results revealed that the strongest electron temperature enhancements, optical emissions, and artificial field-aligned irregularities occurred when HF pumping was produced in the magnetic field-aligned pointing (magnetic zenith) direction [5, 7]. It was suggested that self-focusing of the HF pump wave on artificial field-aligned irregularities was a candidate mechanism for the magnetic zenith effect.

The properties of various HF-induced phenomena, such as artificial field-aligned irregularities, stimulated electromagnetic emission, optical emissions, Langmuir and ion-acoustic turbulence, strongly depend on the proximity of the pump frequency to the electron gyro-harmonic frequency (nf_{ce} , where n is the number of the harmonic and f_{ce} is an electron gyro-frequency). Features and behaviors of artificial field-aligned irregularities, stimulated electromagnetic emission, electron temperature and density, Langmuir and ion-acoustic plasma waves, seen from the incoherent-scatter radar as HF-induced plasma and ion lines, were analyzed in the course of pump-wave frequency stepping within 200 kHz of the nf_{ce} . Such investigations were made for third [20, 21], fourth [22], fifth, and sixth [23] electron gyro-harmonics. Distinctive features, possible generation mechanisms, and conditions of appearance of outshifted plasma lines were considered in [24].

In contrast to the O-mode HF pump wave, a powerful extraordinary (X-mode) HF radio wave did not match the

resonance altitudes because its reflection height was below the upper hybrid (UH) resonance altitude and the reflection altitude of the O-polarized pump wave. An X-mode HF pump wave should therefore not excite the thermal parametric (resonance) instability (TPI) responsible for the artificial field-aligned irregularity generation as well as the parametric decay instability (PDI), when it decays into electrostatic plasma waves such as a Langmuir wave (LW) and ion-acoustic wave (IAW). In addition, the electric field of the X-mode pump wave at the reflection altitude was perpendicular to the geomagnetic field, but the parametric decay instability excitation required a parallel electric field that was realized for the O-mode pump wave. However, a great number of X-mode experiments, carried out by the Russian team at EISCAT, clearly demonstrated for the first time that an X-polarized HF pump wave was able to produce various HF-induced phenomena in the high-latitude ionospheric F region that can be even much stronger than O-mode effects.

This review describes the various phenomena in the high-latitude ionospheric F region induced by X-mode HF pump waves and their comparison with the O-mode effects. Descriptions of the ionospheric modification experiments and diagnostic instruments are given in Section 2. Experimental results related to the distinctive features, behaviors, and possible generation mechanisms of small-scale artificial field-aligned irregularities (AFAIs), changes of plasma parameters (electron temperature and density, T_e and N_e), HF-induced optical emissions, Langmuir and ion-acoustic turbulence, and narrowband stimulated electromagnetic emission within ± 1 kHz of the heater frequency are presented in Sections 3, 4, 5, 6, and 7, respectively. The results come from a large number of experiments carried out in day and evening hours under quiet magnetic conditions at different pump frequencies ($f_H = 4$ MHz to 8 MHz), lying below and above the critical frequency of the F2 layer. Concluding remarks and my thoughts concerning the future investigations of the X-mode effects are given in Section 8.

2. Description of Experiments and Diagnostic Instruments

Modification of the high-latitude ionospheric F region was produced by the EISCAT/heating facility near Tromsø in northern Norway (69.6°N, 19.2°E, magnetic dip angle $I = 77°$) [25]. HF pumping was produced by powerful X-mode polarized HF radio waves at frequencies below and above the critical frequency of the F2 layer ($f_H \le f_0F2$ and $f_H > f_0F2$). Alternating O-mode and X-mode HF pumping experiments were carried out under $f_H \le f_0F2$, when the O-mode and X-mode effects were possible. At low pump frequencies, in the range of 4 MHz to 5.5 MHz, phased array 2, with a beamwidth of 12° to 14° (at -3 dB level) and 22 dBi to 25 dBi gain was utilized. During the experiments, the effective radiated power (ERP) was 110 MW to 220 MW. At pump frequencies of 5.5 MHz to

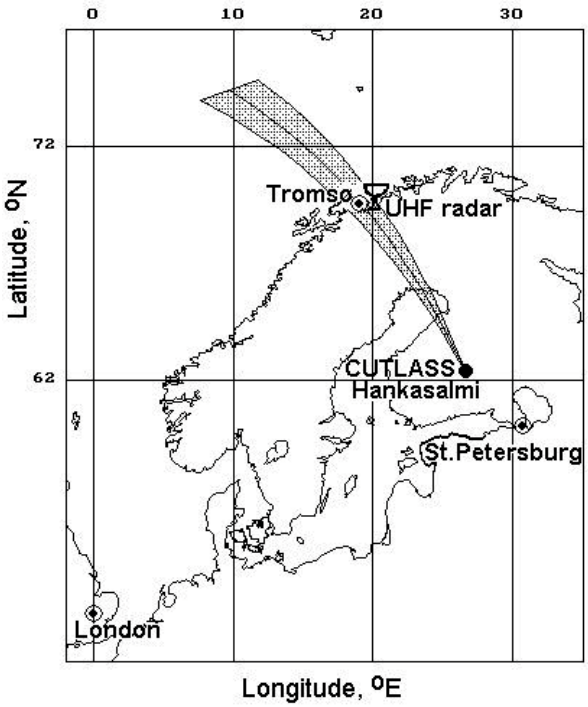

Figure 1. A map showing the location of the EISCAT/heating facility, the EISCAT UHF incoherent-scatter radar, and the viewing geometry of the CUTLASS Hankasalmi (Finland) HF coherent scatter radar.

8 MHz, mostly phased array 1, having a narrow beamwidth of 5° to 6° and resulting in 28 dBi to 31 dBi gain, was used. In the course of experiments, the ERP was varied from 460 MW to 800 MW. Some experiments at frequencies of 5.5 MHz to 8 MHz were conducted by using phased array 3, with a wide beamwidth of 10° to 12° and 22 dBi to 25 dBi gain. In these experiments, the ERP was 130 MW to 240 MW. The HF heater beam was directed towards the magnetic zenith (12° south of vertical). However, for the investigation of the aspect-angle dependence, some experiments were carried out at three positions of the HF beam, such as 90° (vertical), 84°, and 78° (magnetic zenith). The transmission scheme of 10 min continuous wave (CW) on, 5 min off and 5 min on, 2.5 min off was most often used.

Multi-instrument diagnostics were used for the investigation of the X-mode HF-induced phenomena. The EISCAT UHF incoherent-scatter radar at 933 MHz [26], spatially collocated with the HF heating facility at Tromsø, was applied in the evaluation the ionospheric plasma parameters and HF-enhanced ion and plasma lines (HFILs and HFPLs) from the backscattered radar spectra. Artificial field-aligned irregularities were recognized from the backscattered signals received at Hankasalmi, Finland (62.3°N; 26.6°E) by the CUTLASS (Co-operative UK Twin Located Auroral Sounding System) HF coherent radar [27]. Observations were performed in a nonstandard mode, almost simultaneously at three frequencies from 10 MHz to 20 MHz, which allowed diagnostics of artificial field-aligned irregularities with spatial scales perpendicular to the magnetic field of 7.5 m to 15 m. HF-induced optical

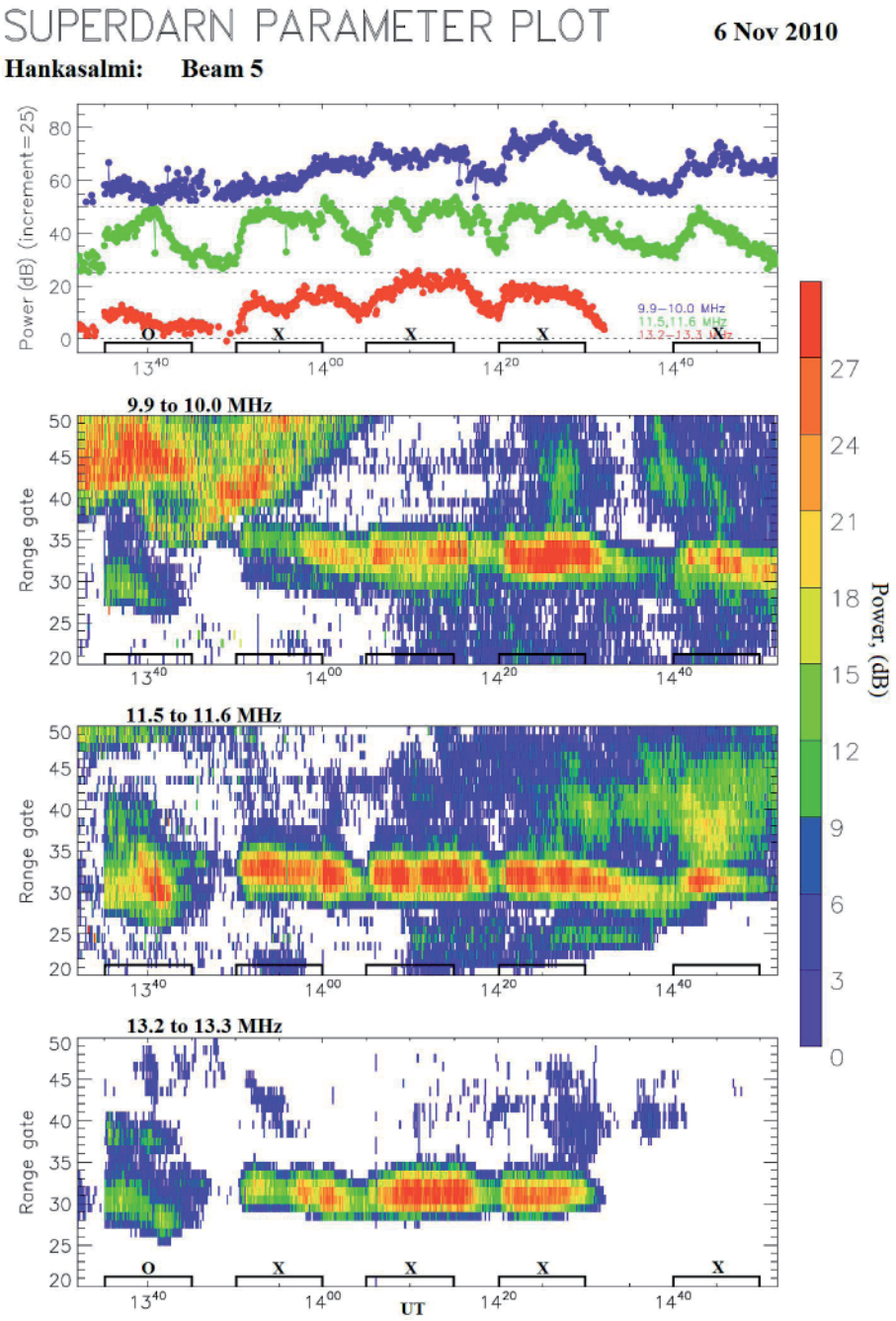

Figure 2. The backscattered power from the Hankasalmi (Finland) CUTLASS radar (beam 5) at operational frequencies of about 10 MHz, 11.5 MHz, and 13 MHz during the experiment on 6 November 2010 from 13:32 to 15:00 UT. The behavior of the backscattered power averaged between 30 to 34 gates, corresponding to the central part of the heated patch, is shown in the top panel and its behavior in the range-gate – universal-time UT coordinates is given in the bottom panels. The HF pump wave was radiated at a frequency of 4.544 MHz towards the magnetic zenith. The effective radiated power was about 180 MW. O/X-mode heater-on cycles are marked on the time axis (adapted from Blagoveshchenskaya et al. [33]).

emissions (artificial aurora) at red (630 nm) and green (557.7 nm) lines were observed at the Tromsø site by the Digital All-Sky Imager 2 (DASI-2) and from remote sites by the Auroral Large Imaging System (ALIS) [28] in Sweden. The observations of narrowband stimulated electromagnetic emission (NSEE) were conducted within ±1 kHz of the pump frequency in the vicinity of St. Petersburg (60°N, 30°E) at a distance from Tromsø of about 1200 km. Multi-channel HF Doppler equipment [29] near St. Petersburg and a net of oblique ionospheric sounders [30] were used for bi-static scatter observations of artificial field-aligned irregularities. The double-rhombic HF antenna system oriented to Tromsø was utilized in all measurements near St. Petersburg in the course of HF pumping experiments

for the narrowband stimulated electromagnetic emission (NSEE) observations. HF receivers for wideband stimulated electromagnetic emission (WSEE) measurements in the frequency band of 200 kHz were also employed at Tromsø. The status of the ionosphere in the course of experiments was checked by HF vertical sounders (Dynasonde and Digisonde) and magnetometers. The geometry of the experiments is shown in Figure 1.

3. Small-Scale Artificial Field-Aligned Irregularities (AFAIs)

Ionospheric modification experiments are providing the means for understanding mechanisms and physical processes leading to the generation and evolution of ionospheric irregularities. We present experimental results concentrating on the features and evolution, generation conditions and mechanisms of artificial field-aligned irregularities, with spatial scales across the geomagnetic field of 7.5 m to 15 m, in the high-latitude ionospheric F region induced by the controlled injection of the powerful HF radio waves from the ground into the ionosphere. The behavior and properties of artificial field-aligned irregularities excited by the O-mode HF pump waves are well known (see, for example, [13-15] and references therein). The main attention is paid to the recently discovered artificial field-aligned irregularities induced by the X-mode HF pump waves and their comparison with the O-mode artificial field-aligned irregularities [31-37].

A large number of experiments, carried out by the Russian team from 2010 to 2019 at EISCAT, clearly demonstrated that the X-mode HF pump wave was able to excite artificial field-aligned irregularities in the high-latitude ionospheric F region. In contrast to the O-mode, when artificial field-aligned irregularities were only generated under $f_H \le f_0F2$, the X-mode artificial field-aligned irregularities were excited in the course of HF pumping into the MZ at frequencies both below and above (up to 2 MHz) the critical frequency of the F2 layer ($f_H \le f_0F2$ and $f_H > f_0F2$) [21, 31, 33, 35, 37]. It is important to note that X-mode artificial field-aligned irregularities are generated in the regular *F* region under quiet conditions (no precipitation of particles, field-aligned currents, and electrojet).

Figure 2 presents the CUTLASS Hankasalmi backscatter power at three frequencies of ~10 MHz, 11.5 MHz, and 13 MHz, sensitive to artificial field-aligned

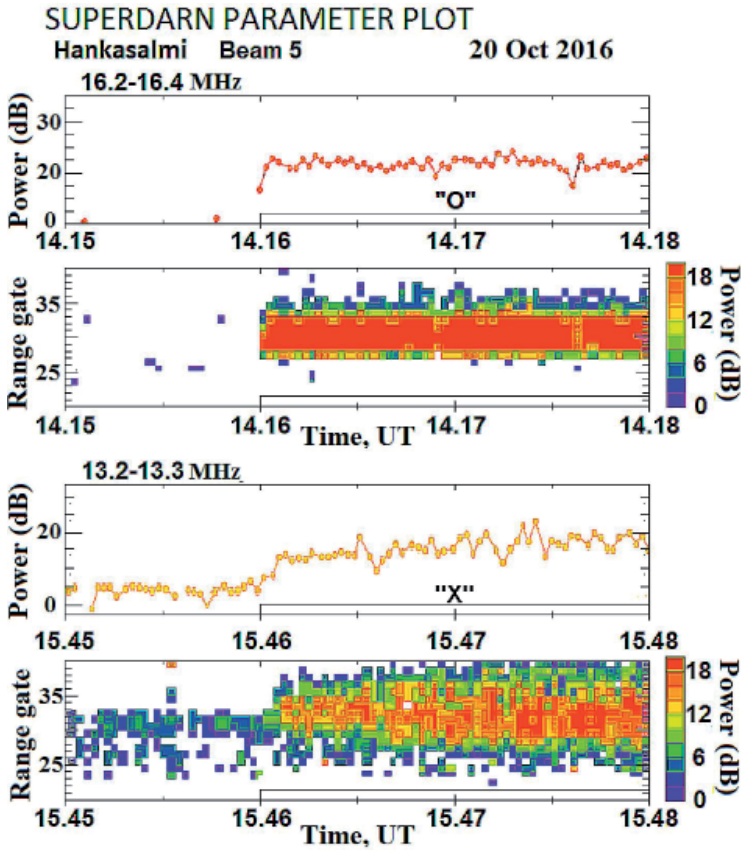

Figure 3. The backscattered power from the Hankasalmi (Finland) CUTLASS radar (beam 5) on 20 October 2016 for O-mode and X-mode heater pulses 1 min before the HF pumping onset and during the first 2 min of the heating cycles. The HF pump wave was radiated at a frequency of 4.544 MHz towards the magnetic zenith. The effective radiated power was about 130 MW. O/X-mode heater-on cycles are marked on the time axis (adapted from Blagoveshchenskaya et al. [32]).

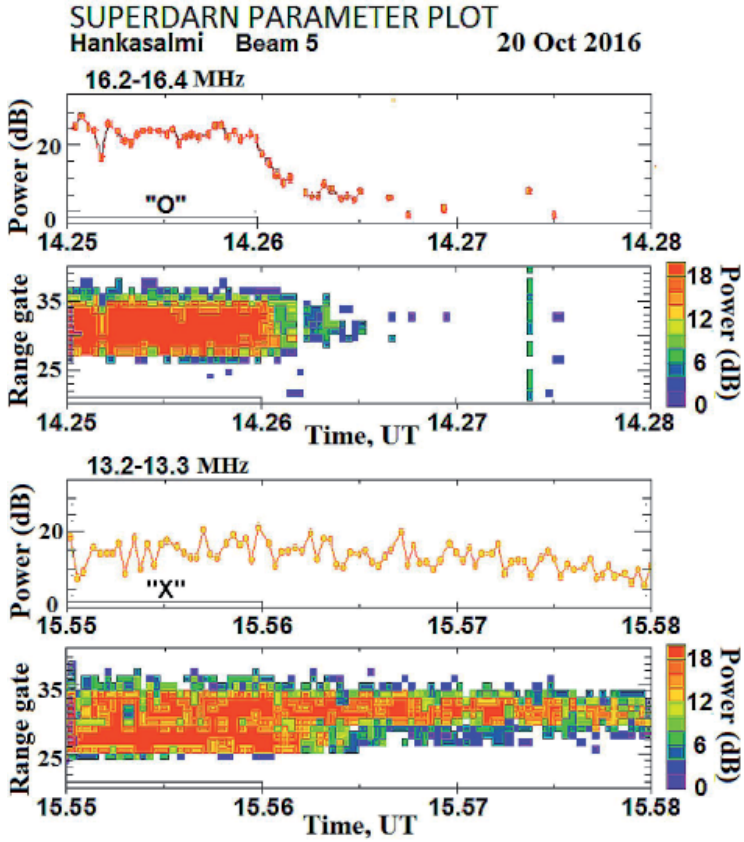

Figure 4. The backscattered power from the Hankasalmi (Finland) CUTLASS radar (beam 5) on 20 October 2016 for O-mode and X-mode heater pulses during the last minute of the heating cycles and the first 2 min after the HF heater was turned off. The HF pump wave was radiated at a frequency of 4.544 MHz towards the magnetic zenith. The effective radiated power was about 130 MW. The O/X-mode heater-on cycles are marked on the time axis (adapted from Blagoveshchenskaya et al. [32]).

irregularities with the spatial size across the geomagnetic field of the order of $l_\perp \approx 15$ m, 13 m, and 11 m, for a beam position centered on the Tromsø heater (beam 5) on 6 November 2010 [33]. HF pumping was produced towards the magnetic zenith at $f_H = 4.544$ MHz, which was above f_0F2.

The analysis of the entire volume of the CUTLASS data clearly demonstrated that the features and behaviors of the O-mode and X-mode artificial field-aligned irregularities radically differed. There was also a significant difference in the decay times for X-mode artificial field-aligned irregularities excited at high ($f_H = 5.5$ MHz to 8 MHz) and low ($f_H = 4$ MHz to 5.0 MHz) heater frequencies. The artificial field-aligned irregularity decay time at high pump frequencies did not exceed 3 min in the evening hours, whereas it can reach unusually long values exceeding the 5 min pause between the pump pulses at low heater frequencies.

Let us further compare the artificial field-aligned irregularity growth and decay times (t_1 and t_2) for O-mode and X-mode HF pumping. The CUTLASS backscatter powers, demonstrating the growth and decay times on 20 October 2016 ($f_H = 4.544$ MHz), are shown in Figures 3 and 4, respectively [37]. As seen, the artificial field-aligned irregularity growth and decay times significantly differed for O- and X-mode HF pumping. Upon the O-mode pumping, $t_1 = 6$ s to 9 s and $t_2 = 30$ s to 50 s. The growth and decay times for an X-mode pumping greatly depend on the preconditioning history. From a "cold" start (the first X-mode pulse), $t_1 \approx 60$ s to 70 s (it can even reach 150 s at $f_H > f_0F2$) and $t_2 \approx 100$ s to 130 s. In X-mode cycles with history, when the aftereffects of previous heating cycles act, t_1 decreased and t_2 increased [37].

It was found that the physical driving mechanisms of artificial field-aligned irregularities with a spatial scale across the geomagnetic field of 7.5 m to 15 m were significantly different for O-mode and X-mode HF pumping, presenting challenges for understanding the relevant processes. In contrast to the O-mode artificial field-aligned irregularities, excited by a thermal parametric (resonance) instability at the upper hybrid resonance altitude [13, 14],

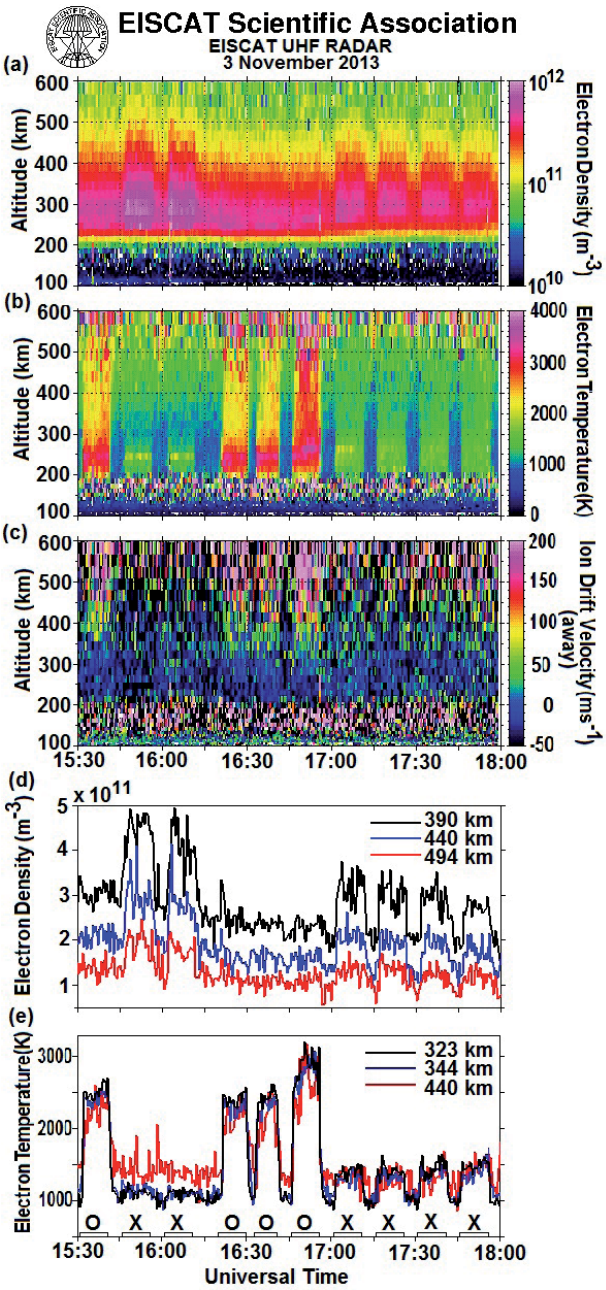

Figure 5. EISCAT UHF radar observations in the magnetic zenith (13°S) obtained with 30 s integration time during an HF modification experiment at Tromsø on 3 November 2013 from 15.30 to 18:00 UT. Altitude-temporal variations of the electron density (a), temperature (b), ion velocities (c), and variations in time at fixed altitudes of the electron density (d) and temperature (e) are shown. High-power HF radio waves with alternating O/X polarization were transmitted towards the magnetic zenith at a frequency of 6.2 MHz by pulses of 10 min on, 5 min off. The effective radiated power was about 450 MW. The heater pulses and polarization of the HF pump wave are drawn on the time axis of the bottom plot (adapted from Blagoveshchenskaya et al. [35]).

the X-mode artificial field-aligned irregularities were generated via a two-step process [31, 36-38]. In the first step, the generation of elongated large-scale irregularities (with a spatial scale across the geomagnetic field of the order of 1 km to 10 km) due to the self-focusing instability occurred. The excitation and behavior of small-scale artificial field-aligned irregularities was driven by large-scale irregularities. Their possible generation mechanisms could be the temperature-gradient-drift instability [38] or the filamentation instability [39].

4. Electron Density and Temperature Disturbances

We next consider the plasma parameter changes, such as the electron density and temperature (N_e and T_e), in the high-latitude ionospheric F2 layer induced by an X-mode HF pump wave. We compare them with the O-mode effects, depending on the ratio of f_H / f_0F2 .

Figure 5 depicts the altitude-temporal distribution of N_e , T_e , and ion velocities (V_i), as well as the N_e and T_e variations at fixed altitudes, from the EISCAT UHF radar observations on 3 November 2013 from 15:30 to 18:00 UT, when the critical frequencies f_0F2 gradually dropped from 6.7 MHz at 15:30 UT to 5.2 MHz at 18:00 UT [35]. In the course of the experiment, the HF pump wave radiated at $f_H = 6.2$ MHz towards the magnetic zenith with an effective radiated power of 450 MW. From 15:30 to 17:00 UT, when the pump frequency was below or near the critical frequency f_0F2 ($f_H / f_0F2 = 0.92 - 1.05$), alternating O/X pumping was carried out. From 17:00 UT, f_0F2 dropped to 5.8 MHz and excitation of the O-mode effects was made impossible because only X-mode HF pumping was performed.

As seen from Figure 5, large electron temperature increases, up to 2500 K to 3000 K (Figures 5b and 5e), accompanied by the generation of ion upflows from the ionosphere above ~350 km (Figure 5c), were observed under O-mode pumping. The electron-density changes were not significant. Such processes were a typical signature of the O-mode HF pumping, observed in previous EISCAT heating experiments [5, 7, 8, 40].

The opposite behavior (minor increases of electron temperature and large electron-density enhancements) was exhibited under X-mode HF pumping. Large electron-density increases of 50% to 70% were observed in a wide altitude range up to 600 km during all X-mode pump pulses (Figures 5a and 5d). Such N_e enhancements were a typical feature of X-mode pumping at different frequencies ($f_H = 4$ MHz to 8 MHz) but were most pronounced at high pump frequencies ($f_H = 6$ MHz to 8 MHz) from EISCAT UHF radar observations [31, 35, 36, 41]. These N_e enhancements occurred only in the magnetic field-aligned direction in a narrow-angle beam with a width of 3° to 4°around the magnetic field line [34, 35]. The N_e enhancements were accompanied by weak T_e increases (about 20% above the background values), when f_H was below the critical frequency ($f_H \le f_0F2$). However, the

T_e enhancements induced by ohmic heating increased up to 50% under $f_H > f_0F2$.

Strong N_e enhancements from EISCAT UHF radar measurements were common for X-mode pumping and were observed as often as the T_e enhancements under the action of O-polarized HF pump waves. They occurred along the magnetic field line in a wide altitude range whether or not the HF-enhanced ion and plasma lines were excited. The origin of large N_e enhancements, observed under X-mode HF pumping, is not yet understood, although one explanation involving ducting of the 933 MHz radar waves by field-aligned irregularities has recently been suggested [42]. However, we suggest that X-mode pumping towards the magnetic zenith initiates the acceleration of electrons, due to the fact that the electric field of a circularly polarized X-mode HF pump wave rotates in the same sense as the electron gyromotion. As was found in [43], the flux of accelerated electrons can produce an increased production of ionization. The presence of electron acceleration produced by the X-mode HF pumping towards the magnetic zenith is greatly confirmed by the optical observations. It was found that X-mode heating leads to a generation of very intense radio-induced optical emission in red and green lines with a high ratio of green to red line of 0.35 to 0.5 [34]. This experimental fact confirmed the presence of strong electron acceleration and therefore the enhanced electron density under X-mode pumping. One would expect that the duct of the enhanced electron density would guide the HF pump wave along the magnetic field line.

5. HF-Induced Optical Emission

We found from a set of repetitive experiments under quiet magnetic conditions that an X-polarized HF pump wave, radiated into the high-latitude ionospheric *F* region towards the magnetic zenith, can generate HF-induced optical emissions (HFOEs) at the red (630 nm) and green (557.7 nm) lines [34]. HF-induced optical emissions were generated at high pump frequencies ($f_H = 6.2$ MHz and 7.1 MHz), which were away from electron gyro-harmonics, under different ratios of the pump frequency f_H to f_0F2 ($f_H > f_0F2$, $f_H \approx f_0F2$, $f_H < f_0F2$). In the course of these experiments, the intensities of the red and green lines changed over a range of 110-950 R and 50-350 R, respectively. A comparison between the O- and X-mode HF-induced optical emissions clearly demonstrated the distinctions between them. The higher ratio of green to red line was typical for the X-mode HF-induced optical emissions. As shown in [34], the ratio of green to red lines for O-mode heating was $I_{577.7}/I_{630.0} = 0.22$ to 0.33, while under X-mode pumping this ratio reached the values of $I_{577.7}/I_{630.0} = 0.35$ to 0.5. Such high ratios of HF-induced optical emission intensities at green to red lines made it evident that strong electron acceleration was observed under X-mode pumping, which, in turn, can lead to the enhanced production of ionization along the magnetic field-aligned direction [43].

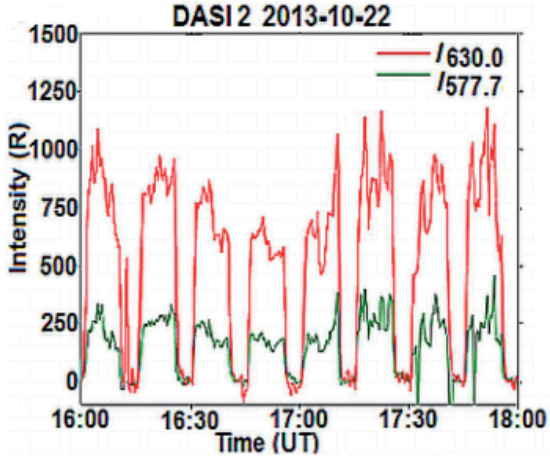

Figure 6. The intensity of the HF-induced optical emissions of the red (630.0 nm) and green (557.7 nm) lines imaged by the DASI-2 at the EISCAT site on 22 October 2013 from 16:00 to 18:00 UT. The X-mode pump wave was radiated at 7.1 MHz towards the magnetic zenith by 10 min on, 5 min off pulses beginning from 16:01 UT. In the course of the experiment, the effective radiated power varied between 458 MW to 548 MW (adapted from Blagoveshchenskaya et al. [34]).

Unusually intense X-mode emissions were excited on 22 October 2013, when they were simultaneously observed at the Tromsø site by DASI-2 and at the remote ALIS Abisko station. There the X-polarized continuous wave was radiated at 7.1 MHz using cycles of 10 min on, 5 min

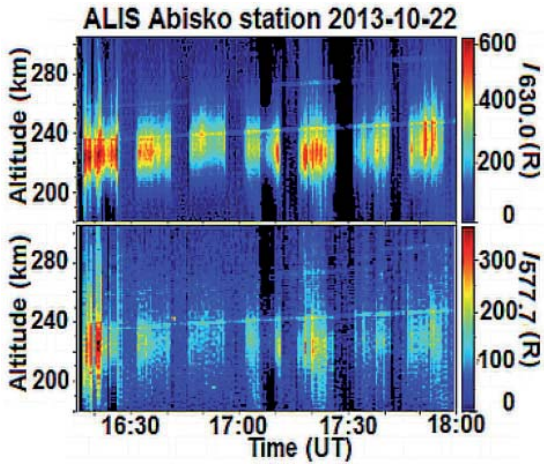

Figure 7. The altitude distribution of HF-induced optical emission intensities at red (630.0 nm) and green (557.7 nm) lines as a function of time (keogram) obtained at the ALIS Abisko station on 22 October 2013 from 16:00 to 18:00 UT. ALIS was looking at a volume above Tromsø and obtained one image every 10 s with an integration time of 6.5 s. The imager was running a filter sequence alternating between the emissions at 557.7 nm, 630.0 nm, and 844.6 nm. The X-mode pump wave was radiated at 7.1 MHz along the magnetic field by 10 min on, 5 min off pulses beginning from 16:01 UT. The effective radiated power varied between 458 MW to 548 MW (adapted from Blagoveshchenskaya et al. [34]).

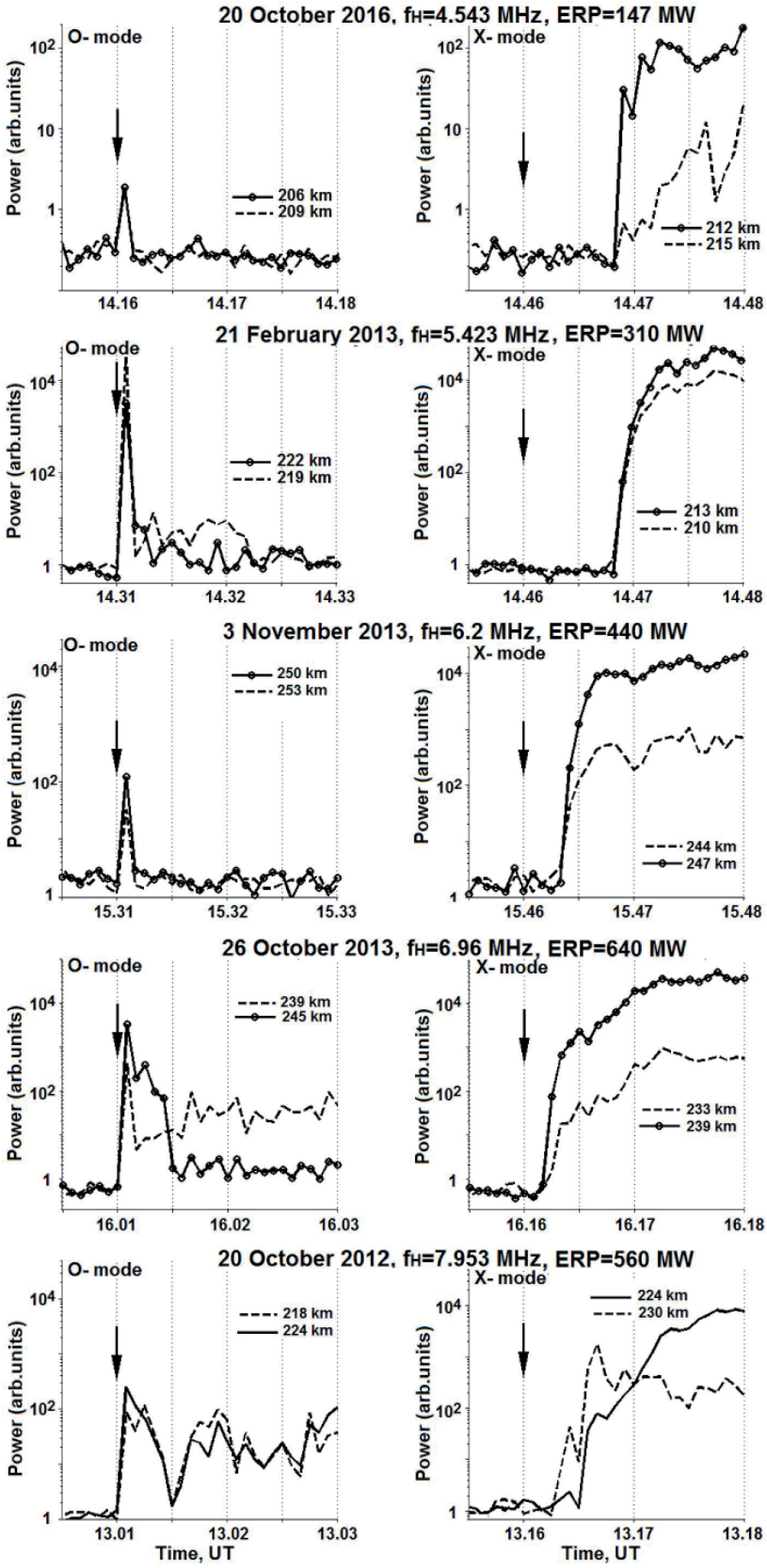

Figure 8. The temporal evolution of the power of HF-enhanced down-shifted plasma lines (HFPLs) with a 5 s resolution under O-mode and X-mode HF pumping at frequencies of 4.544 MHz, 5.423 MHz, 6.2 MHz, 6.96 MHz, and 7.953 MHz, 30 s before the HF pumping onset and during the first 2 min of the heating cycles. The HF-enhanced plasma line powers are shown at two fixed heights where they had maximum values (adapted from Blagoveshchenskaya et al. [36]).

off. The optical observations are shown in Figures 6 and 7 [34]. The intensity of HF-induced optical emissions of the red and green lines, taken by DASI-2 at the Tromsø site, is demonstrated in Figure 6. Strong artificial red and green line emissions, up to about 1000 R and 380 R above the background, respectively, were observed in every X-mode heater pulse from 16:00 to 18:00 UT. The DASI-2 camera was not able to determine the altitude structure of HF-induced optical emissions, but the ALIS camera at Abisco could do that. The altitude distribution of red and green line intensities as a function of time (keogram), taken from the ALIS Abisko station, is shown in Figure 7. As seen from Figure 7, the most intense radio-induced optical emissions were recorded in the altitude range of 215 km to 240 km. It is important that in the same altitude range the most intense HF-induced ion and plasma lines were excited in the EISCAT UHF radar measurements [34].

The distinctive feature of X-mode artificial optical emissions was their coexistence with the intense HF-enhanced ion and plasma lines, artificial field-aligned irregularities, and enhanced electron density in the magnetic field-aligned direction through the whole heater pulse. The O-mode HF-induced optical emission was accompanied by strong thermal electron heating and generation of ion upflows from the ionosphere [34].

6. Langmuir and Ion-Acoustic Turbulence

Incoherent-scatter radar collocated with the HF heater is capable of providing investigations of Langmuir (L) and ion-acoustic (IA) plasma waves. They are directly evidenced from radar spectra as HF-enhanced plasma (HFPL) and ion (HFIL) lines [44, 45].

We analyzed the distinctive features and behaviors of HF-enhanced Langmuir and ion-acoustic turbulences induced by the O-mode and X-mode HF pump waves radiated into the high-latitude ionospheric F region towards the magnetic zenith [36, 41, 46, 47]. Results came from a large number of alternating O/X-mode experiments carried out at the pump frequencies of f_H = 5.423 MHz; 6.2 MHz; 6.96 MHz; 7.1 MHz; 7.953 MHz with an ERP = 450 MW to 650 MW under quiet magnetic conditions. Note that X-mode HF-enhanced plasma lines and HF-enhanced ion lines were excited at pump frequencies both below and above f_0F2 ($f_H \le f_0F2$ and $f_H > f_0F2$). In the case $f_H > f_0F2$, HF-induced plasma and ion lines were generated in the frequency range between f_0F2 and f_xF2, where f_xF2 is the critical frequency of the extraordinary component of the $F2$ layer ($f_xF2 = f_0F2 + f_{ce}/2$, where f_{ce} is the electron gyro-frequency) [35].

An essential difference in the temporal evolution of HF-enhanced plasma lines and HF-enhanced ion lines excited by O-mode and X-mode HF pump waves at frequencies $f_H \le f_0F2$ was found. Figure 8 demonstrates the temporal evolution of the maximum power of the HF-enhanced downshifted plasma line (HFPL) with a 5 s resolution under O-heating and X-heating at frequencies of 4.544 MHz, 5.423 MHz, 6.2 MHz, 6.96 MHz, and 7.953 MHz, 30 s before the HF pumping onset and during the first 2 min of the heating cycles [36]. The HF-enhanced plasma line powers are shown at two fixed heights where they had maximum values. The same behavior was also observed for HF-enhanced ion lines [41].

The O-mode pump onset was accompanied by the immediate increase of the plasma and ion line intensities observed in the first few 5 s dumps. That was a classic manifestation of the resonance parametric decay instability (PDI), when the powerful electromagnetic wave (pump wave) decays into Langmuir and ion acoustic plasma waves. Thereafter, the completely developed artificial field-aligned irregularities prevent any further parametric decay instability excitation. However, under high effective radiated power (ERP > 250 MW to 300 MW), preferably at high pump frequencies (f_H = 7 MHz to 8 MHz), the reappearance of HF-enhanced plasma lines and HF-enhanced ion lines can occur after the initial overshoot. They coexisted with artificial field-aligned irregularities, gradually enhanced, similar to the X-mode effects, but their intensity was much lower as compared to the intensity of the X-mode Langmuir and ion-acoustic waves (see Figure 8).

The appearance of the X-mode Langmuir and ion-acoustic plasma waves was delayed by 15 s to 30 s from the heating onset. Their intensity then smoothly enhanced and maximized within about 1 min, when artificial field-aligned irregularities were generated [41]. Such a behavior of HF-induced plasma and ion turbulence corresponded to the development of the non-resonance type instability in which artificial field-aligned irregularities played a key role. Coexisting HF-enhanced plasma and ion lines and artificial field-aligned irregularities during the whole pump pulse was a typical feature of X-mode experiments. It was also found that intense HF-enhanced plasma lines and HF-enhanced ion lines coexisted with the HF-induced optical emissions at red and green lines with high ratio of green to red lines [34].

It was shown that excitation thresholds for the parametric decay instability (PDI), represented in the radar spectra as HF-enhanced plasma and ion lines, significantly differed for the O-mode and X-mode HF pumping towards the magnetic zenith [41]. Results from a power stepping experiment at f_H = 7.953 MHz demonstrated that the X-mode parametric decay instability excitation threshold was 0.47 V/m. The O-mode persistent plasma and ion-line backscatters, coexisting with artificial field-aligned irregularities, showed an excitation threshold of 0.62 V/m, which exceeded the thresholds for the X-mode HF-enhanced plasma lines and HF-enhanced ion lines, while their intensity was two orders of magnitude less [41]. For the same background conditions and pump frequency, the "classic" resonance parametric decay instability, excited

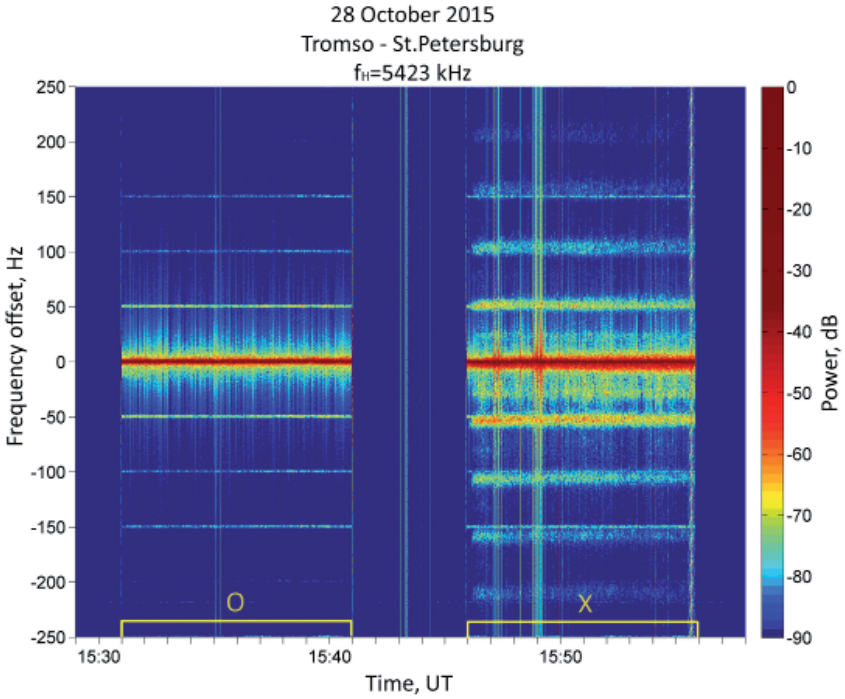

Figure 9. The spectrogram of the narrowband stimulated electromagnetic emission structures recorded at a distance of about 1200 km away from the EISCAT heater for alternating O/X-mode HF pumping towards the magnetic zenith at $f_H = 5.423$ MHz with an effective radiated power of 238 MW on 28 October 2015.

as the immediate response to the onset of the O-mode HF pumping, had a threshold of 0.17 V/m [48], which was much less the excitation threshold of persistent O-mode plasma and ion lines due to the non-resonance instability (0.62 V/m).

7. Narrowband Stimulated Electromagnetic Emission (NSEE)

Recent experiments at EISCAT have demonstrated that an X-mode HF pump wave is capable of exciting various discrete structures in the narrowband stimulated electromagnetic emission (NSEE) spectra (within ±1 kHz of the pump frequency) recorded at 1200 km away from the heating facility [35, 36, 49]. Figure 9 illustrates the spectrogram of the narrowband stimulated electromagnetic emission structures recorded at a distance about 1200 km away from the EISCAT heater for alternating O/X-mode HF pumping at $f_H = 5.423$ MHz on 28 October 2015. An X-mode pump wave reflected at an altitude of about 220 km. In accordance with the IGRF model at an altitude of 220 km, the values of the electron, f_{ce}, and ion (for O^+ ions), f_{ci}, gyro-frequencies were 1.364 MHz and 46.8 Hz, respectively. The pump frequency was thus 33 kHz below $4f_{ce} = 5.456$ MHz.

As seen from Figure 9, only during the X-mode cycle the down and upshifted (relative to the pump frequency) discrete spectral structures (Stokes and anti-Stokes modes), ordered by the ion gyro-frequency (for O^+ ions), were generated. Together with the spectral lines with the maxima at nf_{ci}, where n is the number of the ion gyro-harmonic, the downshifted and occasionally even upshifted spectral components at $0.5f_{ci}$ were also generated. In the course of the O-mode cycle, the discrete spectral structures were not recorded. Only very weak and narrow power-supply harmonic interference at multiples of 50 Hz can be seen during the O-mode transmission pulse.

We provided the first experimental evidence of the sensitivity of phenomena induced by the X-mode HF high-power radio waves to pump frequency stepping through the fifth electron gyro-harmonic ($5f_{ce}$) from below to above [49]. Figure 10 shows the spectrograms of the HF pump wave within a ±250 Hz band taken in the vicinity of St. Petersburg in the course of pump frequency stepping through the fifth electron gyro-harmonic for alternating O-mode and X-mode heating at Tromsø on 25 and 26 October 2013 [49]. The data were obtained with a frequency resolution of 0.2 Hz and a time resolution of 5 s. The strong line in the center with zero frequency offset corresponds to the pump wave frequency. The narrowband stimulated electromagnetic emission band on the spectrograms is represented in such a way that the maximum in the spectrum is at the pump frequency. As evident from Figure 10, during the O-mode pump pulse there were not any spectral structures in the spectrograms. In contrast, X-mode pulses exhibited a wide variety of spectral components.

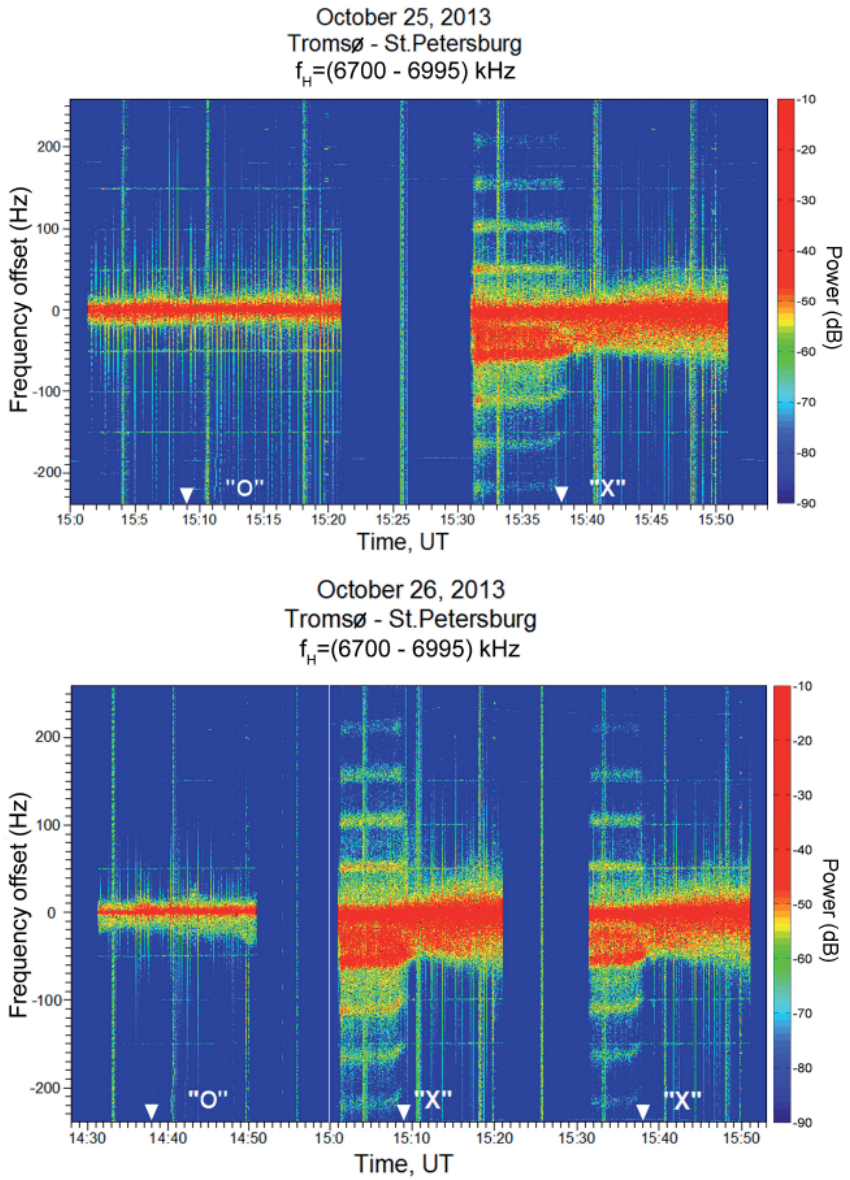

Figure 10. The spectrogram of the narrowband stimulated electromagnetic emission structures recorded with a frequency resolution of 0.2 Hz and a time resolution of 5 s at a distance of 1200 km from EISCAT/heating for alternating O/X-mode HF pumping towards the magnetic zenith on 25 and 26 October 2013 in the course of pump frequency stepping from 6.7 MHz to 6.995 MHz by 5 kHz steps every 20 s across the fifth electron gyro-harmonic. The effective radiated power varied between 657 MW to 715 MW and 456 MW to 501 MW in different transmission pulses. The strong line in the center with zero frequency offset was the pump wave. The narrowband stimulated electromagnetic emission band is represented in such a way that the maximum in the spectrum at the pump frequency corresponded to zero frequency offset at any time. Arrows indicate the time when $f_H = 5f_{ce}$ (adapted from Blagoveshchenskaya et al. [49]).

At pump frequencies $f_H < 5f_{ce}$, the narrowband stimulated electromagnetic emission spectra exhibited very intense downshifted and upshifted discrete structures ordered by the ion gyro-frequency (for O^+ ions). They are similar to the discrete spectral components observed below $4f_{ce}$ (see Figure 9). As the pump frequency reached $5f_{ce}$, discrete spectral lines were greatly suppressed and disappeared in the vicinity of $5f_{ce}$ and did not reappear at $f_H > 5f_{ce}$ [49].

It is suggested that the spectral structures observed below $4f_{ce}$ and $5f_{ce}$ are related to the magnetized stimulated Brillouin scatter (MSBS) process, when the HF pump wave directly decays into the ion gyro-harmonic and a backscattered electromagnetic wave. Artificial field-aligned irregularities play a key role for the narrowband stimulated electromagnetic emission occurrence at a large distance from the EISCAT/Heating. Backscattered EM waves, generated due to the magnetized stimulated Brillouin scatter process, are scattered from artificial field-aligned irregularities and are capable of propagating to a large distance from the heating facility without significant attenuation.

8. Concluding Remarks

In the last 50 years, most HF pumping experiments in the upper ionosphere (*F* region) at different ground-based HF heating facilities in the world were carried out with the use of ordinary polarized (O-mode) powerful HF radio waves. We have presented the first experimental evidence showing that extraordinary (X-mode) powerful HF radio waves, injected into the high-latitude ionospheric F2 layer towards the magnetic zenith, are capable of generating artificial field-aligned irregularities, radio-induced optical emissions at red (630 nm) and green (557.7 nm) lines, strong electron acceleration leading to N_e enhancements, ion-acoustic and Langmuir electrostatic waves, and spectral components in the narrowband stimulated electromagnetic emission spectra observed at a large distance from the HF heater. The results obtained were briefly reported in Sections 3 through 7.

In spite of the fact that the excitation of various unexpectedly strong X-mode phenomena in the F region of the high-latitude ionosphere is a repeatable and easily reproducible feature from EISCAT heating experiments, many aspects of the nonlinear interaction between an X-polarized HF pump wave and the ionospheric plasma still remain poorly understood. Up to the present, an adequate theory describing the interactions between the X-mode HF pump wave and ionospheric plasma is absent. Further clarification and theoretical background are needed to explain the origin of unusually strong phenomena excited in the ionospheric *F*-region by X-polarized HF pump waves.

Langmuir and ion-acoustic turbulence, seen as HF-enhanced ion and plasma lines (HFIL and HFPL) in the incoherent radar spectra, are indicative of the parametric decay instability (PDI). However, it is not clear through what mechanism an X-mode pump wave can excite the parametric decay instability and even the modulational instability (MI), especially taking into account that the X-mode HF-enhanced ion line and HF-enhanced plasma line are of much higher intensity, as compared with the O-mode effects, and were observed throughout the whole HF pump pulse and coexist with strong artificial small-scale field-aligned irregularities.

Strong N_e enhancements from EISCAT UHF radar measurements are typical for X-mode pumping and observed as often as the T_e enhancements under the action of O-polarized HF pump waves. They occurred along the magnetic field line in a wide altitude range, whether or not the HF-enhanced ion and plasma lines were excited. The origin of such N_e enhancements under X-mode HF pumping is not yet fully understood and needs clarification. In principle, the accelerated electrons can produce the enhanced ionization. Hence, an efficient mechanism of the electron acceleration induced by an X-polarized pump wave should be found.

The generation mechanisms of narrowband discrete spectral structures observed under X-mode HF pumping at a large distance from an HF heating facility are not clearly understood and require a solid theoretical basis.

The new EISCAT_3D radar [50] planned to run in 2022 will provide unprecedented temporal and spatial resolution measurements with an extended coverage in height and horizontal extent of the heated volume. It can provide the detailed investigations of the various X-mode phenomena occurring in the magnetic field-aligned direction, including large-scale and small-scale field-aligned irregularities, Langmuir and ion-acoustic plasma waves with high temporal and spatial resolution, and N_e enhancements due to the acceleration of electrons. However, the location of the existing EISCAT HF heating facility cannot provide field-aligned measurements with the use of the EISCAT_3D radar. A new HF heating facility, located in close proximity to the EISCAT_3D site, is needed to realize the three-dimensional capabilities of the new radar. The combination of the EISCAT_3D radar with a new HF heating facility will provide answers to many outstanding scientific questions related to the nonlinear interaction between powerful electromagnetic waves and the high-latitude ionospheric plasma.

9. Acknowledgements

EISCAT is an international scientific association supported by research organizations in China (CRIRP), Finland (SA), Japan (NIPR and STEL), Norway (NFR), Sweden (VR), and the United Kingdom (NERC). The author is thankful to members of her team, especially Dr. T. D. Borisova, Dr. A. S. Kalishin, V. A. Kornienko, and D. D. Rogov. She is also grateful to colleagues with whom she collaborated in the past or is collaborating with in the present time, namely Prof. Bo Thidé, Prof. A. Brekke, Prof. T. Yeoman, Dr. M. Kosch, Dr. I. Häggström, Dr. M. Rietveld, and Dr. U. Brändsröm. The author thanks Prof. A. Pellinen-Wannberg for valuable discussions.

10. References

1. N. F. Blagoveshchenskaya, V. A. Kornienko, T. D. Borisova, B. Thidé, M. J. Kosch, M. T. Rietveld, E. V. Mishin, R. Y. Luk'yanova, and O. A. Troschichev, "Ionospheric HF Pump Wave Triggering of Local Auroral Activation," *Journal of Geophysical Research*, **106**, A12, 2001, pp. 29071-29090.

2. N. F. Blagoveshchenskaya, V. A. Kornienko, T. D. Borisova, M. T. Rietveld, T. Bösinger, B. Thidé, T. B. Leyser, and A. Brekke," Heater-Induced Phenomena in a Coupled Ionosphere-Magnetosphere System," *Advances of Space Research*, **38**, 2006, pp. 2495-2502, https://doi.org/10.1016/j.asr.2004.12.047.

3. N. F. Blagoveshchenskaya, T. D. Borisova, V. A. Kornienko, B. Thidé, M. T. Rietveld, M. J. Kosch, and T. Bösinger, "Phenomena in the Ionosphere – Magnetosphere System Induced by Injection of Powerful HF Radio Waves into Nightside Auroral Ionosphere," *Annales Geophysicae*, **23**, 2005, pp. 87-100.

4. V. A. Kornienko, N. F. Blagoveshchenskaya, T. D. Borisova, B. Thidé, and A. Brekke, "Modification of the Local Substorm Ionospheric and Field-Aligned Currents Produced by the Tromsø Heating Facility," *International Journal of Geomagnetism and Aeronomy*, **4**, 1, 2003, pp. 37-46.

5. N. F. Blagoveshchenskaya, *Geophysical Effects of Active Impacts in Near-Earth Space* (in Russian), St. Petersburg, Gidrometeoizdat, 2001.

6. T. D. Borisova, N. F. Blagoveshchenskaya, V. A. Kornienko, M. T. Rietveld, B. Thidé, and T. B. Leyser, "Ionospheric Effects Observed when the Tromsø HF Heating Facility Was Turned On/Off," *Geomagnetism and Aeronomy*, **45**, 3, 2005, pp. 367-374.

7. M. T. Rietveld, M. J. Kosch, N. F. Blagoveshchenskaya, V. A. Kornienko, T. B. Leyser, and T. K. Yeoman, "Ionospheric Electron Heating, Aurora and Striations Induced by Powerful HF Radio Waves at High Latitudes: Aspect Angle Dependence," *Journal of Geophysical Research*, **108**, A4, 2003, 1141, doi:10.1029/2002 JA 009543.

8. M. J. Kosch, H. Vickers, Y. Ogawa, A. Senior, and N. Blagoveshchenskaya, "First Observation of the Anomalous Electric Field in the Topside Ionosphere by Ionospheric Modification over EISCAT," *Geophysical Research Letters*, **41**, 2014, doi:10.1002/2014GL061679.

9. N. F. Blagoveshchenskaya, V. A. Kornienko, A. V. Petlenko, A. Brekke, and M. T. Rietveld, "Geophysical Phenomena During an Ionospheric Modification Experiment at Tromsø," *Annales Geophysicae*, **16**, 1998, pp. 1212-1225.

10. T. D. Borisova, N. F. Blagoveshchenskaya, V. A. Kornienko, and M. Rietveld, "Characteristics of *Pc*4-5 Pulsations Obtained by the HF Radio Wave Bi-Static Backscatter Method Using the HF EISCAT/Heating Facility and Ground Magnetometers," *Geomagnetism and Aeronomy*, **51**, 4, 2011, pp. 630-642.

11. T. D. Borisova, N. F. Blagoveshchenskaya, I. M. Ivanova, and M. T. Rietveld, "Dependence of the *Pc*4 Magnetic Pulsation Parameters on the Radiated Power of the EISCAT HF Heating Facility," *Geomagnetism and Aeronomy*, 53, 1, 2013, pp. 32-42, doi:10.1134/S0016793213010040.

12. N. F. Blagoveshchenskaya, V. A. Kornienko, T. D. Borisova, I. V. Moskvin, M. T. Rietveld, V. L. Frolov, V. P. Uryadov, L. M. Kagan, Yu. M. Yampolski, V. L. Galushko, A. V. Koloskov, S. B. Kasheev, A. V. Zalizovski, G. G. Vertogradov, V. G. Vertogradov, and M. C. Kelley, "Probing of Medium-Scale Traveling Ionospheric Disturbances Using HF-Induced Scatter Targets," *Annales Geophysicae*, **24**, 2006, pp. 2333-2345.

13. T. R. Robinson, "The Heating of the High Latitude Ionosphere by High Power Radio Waves," *Physics Reports*, **179**, 1989, pp.79-209.

14. A. V. Gurevich, "Nonlinear Effects in the Ionosphere," *Physics-Uspekhi*, **50**, 2007, pp. 1091-1121.

15. A. V. Streltsov, et al., "Past, Present and Future of Active Radio Frequency Experiments in Space," *Space Science Review*, **214**, 118, 2018, https://doi.org/10.1007/s11214-018-0549-7.

16. N. F. Blagoveshchenskaya, V. A. Kornienko, M. T. Rietveld, B. Thidé, A. Brekke, I. V. Moskvin, and S. Nozdrachev, "Stimulated Emissions Around the Second Harmonic of Tromsø Heater Frequency Observed by Long-Distance Diagnostic HF Tools," *Geophysical Research Letters*, **25**, 1998, pp. 873-876.

17. N. F. Blagoveshchenskaya, T. D. Borisova, V. A. Kornienko, T. B. Leyser, M.T. Rietveld, and B. Thidé, "Artificial Field-Aligned Irregularities in Night-Side Auroral Ionosphere," *Advances in Space Research*, **38**, 2006, pp. 2503-2510.

18. N. F. Blagoveshchenskaya, V. A. Kornienko, A. Brekke, M. T. Rietveld, M.J Kosch, T. D. Borisova, and M. V. Krylosov, "Phenomena Observed by HF Long-Distance Tools in the HF Modified Auroral Ionosphere During Magnetospheric Substorm," *Radio Science*, **34**, 1999, pp. 715-724.

19. T. D. Borisova, N. F. Blagoveshchenskaya, I. V. Moskvin, M. T. Rietveld, M. J. Kosch, and B. Thidé, "Doppler Shift Simulation of Scattered HF Signals During the Tromsø HF Pumping Experiment on 16 February, 1996," *Annales Geophysicae*, **20**, 2002, pp. 1479-1486.

20. N. F. Blagoveshchenskaya, H. C. Carlson, V. A. Kornienko, T. D. Borisova, M. T. Rietveld, T. K. Yeoman, and A. Brekke, "Phenomena Induced by Powerful HF Pumping Towards Magnetic Zenith with a Frequency Near the *F*-region Critical Frequency and the Third Electron Gyro Harmonic Frequency," *Annales Geophysicae*, **27**, 2009, pp. 131-145.

21. N. F. Blagoveshchenskaya, T. D. Borisova, T. K. Yeoman, and M. T. Rietveld, "The Effects of Modification of a High-Latitude Ionosphere by High-Power HF Radio Waves. Part 1. Results of Multi-Instrument Ground-Based Observations," *Radiophysics and Quantum Electronics*, **53**, 2011, pp. 512-531.

22. T. D. Borisova, N. F. Blagoveshchenskaya, A. S. Kalishin, M. J. Kosch, A. Senior, M. T. Rietveld, T. K. Yeoman, and I. Hägström, "Phenomena in the High-Latitude Ionospheric *F* Region Induced by a HF Heater Wave at Frequencies Near the Fourth Electron Gyroharmonic," *Radiophysics and Quantum Electronics*, **57**, 2014, pp. 1-19.

23. T. D. Borisova, N. F. Blagoveshchenskaya, A. S. Kalishin, M. T. Rietveld, T. K. Yeoman, and I. Hägström, "Modification of the High-Latitude Ionospheric *F* Region by High-Power HF Radio Waves at Frequencies Near the Fifth and Sixth Electron Gyroharmonics," *Radiophysics and Quantum Electronics*, **58**, 2016, pp. 561-585.

24. T. D. Borisova, N. F. Blagoveshchenskaya, M. T. Rietveld, and I. Häggström, "Outshifted Plasma Lines Observed in Heating Experiments in the High-Latitude Ionosphere at Pump Frequencies Near Electron Gyroharmonic," *Radiophysics and Quantum Electronics*, **61**, 10, 2019, pp. 722-740.

25. M. T. Rietveld, A. Senior, J. Markkanen, and A. Westman, "New Capabilities of the Upgraded EISCAT High-Power HF Facility," *Radio Science*, **51**, 9, 2016, pp. 1533-1546, doi:10.1002/2016RS006093.

26. H. Rishbeth and T. van Eyken, "EISCAT: Early History and the First Ten Years of Operation," *Journal of Atmospheric and Solar-Terrestrial Physics*, **55**, 1993, pp. 525-542.

27. M. Lester, et al., "Stereo CUTLASS: A New Capability for the SuperDARN Radars," *Annales Geophysicae*, **22**, 2004, pp. 459-473.

28. U. Brändström, *The Auroral Large Imaging System – Design, Operation and Scientific Results*, PhD thesis, Swedish Institute of Space Physics, Kiruna, Sweden, October 2003 (IRF Scientific Report 279), ISBN: 91-7305-405-4.

29. N. F. Blagoveshchenskaya, T. D. Borisova, V. A. Kornienko, V. L. Frolov, M. T. Rietveld, and A. Brekke, "Some Distinctive Features in the Behavior of Small-Scale Artificial Ionospheric Irregularities at Mid- and High Latitudes," *Radiophysics and Quantum Electronics*, **50**, 8, 2007, pp. 619-632.

30. D. D. Rogov, N. F. Blagoveshchenskaya, and T. K. Yeoman, "Features of Artificial Ionospheric Irregularities Induced by Powerful HF Radio Waves from Bi-Static Scatter Measurements," Conference Radiation and Scattering of Electromagnetic Waves (RSEMW) 2019, doi:10.1109/RSEMW.2019.8792727.

31. N. F. Blagoveshchenskaya, T. D. Borisova, T. Yeoman, M. T. Rietveld, I. M. Ivanova, and L. J. Baddeley, "Artificial Field-Aligned Irregularities in the High-Latitude *F* Region of the Ionosphere Induced by an X-mode HF Heater Wave," *Geophysical Research Letters*, **38**, 2011, L08802, doi: 10.1029/2011GL046724.

32. N. F. Blagoveshchenskaya, T. D. Borisova, M. T. Rietveld, T. K. Yeoman, D. M. Wright, M. Rother, H. Luhr, E. V. Mishin, and C. Roth, "Results of Russian Experiments Dealing with the Impact of Powerful HF Radiowaves on the High Latitude Ionosphere Using the EISCAT Facilities," *Geomagnetism and Aeronomy*, **51**, 8, 2011, pp. 1109-1120.

33. N. F. Blagoveshchenskaya, T. D. Borisova, T. K. Yeoman, M. T. Rietveld, I. Häggström, and I. M. Ivanova, "Plasma Modifications Induced by an X-mode HF Heater Wave in the High Latitude *F* Region of the Ionosphere," *Journal of Atmospheric and Solar-Terrestrial Physics*, **105-106**, 2013, pp. 231-244.

34. N. F. Blagoveshchenskaya, T. D. Borisova, M. Kosch, T. Sergienko, U. Brändström, T. K. Yeoman, and I. Häggström, "Optical and Ionospheric Phenomena at EISCAT Under Continuous X-Mode HF Pumping," *Journal of Geophysical Research: Space Physics*, **119**, 2014, pp. 10,483-10,498, doi:10.1002/ 2014JA020658.

35. N. F. Blagoveshchenskaya, T. D. Borisova, T. K. Yeoman, I. Häggström, and A. S. Kalishin, "Modification of the High Latitude Ionosphere *F* Region by X-Mode Powerful HF Radio Waves: Experimental Results from Multi-Instrument Diagnostics," *Journal of Atmospheric and Solar-Terrestrial Physics*, **135**, 2015, pp. 50-63, https://doi.org/10.1016/j.jastp.2015.10009.

36. N. F. Blagoveshchenskaya, T. D. Borisova, A. S. Kalishin, V. N. Kayatkin, T. K. Yeoman, and I. Häggström, "Comparison of the Effects Induced by the Ordinary (O-Mode) and Extraordinary (X-Mode) Polarized Powerful HF Radio Waves in the High-Latitude Ionospheric *F* Region," *Cosmic Research*, **56**, 1, 2018, pp. 11-25.

37. N. F. Blagoveshchenskaya, T. D. Borisova, A. S. Kalishin, T. K. Yeoman, Yu. A. Schmelev, and E. E. Leonenko, "Characterization of Artificial, Small-Scale,

Ionospheric Irregularities in the High-Latitude *F* Region Induced by High-Power, High-Frequency Radio Waves of Extraordinary Polarization," *Geomagnetism and Aeronomy*, **59**, 6, 2019, pp.759-773.

38. N. Borisov, F. Honary, and H. Li, Excitation of Plasma Irregularities in the *F*-Region of the Ionosphere by Powerful HF Radio Waves of X-polarization, *Journal of Geophysical Research: Space Physics*, **123**, 2018, pp.5246-5260, doi.org/10.1029/2018JA025530.

39. S. Kuo, "Ionospheric Modifications in High Frequency Heating Experiments," *Physics Plasmas*, **22**, 2015, 012901, doi: 10.1063/1.4905519.

40. M. J. Kosch, Y. Ogawa, M. T. Rietveld, S. Nozawa, and R. Fujii, "An Analysis of Pump-Induced Artificial Ionospheric Ion Upwelling at EISCAT," *Journal of Geophysical Research*, **115**, 2010, A12317, doi:10.1029/2010JA015854.

41. N. F. Blagoveshchenskaya, T. D. Borisova, A. S. Kalishin, T. K. Yeoman, and I. Häggström, "Distinctive Features of Langmuir and Ion-Acoustic Turbulences Induced by O- and X-Mode HF Pumping at EISCAT," *Journal of Geophysical Research: Space Physics*, **125**, 2020, doi: 10.1029/2020JA028203.

42. M. T. Rietveld and A. Senior, "Ducting of Incoherent Scatter Radio Waves by Field-Aligned Irregularities," *Annales Geophysicae*, 2020, in press, doi: 105194/angeo-2020-22.

43. H. C. Carlson, V. B., Wickwar, and G. P. Mantas, "Observations of Fluxes of Suprathermal Electrons Accelerated by HF excited Instabilities," *Journal of Atmospheric and Solar-Terrestrial Physics*, **44**, 1982, pp. 1089-1100.

44. T. Hagfors, W. Kofman, H. Kopka, P. Stubbe, and T. Äijänen, "Observations of Enhanced Plasma Lines by EISCAT During Heating Experiments," *Radio Science*, **18**, 1983, pp. 861-866.

45. P. Stubbe, H. Kohl, and M. T. Rietveld, "Langmuir Turbulence and Ionospheric Modification," *Journal of Geophysical Research*, **97**, 1992, pp. 6285-6297.

46. N. F. Blagoveshchenskaya, T. D. Borisova, and T. K. Yeoman (2017), "Comment on the Article 'Parametric Instability Induced by X-Mode Wave Heating at EISCAT' by Wang et al. (2016)," *Journal of Geophysical Research: Space Physics*, **122**, 2017, pp. 12,570-12,586, https://doi.org/10.1002/2017JA023880.

47. T. D. Borisova, N. F. Blagoveshchenskaya, T. K. Yeoman, and I. Häggström, "Excitation of Artificial Ionospheric Turbulence in the High-Latitude Ionospheric *F* Region as a Function of the EISCAT/Heating Effective Radiated Power," *Radiophysics and Quantum Electronics*, **60**, 4, 2017, https://doi.org/10.1007/s11141-017-9798-7.

48. C. Bryers, M. Kosch, A. Senior, M. T. Rietveld, and T. K. Yeoman, "The Thresholds of Ionospheric Plasma Instabilities Pumped by High-Frequency Radio Waves at EISCAT," *Journal of Geophysical Research: Space Physics*, **118**, 2013, pp. 7472-7481.

49. N. F. Blagoveshchenskaya, T. D. Borisova, A. S. Kalishin, T. K. Yeoman, and I. Häggström, "First Observations of Electron Gyro-Harmonic Effects Under X-Mode HF Pumping the High Latitude Ionospheric *F*-Region," *Journal of Atmospheric and Solar-Terrestrial Physics*, **155**, 2017, pp. 36-49, doi:10.1016/j.jastp.2017.02.003.

50. I. McCrea, A. Aikio, L. Alfonsi, E. Belova, S. Buchert, M. Clilverd, N. Engler, B. Gustavsson, C. Heinselman, J. Kero, M. Kosch, H. Lamy, T. Leyser, Y. Ogawa, K. Oksavik, A. Pellinen-Wannberg, F. Pitout, M. Rapp, I. Stanislawska, and J. Vierinen, "The Science Case for the EISCAT_3D Radar," *Progress in Earth and Planetary Science*, **2**, 2015, https://doi.org/10.1186/s40645-015-0051-8.

Radiation-Pattern Reconfigurable and Wideband Vector Antenna for 3-D Direction Finding

J. Duplouy[1,2], C. Morlaas[1], H. Aubert[2], P. Potier[3], and P. Pouliguen[3]

[1]ENAC, TELECOM-EMA
Université de Toulouse
F-31055 Toulouse, France
E-mail: johan.duplouy@gmail.com

[2]LAAS-CNRS, MINC
Université de Toulouse
F-31400 Toulouse, France

[3]DGA
F-75509 Paris, France

Abstract

The direction-finding performance of a radiation-pattern reconfigurable and wideband vector antenna is reported. This eight-port vector antenna consisted of the arrangement of circular arrays of Vivaldi antennas. Accurate estimation of the direction of arrival of an incoming vertically- or horizontally-polarized electromagnetic field across the three-dimensional upper half-space was achieved over a frequency bandwidth of 8.2:1 thanks to radiation-pattern reconfigurability. The proposed vector antenna offered the opportunity of using more radiation patterns than those commonly used in standard vector antennas for estimating the direction of arrival of incoming electromagnetic fields, which led to better estimation accuracy. Measurement results were found to be in good agreement with the simulated results obtained from full-wave electromagnetic simulations.

1. Introduction

Direction finding (DF) aims to estimate the direction-of-arrival (DoA) of incoming electromagnetic (EM) fields. This estimation is nowadays increasingly needed in numerous civil and military applications, such as navigation, electronic warfare, object tracking, search and rescue, and radio astronomy [1]. The latest technical inquiries for these applications are approaching the characteristics of the ideal direction finder, which are the direction of arrival estimation of incoming EM fields over the three-dimensional space (i.e., 360° of azimuth and 180° of elevation), considering their polarizations and within a wide frequency range thanks to a low-profile and compact antenna. However, most of the commercially available (see, e.g., [2-4]) or published (see, e.g., [5-6]) direction-finding antennas operate in the VHF or UHF band and offer only a two-dimensional angular coverage (i.e., only the azimuth angle of the direction of arrival can be estimated for a restricted range of elevation angles of directions of arrival). The direction-of-arrival estimation generally relies on the spatial diversity of the antenna array [7], and cannot be straightforwardly applied to design wideband direction-finding antennas targeting a three-dimensional angular coverage. Such coverage can be obtained by using an innovative direction-finding technique that allows the direction-of-arrival derivation from the measurement of the different components of the incoming EM field (ideally, the six Cartesian components, E_x, E_y, E_z, H_x, H_y, and H_z), thanks to a vector antenna (VA) [8]. Vector antennas are multi-port antennas composed of three electric dipoles and three magnetic dipoles, all spatially collocated with orthogonal orientations. Each component of the incoming EM field is hence measured through the radiation pattern (RP) of the relevant dipole. These are gaining prominence nowadays since a single vector antenna is sufficient to estimate the direction of arrival of an incoming EM field over the three-dimensional space regardless of its polarization, and notably allows compactness by substituting for a large antenna array. First, attention was mainly focused on the implementation of wideband and active vector-antenna structures [9, 10]. Second, a passive and dual-band vector antenna operating at GSM frequencies that allowed only the direction-of-arrival estimation of vertically-polarized EM fields was proposed in [11]. Fully passive vector antennas do not suffer from the intrinsic and strong limitations of active antennas, but the wideband coverage was very challenging to achieve. Recently, the authors reported first a passive, wideband and radiation-pattern reconfigurable vector antenna [12, 13]. The prototype of this vector

Figure 1a. A photograph of the Four Season vector antenna prototype (from [14]).

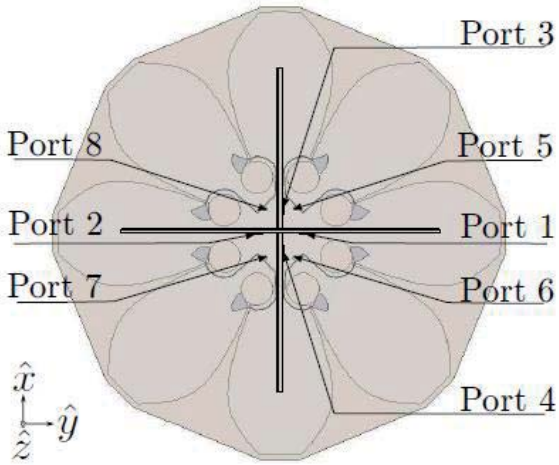

Figure 1b. The numbering of the ports of the Four Season vector antenna (from [14]).

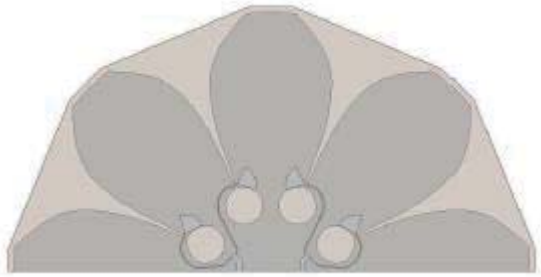

Figure 1c. The Four Season vector antenna vertical array and feeding circuit (from [14]).

antenna was only able to estimate the direction of arrival of vertically-polarized EM fields over an impedance bandwidth of 1.69:1 (or 2.10 GHz to 3.55 GHz), since only three components could be measured (E_z, H_x, and H_y). In [13], a new direction-finding technique was also proposed for radiation-pattern-reconfigurable vector antennas in order to enhance their direction-finding performance across the overall frequency bandwidth. This technique consisted of selecting and using additional radiation-pattern diversity in the direction-of-arrival estimation process. Very recently, the authors proposed the *Four Season* vector antenna [14], based on the design of the vector antenna reported in [12, 13]. A preliminary evaluation of the direction-finding performance was performed and demonstrated that this vector antenna enables the estimation of the direction of arrival of incoming vertically and horizontally polarized EM fields in the three-dimensional upper half-space over a wider bandwidth (7:1 or 1 GHz to 7 GHz).

In this article, the direction-finding performance of the Four Season vector antenna is evaluated in detail, including the evaluation of the prototype's sensitivity for direction-of-arrival estimation errors below 5° in the three-dimensional upper half-space. Moreover, the simulated and measured direction-finding performance is assessed using the new direction-finding technique proposed by the authors in [13], and compared with the preliminary performance reported in [14] (obtained without using this technique). The direction-finding performance evaluation shows the benefits of this technique.

The paper is organized as follows. The key characteristics of the Four Season vector antenna are summarized in Section 2. The selection of the additional radiation-pattern diversity to be used in the direction-of-arrival estimation process is reported in Section 3. The evaluation of direction-finding performance is investigated in Section 4. The conclusion and future directions are given in Section 5.

2. The Four Season Vector Antenna

In this section, the main characteristics of the passive, wideband, and radiation-pattern reconfigurable Four Season vector antenna, recently reported by the authors [14], are summarized (see Figure 1). The topology of this vector antenna can be divided into two parts. The vertical part consists of two spatially collocated and orthogonally oriented dual-port semi-circular arrays of four Vivaldi antennas. The horizontal part consists of a circular array of eight Vivaldi antennas. As shown in Figure 1, each port is associated with two Vivaldi antennas. Therefore, this vector antenna has a total of eight ports: four ports (ports numbers from 1 to 4) are associated with the vertical part, and four ports (ports numbers from 5 to 8) are associated with horizontal part. The vertical part enables the measurement of three components of the incoming EM field (namely, E_z, H_x, and H_y), while the horizontal part permits the measurement of the other three components (namely, H_z, E_x, and E_y). Each of these two triplets respectively allows the estimation of the direction of arrival of a vertically or

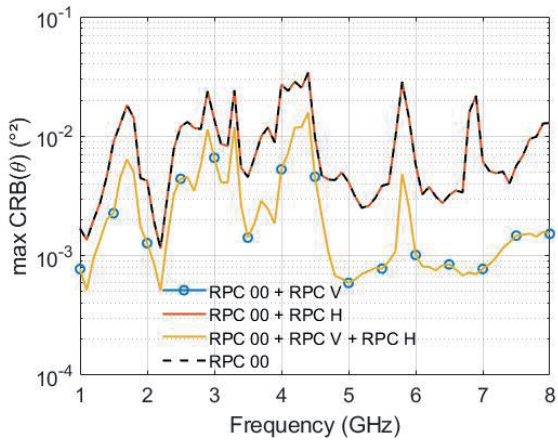

Figure 2a. The highest simulated Cramer-Rao bound (θ) of the Four Season vector antenna for an incoming vertically-polarized EM field obtained using different RPCs added to RPC 00.

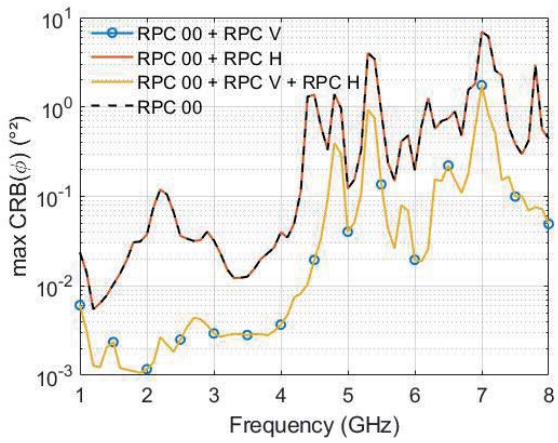

Figure 2b. The highest simulated Cramer-Rao bound (ϕ) of the Four Season vector antenna for an incoming vertically-polarized EM field obtained using different RPCs added to RPC 00.

horizontally polarized incoming EM field. Following [13] and [14], the measurements of the EM field components are derived from six sets of weighting coefficients assigned to the received signals thanks to the ability to reconfigure the radiation pattern of the Four Season vector antenna. These sets of weighting coefficients are given in Table 1, and are denoted by the acronym RPC 00 (Radiation Patterns Combination). The constitutive radiating elements exhibited a measured bandwidth of 6.77:1 (for a $\text{VSWR} \leq 2.3$) between 1.24 GHz and 8.40 GHz. The antenna was included in a half-sphere within a 0.47λ radius, where λ is the free-space wavelength at 1.24 GHz. The electrical performance in terms of impedance matching and radiation-pattern properties of the Four Season vector antenna were measured in an anechoic chamber, and results were available in [14]. They were in good agreement with the data obtained from full-wave EM simulations (*HFSS* software).

Table 1. The set of weighting coefficients assigned to the signal received by the eight-port Four Season vector antenna for measuring the six components of an incoming EM field.

RPC 00	Port Number							
	1	2	3	4	5	6	7	8
E_x	0	0	0	0	1	–1	–1	1
E_y	0	0	0	0	1	1	–1	–1
E_z	1	1	1	1	0	0	0	0
H_x	1	–1	0	0	0	0	0	0
H_y	0	0	1	–1	0	0	0	0
H_z	0	0	0	0	1	–1	1	–1

3. Selection of Additional Radiation Patterns to be Used in the Direction-Finding Process

In this section, we select more sets of weighting coefficients (or accordingly, more radiation patterns) to be used in addition to RPC 00 in the direction-finding process in order to enhance the accuracy of the direction-of-arrival estimation provided by the Four Season vector antenna. These radiation patterns were chosen from an innovative method proposed by the authors in [13], which was based on the Cramer-Rao bound (CRB). The main advantage of this method is the independence regarding the direction-of-arrival estimation technique used for evaluating the direction-finding performance of the vector antenna. The objective of this method consists of selecting the additional RPC (defined as different sets of weighting coefficients providing the same radiation pattern with a rotation of 90° in the azimuthal plane) that maximizes the estimation accuracy across the entire frequency bandwidth. More specifically, the proposed method consists of choosing between several RPCs, the RPC that provides the smallest Cramer-Rao bound (in azimuth and elevation) when added to RPC 00. As in [13], we limited the possible values for the weighting coefficients β_i to $\{1, 0, -1\}$ $(i \in [1;8])$. 3^8 sets of weighting coefficients $[\beta_1, \beta_2, \beta_3, \beta_4, \beta_5, \beta_6, \beta_7, \beta_8]$ are available and could be assigned to the signals received by the eight-port antenna. Among these 6561 sets, we considered only the sets of the form $[\beta_1, \beta_2, \beta_3, \beta_4, 0, 0, 0, 0]$ and $[0, 0, 0, 0, \beta_5, \beta_6, \beta_7, \beta_8]$ in order to simplify the RPC selection. The vertical and horizontal parts of the Four Season vector antenna were therefore independently considered in order to respectively improve the direction-of-arrival estimation for vertically and horizontally polarized incoming EM fields. Consequently, two kinds of RPCs (RPC V and RPC H) were selected, one for each polarization. According to this independency, there were only 2 × 34 sets to investigate, which yielded

	Port Number							
	1	2	3	4	5	6	7	8
RPC V	1	1	1	–1	0	0	0	0
	–1	1	1	1	0	0	0	0
	1	–1	1	1	0	0	0	0
	1	1	1	–1	0	0	0	0
RPC H	0	0	0	0	1	1	1	–1
	0	0	0	0	–1	1	1	1
	0	0	0	0	1	–1	1	1
	0	0	0	0	1	1	1	–1

Table 2. Selected RPC V and RPC H with their associated set of weighting coefficients.

a total of 2 × 11 RPCs. For the sake of brevity, the sets of weighting coefficients of the tested RPCs associated with the vertical and horizontal part of the vector antennas are not written here. Only the additional weighting coefficients of the selected RPC V and RPC H are reported in Table 2. For both polarizations of the incoming EM field, the Cramer-Rao bound on θ and ϕ was computed using the parameters of [13] for the 22 RPCs, except that the study was performed from 1 GHz to 8 GHz with a 0.1 GHz frequency step. For the sake of readability, Figures 2 and 3 show only the RPCs that ensure the highest precision across the overall bandwidth and for both polarizations. The Cramer-Rao bound obtained from using only RPC 00 are also set out for comparison purposes. Globally, RPC V was more effective than RPC H for enhancing the direction-finding performance. Moreover, it can be noted that RPC H was completely inefficient in improving the direction-finding accuracy when the incoming EM field was vertically polarized. However, it can be observed that the use of both RPC V and RPC H in addition to RPC 00 slightly improved the direction-finding performance. Nonetheless, the estimation accuracy was clearly enhanced across the entire bandwidth for both polarizations thanks to additional radiation-pattern diversity. Besides, RPC H had less impact on the Cramer-Rao bound for a horizontally-polarized EM field compared to RPC V for a vertically-polarized EM field because the estimation was already more accurate using only RPC 00 for a horizontally polarized EM field (Figure 3b) than for a vertically-polarized EM field (Figure 2b). Finally, the authors would like to point out that better direction-finding performance may be obtained by taking account of a huge amount of sets of weighting coefficients of the form $[\beta_1, \beta_2, \beta_3, \beta_4, \beta_5, \beta_6, \beta_7, \beta_8]$ and also by considering complex values for selecting the additional RPCs. However, since the resulting number of possibilities would increase, the process of selection by computing and analyzing the Cramer-Rao bound would be more time consuming.

4. Measurement of the Direction-Finding Performance of the Four Season Vector Antenna Using Additional Radiation Patterns

4.1 Measured Direction-Finding Performance Using the Additional Radiation Patterns

The accuracy of the direction-of-arrival estimation can be derived from using the Four Season vector antenna and the MUSIC (MUltiple Signal Classification) algorithm [15]. In this section, we evaluate the accuracy of the direction-of-arrival estimation of a vertically or horizontally polarized incoming EM field using the measurement of its six components (RPC 00) and additional radiation-pattern diversity (RPC V and RPC H). The scenario used for this evaluation was the same as that defined in [14]. Comparisons between full-wave EM simulations and measurements results were also carried out to validate the predicted

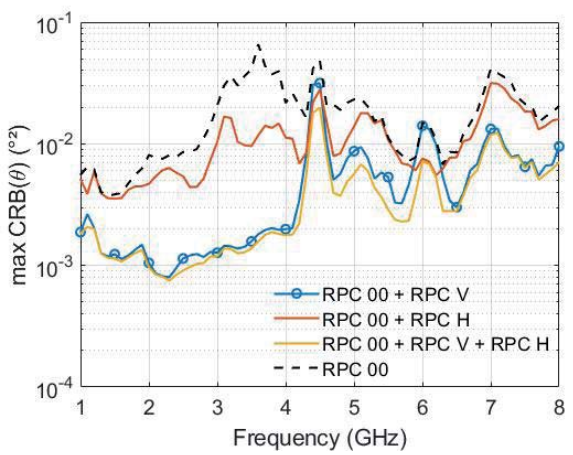

Figure 3a. The highest simulated Cramer-Rao bound (θ) of the Four Season vector antenna for an incoming horizontally-polarized EM field obtained using different RPCs added to RPC 00.

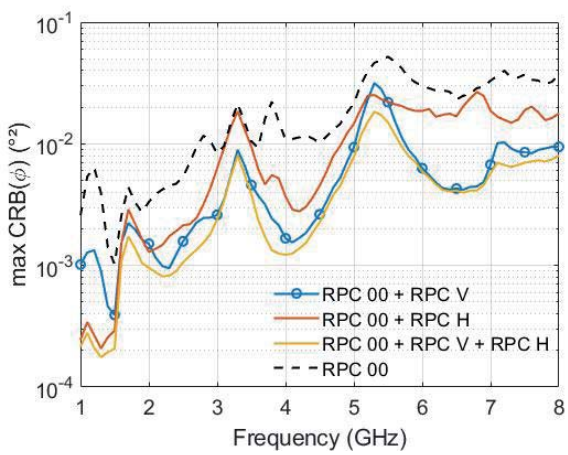

Figure 3b. The highest simulated Cramer-Rao bound (ϕ) of the Four Season vector antenna for an incoming horizontally-polarized EM field obtained using different RPCs added to RPC 00.

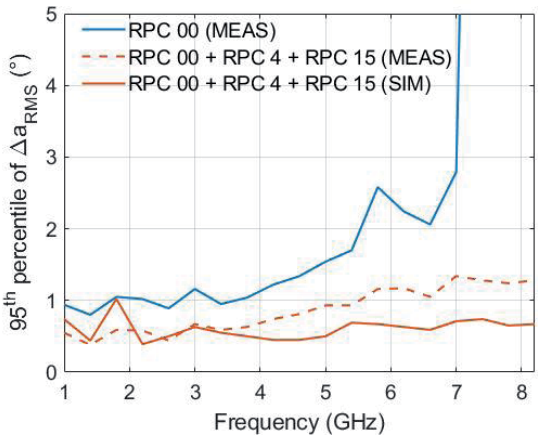

Figure 4a. The 95th percentile of Δa_{RMS} achieved with the Four Season vector antenna when additional radiation-pattern diversity is added to RPC 00 in the direction-of-arrival estimation process of an incoming vertically polarized EM field.

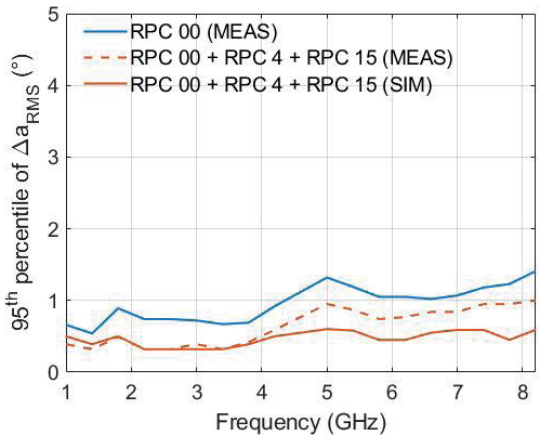

Figure 4b The 95th percentile of Δa_{RMS} achieved with the Four Season vector antenna when additional radiation-pattern diversity is added to RPC 00 in the direction-of-arrival estimation process of an incoming horizontally polarized EM field.

direction-finding performance. As in [14], the accuracy of direction-of-arrival estimation was assessed through the 95th percentile of the angular distance Δa_{RMS} (defined in Appendix A-D of [13]). Figure 4 presents the results of this investigation. The measurement results obtained in [14] when only RPC 00 were used in the direction-finding process were also recalled for comparison purposes. These correspond to the accuracy that can be achieved using only the measurement of the six components of the EM field incident upon the vector antenna. Such a measurement is theoretically sufficient to estimate its direction of arrival. In this case, the measured 95th percentile of Δa_{RMS} was smaller than 2° between 1 GHz to 5.5 GHz and exceeded 5° from 7 GHz if the incoming EM field was vertically polarized. For an incoming horizontally polarized EM field, the measured 95th percentile of Δa_{RMS} was smaller than 2° from 1 GHz to 8.2 GHz. Using additional radiation-pattern diversity, the accuracy was enhanced approximately by a factor of two for both polarizations. The benefits were even more noticeable for a vertically polarized incident EM field in the low end of the frequency range, since the measured 95th percentile of Δa_{RMS} was found to be smaller than 1° over a wider bandwidth (8.2:1 or 1 GHz to 8.2 GHz). The same level of accuracy was also achieved for a horizontally polarized incident EM field thanks to additional radiation-pattern diversity. The improvement of the direction-finding performance was predicted by the Cramer-Rao-bound analysis reported in Figures 2 and 3. It could be observed that the Cramer-Rao bound in azimuth and elevation decreased over the entire bandwidth using RPC V and H, leading to the better estimation accuracy. Globally, there was a reasonably good agreement between measurement and simulation results. The slightly discrepancy at high frequencies could be explained by the fact that the dielectric losses were considered constant in the simulation and did not increase with the frequency as in practice, which was especially disadvantageous with the low-cost substrate (FR-4) used to manufacture the antenna.

4.2 Sensitivity of the Prototype

In this section, we evaluate the sensitivity of the Four Season vector antenna prototype using the additional radiation-pattern diversity (RPC V and RPC H) in the direction-of-arrival estimation process. The sensitivity corresponds to the minimum power density (P_{sensi}) required at the antenna location (for a given noise power level P_n) to estimate the direction of arrival with a required accuracy (defined here as the 95th percentile of $\Delta a_{RMS} \leq 5°$). To evaluate the sensitivity of the prototype, the 95th percentiles of Δa_{RMS} were measured for three frequencies (1.4 GHz, 5 GHz, and 8 GHz) and for different power-densities-to-noise-ratios (PDNR, see Appendix A-A of [13] for the definition), ranging from 12 dB/m^2 to 36 dB/m^2

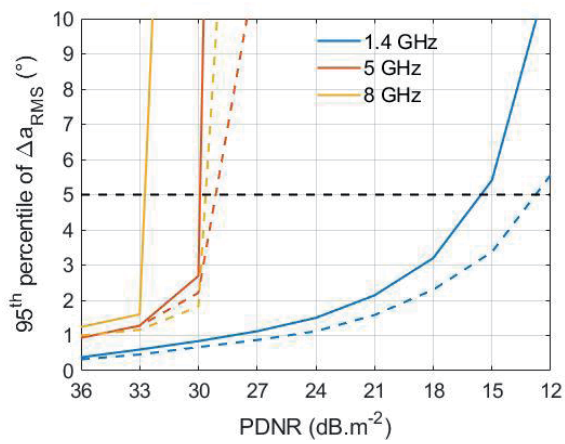

Figure 5. The measured 95th percentile of Δa_{RMS} achieved for different power-densities-to-noise-ratios and when RPC V and RPC H are added to RPC 00 in the direction-of-arrival estimation process of an incoming vertically (solid lines) or horizontally (dashed lines) polarized EM field.

Table 3. The measured sensitivity of the Four Season vector antenna using RPC 00 and RPC V and RPC H.

Frequency	P_{sensi} dBW / m^{-2}	PDNR dBW / m^{-2}
Vertical Polarization		
1.4 GHz	–125	16
5 GHz	–111	30
8 GHz	–108	33
Horizontal Polarization		
1.4 GHz	–128	13
5 GHz	–112	29
8 GHz	–111	30

(with a step of 3 dB). These frequencies corresponded approximately to the lower, central, and upper operating frequencies of the antenna. Moreover, this evaluation assumed that the incoming EM field was either vertically or horizontally polarized. Figure 5 presents the results of this analysis. For both cases, it could be seen that the sensitivity of the Four Season vector antenna was degraded as the frequency increased since the 95th percentile of Δa_{RMS} also rose. This can be explained by two main reasons. As the frequency increases, there are (1) the enhancement of the risk of angular ambiguity (defined in Appendix A-C of [13]), and (2) the decrease of the antenna's efficiency. These can lead to an increase of the estimation errors. Moreover, there is also the emergence of ripples in the radiation patterns as the frequency increases, but this phenomenon was taken into account during the evaluation of the direction-finding performance with the MUSIC algorithm through the calibration process, as detailed in [13]. It can also be noted that the sensitivity required for estimating the direction of arrival of a vertically polarized EM field for a given accuracy is higher than that of a horizontally polarized EM field. This is consistent with the Cramer-Rao bound results depicted in Figures 2 and 3, which showed that the accuracy of the elevation-angle estimation was relatively the same over the entire bandwidth for both polarizations while the azimuth-angle estimation was more accurate at higher frequencies if the incoming EM field was horizontally-polarized. To estimate the required accuracy the direction of arrival of a vertically or horizontally polarized EM field, the incoming power density required at the Four Season vector antenna location (P_{sensi}) is summarized in Table 3. From this study, the theoretical range could be easily derived for an estimation accuracy of 5°, knowing the gain and emitting power of a transmitter.

5. Conclusion

The direction-finding performance of a passive, wideband radiation-pattern reconfigurable vector antenna has been reported in this paper. The vector antenna prototype enables the accurate estimation of the direction of arrival of a vertically or horizontally polarized EM field across the three-dimensional upper half-space and over a 8.2:1 bandwidth (or 1 GHz to 8.2 GHz]) using the measurement of six EM field components and additional radiation patterns in the direction-finding process. Next steps will be focused on evaluating the direction-finding performance of this vector antenna and the benefits of the additional radiation-patterns technique in multipath and multi-source environments.

6. Acknowledgments

We would like to thank the French Defense Agency (Direction Général de l'Armement, DGA) and the Occitanie regional council for the financial support of the thesis of Johan Duplouy in the framework of the AVIAtoR3D project.

7. References

1. T. E. Tuncer and B. Friedlander, *Classical and Modern Direction-of-Arrival Estimation*, New York, Academic Press, 2009.

2. Rohde & Schwarz, "DF antenna ADD253," http://www.rohde-schwarz.com/en/product/add253, visited on June 21, 2018.

3. CRFS, "DF antenna RFeyeArray 300," https://www.crfs.com/all-products/hardware/direction-finders/array-300/, visited on June 21, 2018.

4. TCI, "DF antenna Model 643," https://www.tcibr.com/product/tci-model-643-dual-polarized-vhfuhf-dfand-spectrum-monitoring-antenna/, visited on June 21, 2018.

5. A. Bellion and C. Le Meins, "Directional Multiple-Polarization Wide Band Antenna Network," US Patent US20110133986A1, December 21, 2007.

6. L. Scorrano and L. Dinoi, "Experimental Characterization of a Dual-Polarized Direction Finding Array for VHF-UHF Frequency Bands," European Conference on Antennas and Propagation (EUCAP), March 2017, pp. 1295-1298.

7. P. Gething, *Radio Direction Finding and Superresolution*, London, P. Peregrinus Ltd., 1991.

8. A. Nehorai and E. Paldi, "Vector-Sensor Array Processing for Electromagnetic Source Localization," *IEEE Transactions on Signal Processing*, **42**, 2, February 1994, pp. 376-398.

9. B. Almog, "Compact 3D Direction Finder," Patent EP20120184835, March 20, 2013.

10. A. Musicant, B. Almog, N. Oxenfeld, and R. Shavit, "Vector Sensor Antenna Design for VHF Band," *IEEE Antennas and Wireless Propagation Letters*, **14**, 2015, pp. 1404-1407.

11. J. Lominé, C. Morlaas, C. Imbert, and H. Aubert, "Dual-Band Vector Sensor for Direction of Arrival Estimation of Incoming Electromagnetic Waves," *IEEE Transactions on Antennas and Propagation*, **63**, 8, August 2015, pp. 3662-3671.

12. J. Duplouy, C. Morlaas, H. Aubert, P. Potier, P. Pouliguen, and C. Djoma, "Reconfigurable Grounded Vector Antenna for 3-D Electromagnetic Direction-Finding Applications," *IEEE Antennas and Wireless Propagation Letters*, **17**, 2, February 2018, pp. 197-200.

13. J. Duplouy, C. Morlaas, H. Aubert, P. Potier, and P. Pouliguen," Wideband and Reconfigurable Vector Antenna Using Radiation Pattern Diversity for 3-D Direction-of-Arrival Estimation," *IEEE Transactions on Antennas and Propagation*, **67**, 6, June 2019, pp. 3586-3596.

14. J. Duplouy, C. Morlaas, H. Aubert, P. Potier, and P. Pouliguen, "Wideband Vector Antenna for Dual-Polarized and Three-Dimensional Direction-Finding Applications," *IEEE Antennas and Wireless Propagation Letters*, **18**, 8, August 2019, pp. 1572-1575.

15. R. Schmidt, "Multiple Emitter Location and Signal Parameter Estimation," *IEEE Transactions on Antennas and Propagation*, **34**, 3, March 1986, pp. 276-280.

EIGHTH INTERNATIONAL URSI STUDENT PAPER COMPETITION

Financially Sponsored by the U.S. National Committee for URSI

Chair: Sembiam Rengarajan, California State University, Northridge, CA, USA
Co-Chair: Michael Newkirk, The Johns Hopkins University Applied Physics Laboratory, Laurel, MD, USA

The 1st through 5th Student Paper Prize winners will be awarded a certificate and a check in the amounts of $1500, $1250, $1000, $750, and $500, respectively.

Rules and Guidelines

- The first author and presenter must be a full-time university student.
- The topic of the paper must be related to the field of one of the ten URSI Commissions.
- A full paper, not longer than 10 pages and not shorter than 4 pages in single-column, single-spaced format, meeting the requirements of the SPC paper URSI Template, must be submitted by January 31, 2020.
- Each student is allowed to submit one paper only for the Student Paper Competition.
- The student must also submit either an Extended Abstract or a Summary Paper version of the paper at the same time the full paper is submitted.
- Applicants to the 2020 GASS Student Paper Competition will not be eligible to participate with the same paper.
- Submissions should be made through the URSI GASS 2021 online paper submission system, with the appropriate box (indicating the Student Paper Competition) being checked during the paper submission.
- The full paper will be evaluated within the Competition and will not be published to ensure that there are no subsequent prior-publication issues for those students who wish to submit the work to a journal. This means that the ten-page paper will not be included in the conference proceedings. Only the shortened version will appear in the conference proceedings.
- A paper that is submitted to a journal before submission to the student competition is ineligible. However, students are encouraged to submit their papers to a journal after January 31, 2021.
- A letter from the student's advisor on university letterhead must be uploaded with the full paper. The letter must state that the author is enrolled as a full-time university student in a degree program. If the paper is coauthored, the letter must state that all coauthors played only an advisory role. No other students are permitted as coauthors.
- Submissions must use the following file naming convention, where "Lastnameauthor" text is replaced by the student's surname:
  SPCFullLastnameauthor.pdf
  SPCAbstractLastnameauthor.pdf
  SPCLetteradvisorLastnameauthor.pdf

Ten finalists will be chosen based upon quality, originality and scientific merit. They will receive free tickets to the banquet, where all finalists will be recognized, and prizes will be presented to the five winners.

The finalists will present their papers in a special SPC session at the GASS. They will be judged by a panel consisting of the ten URSI Commission Chairs or their authorized representatives.

The prizes will be awarded based on the clarity of the presentation, adherence to time, accessibility to the broad audience of the ten URSI Commissions, and the ability to answer questions on the work. Prizes will be awarded by check in USD currency.

In Memoriam: Govind Swarup

Prof. Govind Swarup (Figure 1), the doyen of radio astronomy in India and also an internationally acclaimed radio astronomer, breathed his last on September 7, 2020, in Pune, India. He is survived by his wife, Mrs. Bina Swarup; their son, Vipin Swarup; and their daughter, Anju Basu. Prof. Swarup was a legendary figure who will be remembered in the times to come, not just for pioneering radio astronomy in India, but also as one who had big ideas and knew how to make them real.

Figure 1. Govind Swarup (1929–2020).

Govind Swarup was born on March 23, 1929, in Thakurdwara, a small town in the Moradabad district of Uttar Pradesh. His father, Ram Raghuvir Saran, established the first theater in Delhi, the capital of India. His mother, Gunavati Devi, was a housewife who encouraged Govind to read. In 1944, he matriculated with distinction, and then went to Ewing Christian College in Allahabad for his intermediate college studies. These were unforgettable years for him. He learnt to swim at the confluence of the Ganges and Jamuna Rivers, a talent that would come in handy later at Potts Hill reservoir in Sydney, Australia. Leadership qualities in him were evident at this early age, as he became Secretary of the College's Physics Club.

During 1946-1950, Govind completed his BSc and MSc in Physics. Govind was greatly inspired by his teacher, Prof. K. S. Krishnan, who was to later play an important role. During these years, Govind also subscribed to "Harijan," a weekly journal published by Mahatma Gandhi, whom he greatly admired, and he developed a great love for his motherland.

After obtaining his MSc, Govind joined the National Physical Laboratory (NPL), New Delhi. His teacher, K. S. Krishnan, had in the meanwhile become the founder Director of NPL, and Krishnan's research interest was primarily the quantum theory of magnetism: a hot topic in physics at that time. Krishnan asked young Govind to build the necessary electronics to operate at a wavelength of 3 cm ($f = 10$ GHz) in order to study electron-spin resonance. Such high-frequency electronics were very novel at that time. Using some surplus radar sets from WWII, Govind managed to successfully set up the spin-resonance experiment within 18 months: a remarkable achievement.

Krishnan was a person of broad interests. In his pursuit for initiating new and exciting activities at NPL, he attended the Tenth General Assembly of URSI, held at Sydney, Australia, in August 1952. Among other things, he there learnt about the dramatic and remarkable discoveries in the field of radio astronomy being made by Joseph Pawsey and his group at the Radio Physics Division of CSIRO (the Australian equivalent of CSIR in India). This group was comprised of some of the most outstanding experimentalists, such as J. Paul Wild, Wilbur N. Christiansen, John G. Bolton, and Bernard Y. Mills. Upon his return, Krishnan gave a colloquium at NPL in which he described these momentous discoveries. That is how Govind got interested in radio astronomy! Govind was also greatly enthused by Krishnan's announcement that he wanted to start radio astronomy activities at NPL, despite their meager resources. To provide the initial training and a first-hand exposure to radio astronomy, Krishnan put forward Govind's name for a two-year fellowship under the Colombo Plan to work at the Radio Physics Division of CSIRO in Sydney.

In March 1953, Govind and another Indian recipient of the Colombo Plan Fellowship, R. Parthasarathy from the Kodaikanal Observatory in Tamil Nadu, arrived at Sydney to work with J. L. Pawsey and his Radio Physics group. Govind had a remarkable career during his stay of two years and four months, working, in turn, with Christiansen, Wild, Mills, and Bolton. This training had a major lasting influence on Govind's career. He specifically cited the example of his learning the powerful technique of radio interferometry from Christiansen. Govind and Parthsarathy also spent time doing some experimental work themselves under the direction of Pawsey. They worked on a sophisticated telescope designed and built by Christiansen for studying the sun, converting the array of 32 antennas, each roughly 2 m in diameter, so that the operating wavelength would be 60 cm (500 MHz) instead of the 20 cm for which they had originally been designed. This experience was of great value to these young scientists, working independently on hardware construction, observations, data reduction, and the interpretation of the results. It was also during this time that his swimming ability came in handy, when he had an occasion to save Parthasarathy from drowning in the Potts Hill reservoir! As it turned out, Christiansen decided to build a new telescope and in the process, the present 32-element array was to be scrapped. On being requested by Govind, Pawsey agreed to donate those 32 elements of the 1.7 m dishes to NPL, India.

Govind returned to NPL in August 1955, ready to initiate radio-astronomy research, using Christiansen's array

Figure 2. A view of the Ooty Radio Telescope facing due west (courtesy NCRA, Pune).

from Potts Hill as the nucleus around which he planned the initial activities. Roughly during that period, several other persons – Parthasarathy, T. Krishnan, N. V. G. Sarma, M. N. Joshi, and M. R. Kundu – also joined NPL. Dr. Krishnan did thus manage to get a group together and start radio astronomy in NPL. To adapt a phrase from Govind, K. S. Krishnan, who also later became an URSI Vice President, was thus really the foster father for radio astronomy in India. Unfortunately, there was a major delay in getting the 32 dishes from Australia, and hence Govind decided to go to the US for a few years. Gradually, the other group members left too, causing this fledgling group to disperse within a short period.

Before leaving for the US, Govind got married in a conventional arranged Indian marriage. He left for the US with his wife, Bina, in August 1956, to join the Harvard College Observatory. He went to study the dynamic spectra of solar bursts using the 100 MHz to 600 MHz swept-frequency radio spectrograph that had just been installed there. Within a few months, he had made an interesting discovery: the new "Type U" solar radio bursts. In the following year, on the advice of his former mentor, Joseph Pawsey, he decided to join Stanford University and work under the guidance of Prof. R. N. Bracewell, a well-known radio astronomer, in September 1957. Stanford was famous for radio engineering, and Pawsey recommended that if Govind really wanted to return to India, he needed to focus on developing his skills in electronics.

Govind's PhD work mainly involved the setting up of the radio heliograph array on the outskirts of the Stanford University campus. The array was designed to produce daily maps of solar radio-emitting regions at 9.2 cm. During 1956-62, apart from "Type U" bursts, Govind developed a gyro-radiation model for explaining the microwave solar emission, and made studies of the radio emission from the quiet sun. In 1959, in collaboration with K. S. Yang, he developed a round-trip transmission technique for phase measurements. In 1962, he also found the first example of a steep spectrum "bridge" of radio emission between the two radio lobes of the powerful radio galaxy, Cyg-A, using the Stanford Compound Interferometer. Such bridges allow estimates of the age of a radio galaxy.

After obtaining his PhD, Govind joined the faculty of Stanford in January 1961. In the following year, the ex-pat group of young Indian researchers, comprised of Govind Swarup, T. K. Menon, M. R. Kundu, and T. Krishnan, all of whom became well known in their later careers, came together and decided to return to India to set up radio-astronomy experimental facilities. Although they applied to many places in India, it was Prof. Homi Bhabha, founder Director of the Tata Institute of Fundamental Research (TIFR) at Mumbai, who assured them that he was forming a radio-astronomy group and invited them to return. However, it was only Govind who immediately came back and joined TIFR on April 2, 1963. Profs. Kundu and Menon came back later, but did not stay for long.

During the initial period of 1963-1966, two of his former NPL colleagues, N. V. G. Sarma and M. N. Joshi from NPL, and a few other young recruits, such as Vijay Kapahi, J. D. Isloor, Ramesh Sinha, Suresh Damle, Durga Bagri, T. Velusamy V. Balasubramnian, and one of us (SA), joined Govind's group. Under the overall guidance of Govind, the group first set up the Kalyan Radio Telescope (in 1963-1965), using the 32 antennas of the Potts Hill array that had come from Australia. Later, with additional engineering and technical personnel (1965-1970), they went on to build the more ambitious 530 m long and 30 m wide steerable parabolic-cylindrical Ooty Radio Telescope (ORT), situated at Ootacamund (Ooty for short) in south India. The unique and innovative design of this was

Figure 3. A panoramic view of a few of the antennas of the Giant Meterwave Radio Telescope array (courtesy NCRA, Pune).

conceived by Govind. The ORT (Figure 2) was placed on a North-South oriented and suitably inclined hill so as to make its long axis of rotation parallel to that of the Earth, enabling it to track celestial radio sources in hour angle for 9.5 hrs. Using the method of lunar occultation, it provided for the first time high-angular-resolution data (1 arcsec to 10 arcsec) for the linear sizes of more than 1,000 weak radio sources. The evolution of these with redshift (or distance) provided independent evidence for the Big Bang model of the Universe. Occultation observations made using the ORT of the galactic center source, Sgr-A, yielded the first two-dimensional separation of its thermal and non-thermal emissions. Over the years, the ORT has been used for a variety of studies including interplanetary scintillations and the solar wind, pulsars, radio recombination lines, etc., and remains an active and working facility to this date after fifty years: in fact, it is nearing completion of a major new upgrade.

The next project that Govind and his team realized was the Ooty Synthesis Radio Telescope (OSRT, completed in 1984), which extended the ORT into an aperture-synthesis interferometer by adding seven smaller cylindrical antennas at distances up to 4 km. Although relatively short-lived, the OSRT provided valuable experience in building and operating interferometers, which was to prove useful in giving confidence to take the next big step. During the late 1970s, Govind had also tried to build a very large instrument, called the Giant Equatorial Radio Telescope (GERT), in Kenya or Indonesia on the equator, but this could not materialize. As fallouts of his main radio-astronomy activities, Govind also helped in building India's first communication-satellite antenna at Arvi, north of Pune, and helped in building an antenna group in the Electronics Corporation of India Limited (ECIL), Hyderabad. This unit has since grown into a major enterprise for building antennas for many government of India projects. He also worked on solar thermal energy for societal benefit.

During 1984-1996, with several experienced colleagues, Govind conceived and directed the design and construction of the Giant Meterwave Radio Telescope (GMRT). That undoubtedly marked the pinnacle of his career of building iconic, front-line experimental facilities. Consisting of 30 fully steerable parabolic dishes of 45 m diameter that were located in an approximately Y-shaped array of about 25 km in extent in western India, about 80 km from the city of Pune, the GMRT (Figure 3) is a highly versatile and powerful instrument. It is the world's largest radio telescope operating in the frequency range of about 130 MHz to 1430 MHz. Novel concepts developed by Govind and his team made it possible to construct the large GMRT antennas very economically. GMRT also had some other innovations, such as being one of the first radio interferometers to use optical fibers to transport the antenna signals to the central processing station, and to simultaneously support both the interferometry and beam-former modes.

The making of the GMRT was not without its fair share of challenges, ranging from the complexity of the mechanical structure to the radio-frequency electronics and the complex digital-signal-processing systems: the correlator and beamformer electronics. It is to the credit of Govind's team that they were able to successfully tackle these challenges. The completed GMRT was opened to the global community from early 2002 onwards. In the process, Govind attracted a new generation of young members, including one of us (YG), who brought in fresh talent to supplement the experienced team that had grown since the days of the ORT. More recently, this younger generation has carried the torch forward with a significant upgrade of the GMRT that was completed in 2019, and was, most fittingly, inaugurated by Govind on the occasion of his 90th birthday.

Since its commissioning in the late 1990s, the GMRT has been used by astronomers from all over the world to produce many path-breaking discoveries and results. During this period, Govind himself worked with younger colleagues to make observations with the GMRT of the emission and absorption of atomic hydrogen from objects

in the early Universe, and investigated deficiency of radio sources at 327 MHz towards the prominent cold spot of the cosmic microwave background radiation. In the last few years, he had also been working with students to detect and characterize the radio emissions from the planet Venus using GMRT observations.

To summarize, during the past five decades and more, working with different generations of colleagues, Govind made pioneering contributions in the building of front-line radio-astronomy facilities in India. He carried out important research in areas such as solar radio emission, radio galaxies, quasars and cosmology, and interplanetary scintillations and pulsars.

Govind was elected Fellow of the Royal Society, London, and also of all the three major Science Academies of India: Indian National Science Academy, Indian Academy of Sciences, National Academy of Sciences India. He was also elected to the Fellowship of the Third World Academy of Sciences; the Royal Astronomical Society, London; the Astronomical Society of India (President 1975-77); and the International Astronomical Union (IAU) (President, Commission 40 on radio astronomy, 1979-82). He was a member of the Executive Committee of the Inter Union Commission for Frequency Allocation (IUCAF) during 1990-1995; the IAU Working Group for Future Large Scale Facilities (1994-2000); Chair of the Indian National Committee for URSI (1986-88 and 1995-97); URSI Standing Committee for Future General Assemblies (1999-2002); and the editorial boards of many journals.

The list of awards received by Govind is long, and we name here only the prominent awards: Padma Shri, one of the highest civilian awards for distinguished service of the Government of India (1973); S. S. Bhatnagar Award, Council of Scientific and Industrial Research, CSIR, India (1972); Tskolovosky Medal, Federation of Cosmonautics, USSR (1987); The Third World Academy of Sciences Award in Physics (1988); John Howard Dellinger Gold Medal, URSI (1990); 12th Khwarizmi International Award, Iran (1999); Herschel Medal of the Royal Astronomical Society (2006); Grote Reber Medal (2007); Pontifical Academy Award (2011).

There was a great deal of camaraderie in the ORT group headed by Govind, particularly in the first 20 years. Ooty was a small and remote town, perched on the Nilgiri Hills. The group members and their families found great joy in gathering together for all kinds of celebrations. It was in one of those memorable evenings on New Year's eve, when everyone was on a high, that the idea of GMRT took shape after many arguments on what the group should do going forward. The very next day, on the afternoon of January 1, 1984, Govind called some of his colleagues to lay out his dream of building a Y array of many parabolic cylinders, similar to the VLA array that had just become operational. This finally evolved into the concept that became the GMRT.

The site for GMRT was finalized after extensive site surveys by one of us (SA) and others, with the central core located in a quiet rural area of one square kilometer near a village called Khodad (north of the Pune district in western India) in 1985. The Y array did not turn out to be of three straight arms, as these, especially the Western arm, had to be somewhat zigzag. The joke went around saying that since the Western arm was close to a vineyard and their Champagne factory outlet, the people laying out this line had had a glass too many! In reality, of course, the deviations were due to many villages located near the antenna sites, and constraints on availability of land.

Govind was a very persistent and hardworking researcher. In the early days, the graduate students used to say that he gained energy from everyone at the table, while all others became exhausted! As years went by, we saw him motivating everyone he came across without any formalities, and challenging them to do their best. One of us (YG) remembers being challenged, in 1996 (at a fairly early stage in his career), to take up the task of completing the complex digital processing system for the GMRT: one of the critical elements that was holding up the successful completion of the GMRT. Govind was also highly motivated and focused on what he wanted to achieve in the time available. This resulted over the past five decades in the creation of a large school and facilities that are likely to remain strong for a long time.

After his formal retirement, Govind tried to set up an Indian Institute for Science and Technology Education (IISTE) with his friend, the former Vice Chancellor of Pune University, Prof. V. G. Bhide. They almost succeeded, but the government changed in the meanwhile, and the task was taken forward by others into what became the Indian Institute for Science Education Research (IISER) of today.

There was an interesting incident that took place during URSI GA 2005 in Delhi. The venue was Vigyan Bhavan (then the main science conference facility in New Delhi), which had been booked for all the eight days of the meeting. However, just 10 days before the URSI GA meeting, the government of India decided to hold another important meeting there on one of the days, to be addressed by the President of India, Dr. A. P. J. Abdul Kalam. On being persuaded by one of us (SA), Govind agreed to write a telegram directly to Dr. Kalam, requesting him earnestly to shift the venue of his other meeting. A few days later, it was learnt that the President had indeed shifted the venue! Later on, during a private conversation at his presidential residence, Dr. Kalam mentioned that he "of course had to shift the venue because the telegram came from Govind Swarup!"

Govind had thus become a legend in India, and elsewhere, even during his lifetime. In spite of all his achievements and accolades, he continued to be down to earth and extremely approachable throughout his life, to the very end. He leaves behind a tremendous legacy of

Figure 4. Felicitations to Prof. Govind Swarup on his 90th birthday at the URSI Asia Pacific Radio Science Conference 2019 (URSI AP-RASC 2019) (l-r) Amitava Sen Gupta, S. Ananthakrishnan, Makoto Ando, Govind Swarup, R. Paulraj, and Ondrej Santolik (from InRaSS archives).

Figure 5. From the ceremony marking the inauguration of the upgraded GMRT by Govind Swarup on March 21, 2019, in Pune, during a special event in the conference, "The Metrewavelength Sky – II" organized by NCRA (l-r) K. VijayRaghavan, Bina Swarup, Govind Swarup, Anil Kakodkar, Yashwant Gupta, and Sandip Trivedi (courtesy NCRA, Pune).

institutions and individuals who will carry forward his good work.

Last year, the URSI Asia Pacific Radio Science Conference (URSI AP-RASC 2019) was held in New Delhi during Match 12-16, 2019, organized by the Indian Radio Science Society (InRaSS). It was decided to felicitate Govind on his 90th birthday, falling around the same time (Figure 4). He graciously accepted our invitation and traveled to Delhi, despite his extremely frail health condition. He also gave an inspiring keynote address in a special Commission J session that was organized in his honor. The following week, he was felicitated on his 90th birthday by the NCRA, where he most fittingly inaugurated the upgraded GMRT (Figure 5), which will carry on his legacy for many more years to come.

By a fortuitous turn of events, it was just announced that GMRT has been selected for an IEEE Milestone award. It is only the third such award in India, after the discoveries of Sir J. C. Bose and Sir C. V. Raman, the former being one of the first radio scientists and the latter a Nobel Prize winning physicist. Govind Swarup would have been truly proud.

We pay our homage to a great son of India and our heart-felt condolences to his family. May his soul rest in peace.

Amitava Sen Gupta
General Secretary, Indian Radio Science Society (InRaSS)
The NorthCap University, Gurugram, India
(Formerly) Acting Director, CSIR-National Physical Laboratory, New Delhi, India
E-mail: sengupta53@yahoo.com

Subra Ananthakrishnan
President, Indian Radio Science Society (InRaSS)
Pune University, Pune, India
(Formerly) Senior Prof, NCRA-TIFR & Observatory Director, GMRT
E-mail: subra.anan@gmail.com

Yashwant Gupta
Centre Director, National Centre for Radio Astrophysics (NCRA)
Tata Institute of Fundamental Research (TIFR), Pune, India
E-mail: ygupta@ncra.tifr.res.in

Et Cetera

Tayfun Akgül
Istanbul Technical University
Dept. of Electronics and Communications Engineering
Telecommunications Division
80626 Maslak Istanbul, Turkey
Tel: +90 212 285 3605; Fax: +90 212 285 3565
E-mail: tayfunakgul@itu.edu.tr.

XXXIV General Assembly and Scientific Symposium of the International Union of Radio Science

Union Radio Scientifique Internationale

August 28 - September 4, 2021 - Rome, Italy

www.URSI2021.org

Preliminary Call for Papers

The **XXXIV General Assembly and Scientific Symposium** (GASS) of the International Union of Radio Science (URSI, www.ursi.org) will take place in Rome, Italy, from August 28 to September 4, 2021. The scientific programme will be organized around the ten URSI Commissions (see below) and will comprise oral sessions, poster sessions, tutorials, plenary and public lectures, with both invited and contributed papers. In addition, there will be **workshops, short courses, special programmes for young scientists, a student paper competition, programmes for accompanying persons, and an industrial exhibition**. More than 1,500 scientists from more than 50 countries are expected to participate.

Scientists and researchers are invited to submit papers, to be included in the scientific program. Detailed information will be posted on the GASS 2021 web site. **Any topic concerning the scientific domains of URSI Commissions is potentially acceptable**. In addition, papers addressing multidisciplinary aspects will be assigned to inter-Commission sessions.

COVID 19: Given the uncertainty on the vaccine and on the status of the pandemic worldwide in August 2021, the committee is implementing two options for the GASS: a fully physical event, and a hybrid meeting allowing both on-site and remote participation, becoming wholly virtual in case of necessity. Consequently, radioscientists **can confidently submit contributions before the deadline**. Updated information will be posted on the GASS web site in due course.

Paper Submission

All papers should be submitted electronically via the link provided on the GASS 2021 web site, **to be checked prior to submission regarding latest instructions, templates, and sample formats**. Accepted papers presented at GASS 2021 may be submitted for posting on IEEE Xplore, if the author so chooses.

>> Check www.URSI2021.org for regular updates

Important Deadlines:

Paper submission opening: **November 15, 2020**
Paper submission closing: **January 31, 2021**
Notification of acceptance: **March 15, 2021**

URSI Commissions

Commission A: Electromagnetic Metrology
Commission B: Fields and Waves
Commission C: Radiocommunication and Signal Processing Systems
Commission D: Electronics and Photonics
Commission E: Electromagnetic Environment and Interference
Commission F: Wave Propagation and Remote Sensing
Commission G: Ionospheric Radio and Propagation
Commission H: Waves in Plasmas
Commission J: Radio Astronomy
Commission K: Electromagnetics in Biology and Medicine

Young Scientists Program and Student Paper Competition

A limited number of grants are available for young scientists to help them attend the GASS. Information on this program and on the Student Paper Competition will be available on the Web site.

Book Review

George Trichopoulos
Electrical, Computer & Energy Engineering ISTB4 555D
Arizona State University
781 E Terrace Road, Tempe, AZ, 85287 USA
Tel: +1 614 364 2090
E-mail: gtrichop@asu.edu

Open Skies: The National Radio Astronomy Observatory and its impact on US Radio Astronomy by Kenneth I. Kellermann, Ellen N. Bouton, and Sierra S. Brandt, New York, Springer – Open Access, 2020, 670 pp. ISBN 978-3-030-32344-8 (hardcover, €53.49, $59.99), ISBN 978-3-030-32345-5 (ebook, free download).

The view of the starry night sky has since time immemorial filled humanity with awe, wonder, and curiosity. In antiquity, systematic studies were already made of the movement of the sun, moon, and planets: the beginning of the science of astronomy. The introduction of the first telescope by Galileo in 1609 caused a revolution in the observations of the sky, and slowly made astronomy a quantitative science. Over time, ever larger telescopes were built that expanded the study of stars and galaxies immensely. However, all insight gleaned from the observations was restricted to radiation in the one-octave-wide spectral window of visible light, 0.4 μm to 0.8 μm in wavelength.

The detection and interpretation by Karl Jansky in the early 1930s of radiation from the central region of our Galaxy, the Milky way, at a radio wavelength of 15 m, opened a completely new window through which the cosmos could be observed. It was so out of the ordinary that professional astronomers essentially ignored it. However, an electrical engineer and radio ham, Grote Reber, built a 10 m-diameter parabolic reflector in his backyard and started to systematically observe the sky at a wavelength of 2 m. His results were published during WWII, and drew the attention of astronomer Jan Oort at Leiden Observatory in the Netherlands. During the war, radar engineers in England and Australia had noticed interfering radiation from the sun, and in both countries the available equipment was quickly turned to the sky at the end of the war. The exciting observations in the early years, including the detection of the 21 cm spectral line of atomic hydrogen in 1951, led to the planning of large radio telescopes in these countries.

In the early 1950s, large Yagi arrays, operating at short meter wavelengths, were operational at Cambridge University in the UK and CSIRO in Sydney, Australia. At Dwingeloo in the Netherlands, a 25 m-diameter parabolic telescope came into operation in 1956, and the huge 76 m-diameter antenna in Jodrell Bank, UK, followed in 1957. In Australia, a 64 m telescope was completed in 1961. Compared to these initiatives, the development of radio astronomy in the USA was limited to a few universities and government laboratories, most of which were devoid of astronomers. A notable exception was Harvard University, where astronomy professor Bart Bok educated the first group of American radio astronomers with a small 7.5 m antenna, and from 1956 with an 18 m telescope concentrating on observations of the 21 cm hydrogen line.

Concern about the lack of competitive observing possibilities in the USA led to discussions in the mid-fifties for the establishment of a national facility for radio astronomy under the aegis of the recently established National Science Foundation (NSF). This resulted in the creation of the National Radio Astronomy Observatory (NRAO), located in Green Bank, in a remote Appalachian valley of West Virginia, in the fall of 1957.

The story of NRAO is comprehensively told in the book Open Skies. The title refers to the policy for the use of the observatory: "all qualified scientists without regard of institutional affiliation would have access to the facility...." This policy has been followed by NRAO ever since, and has been adopted by most radio, and somewhat later, optical, observatories throughout the world. The three authors bring their specific capacities to the text. The senior author, Kenneth Kellermann, came to NRAO in 1965 at the time where the observatory had gotten up to speed. Ellen Bouton has been librarian and then archivist since 1975, creating the extensive archive that is reflected in the hundreds of detailed references and notes dotted into the text. Historian of astronomy Sierra Brandt contributed to the archives and the wider historical aspects of the subject.

Rather than telling a strictly chronological tale, the book is divided into eleven chapters that each describe the major projects or areas of NRAO's activities over time. This has the advantage that these can be dealt with coherently and completely.

Chapters 1 and 2 introduce the birth and early development of radio astronomy, beginning with Jansky's initial discovery through the early efforts worldwide up to the mid-1950s, where radio observatories in the UK, Australia, the Netherlands, and other countries had shown the rich reservoir of astronomical science that could be addressed at radio wavelengths. This period has been covered in detail by W. Sullivan in Cosmic Noise, reviewed in the Radio Science Bulletin No. 338, September 2011.

Chapter 3 is devoted to the discussions, decisions, and planning of a national radio-astronomy facility supported by the NSF that would provide instruments of high caliber to all qualified astronomers. Over 75 pages with 220 footnotes we read a detailed account of the birth pangs of NRAO. The NSF, as federal sponsor of the observatory chose Associated Universities Incorporated (AUI) as the managing organization for the formation and later operation of the observatory. AUI had been established in 1947 by a number of Northeastern universities to manage the nuclear physics laboratory at Brookhaven on Long Island. Both NSF and AUI had their own governing boards and advisory committees, each of which had leaders with big egos and committees of expert advisers. For more than two years, during numerous meetings, the organization of the national observatory was established and a plan for the observatory equipment was agreed. It is fascinating to follow the proceedings under the influence of strong personalities, overly confident advisers, especially optical astronomers, and administrators. In 1956, NRAO was established with a 140-ft equatorially mounted radio telescope as its piece de résistance that would, however, take a decade to be realized.

The first ten years of NRAO are treated in the aptly titled Chapter 4: "Growing Pains." The remote site in Green Bank, West Virginia, was not a very attractive place to live for scientists and engineers, but a handful of fresh PhDs from Bart Bok at Harvard took up the challenge. The search for a director took several years, and ended in mid-1959 with the appointment of Otto Struve, a highly esteemed optical astronomer. After two years, he returned to full research and his chosen successor, Joe Pawsey from Australia, died before he could assume his position. Dave Heeschen, the first staff astronomer, was appointed director in 1962 and remained in this position for sixteen years.

[In the spring of 1963, close to finishing my studies in physics at the Technical University of Delft in the Netherlands, I had applied for a position with the Dutch radio astronomy group at Leiden Observatory. I was eager to become a radio astronomer, but there was no position available. Fortuitously, Dave Heeschen visited Leiden, and a meeting between Professor Oort, Heeschen, and myself was arranged. After a half-hour interview, Heeschen offered me a research assistant position in Green Bank for three years. The three years from 1963-1966 among the highly international staff and the expansion of the telescopes in Green Bank were an ideal introduction to my later career.]

Under Heeschen's leadership and vision, NRAO developed into the major radio observatory in the USA and eventually the world. The construction and operation of the first telescopes are presented in quite some detail, in particular the 140-ft telescope that evolved into a nightmare until it finally came on air in 1965 at triple the original contract price and a delay of five years. As Heeschen remarked at its dedication, "The 140 foot is a classic example of how not to design and build a telescope." Due to its first-class receiver systems and efficient and user friendly operation it was the most effective radio telescope for quite a number of years. While waiting for the delayed 140-ft, deputy director John Findlay organized the design and construction of a 300-ft large transit telescope in less than 18 months (1962) and for less than one million dollars, and two years later the first 85-ft antenna was extended by a second one to form the Green Bank Interferometer. From 1965 onwards, NRAO was a productive radio observatory, providing data to a good part of the world's radio astronomers. Just in this period, the growing scientific staff with their families became dissatisfied with the loneliness and simplicity of Green Bank, resulting in a relocation of NRAO's headquarters to the campus of the University of Virginia in Charlottesville.

As an intermezzo, a short chapter is devoted to Frank Drake's Project Ozma, the first search for signals from extraterrestrial civilizations. The growing size and maturity of NRAO, along with the relocation to Charlottesville, caused significant internal reorganizations that were handled by Dave Heeschen with his usual no-nonsense approach. His last word at a committee or staff meeting was invariably "the bar is open." This is also the title of Chapter 6, in which the organizational changes are presented and aspects of cooperation with and competition from other US and foreign radio observatories are discussed.

The Green Bank Interferometer was built to enable scientific and technical staff to gain experience in interferometry. Already in the early sixties, internal discussions pointed to the need for a telescope that could produce radio pictures of extended objects with an angular resolution comparable to optical instruments, i.e., one arc-second. In 1967, NRAO submitted a proposal for the design and construction of a "Very Large Array" (VLA) that would provide such a resolution at the best possible sensitivity. The story of the VLA is told in Chapter 7. Following a lengthy and heated struggle with Caltech over a competing proposal, the VLA construction was executed within schedule and budget. It started full operation in 1980, and has since then been the most sensitive and versatile radio telescope in the world.

Observations with interferometers had shown that many objects contained structure in their brightness on angular scales well below 1 arcsec. To resolve these would require baselines of thousands of kilometers, pointing to the need for interferometric observations with stations that did not have a physical signal connection between

them. In 1967, a group in Canada and another at NRAO set up experiments to record astronomical data along with accurate time stamps on magnetic tape, and to combine the recordings from two widely separated antennas in a special correlator or computer. This technique is called VLBI (Very long Baseline Interferometry) and has been very successful. Chapter 8 describes these efforts and the construction of yet another NRAO telescope, the VLBA (Very Large Baseline Array), which comprises 10 antennas of 25 m diameter on locations from Hawaii to the Virgin Islands, with eight spread over the continental USA. There exist additional VLBI networks of independent telescopes all over the world that schedule observations at specific periods.

In the original proposal for NRAO, the main instrument was a very large parabolic reflector with a diameter of 400 – and preferably 600 – feet. The delays in the 140-ft project caused the stopgap construction of the 300-ft transit telescope, but initially no effort was spent in designing the very large antenna. Instead, NRAO observed the work by the US Naval Research Laboratory (NRL) to construct a fully steerable antenna of 600-ft diameter in Sugar Grove, located in a neighboring valley from Green Bank. This project ended early in a great fiasco, as vividly described in Chapter 9. NRAO took the approach of slowly and thoroughly building in-house design capabilities that worked under the heading Largest Feasible Steerable Telescope (LFST). At the center of activity stood the application of the principle of homologous deformation (shortly called homology) that was developed by NRAO staff member Sebastian von Hoerner. A homologous reflector retains a parabolic shape under varying gravitational forces, and allows a significant lighter structure for a given precision. A prime example is the Effelsberg 100-m radio telescope in Germany. The LFST group presented designs for a 100-m telescope (shortest wavelength 1 cm), and 65-m (3.5 mm) and 25 m (1 mm) telescopes. Only the 25 m was submitted for funding, but was eventually dropped in favor of the VLBA. With the VLA and VLBA in full operation, NRAO did not propose a very large dish.

In November 1988, the 300-ft transit telescope in Green Bank collapsed. Unexpectedly, the powerful US Senator Byrd decided that this telescope in his home state should be replaced with at least an equivalent instrument. The fascinating story of the birth, design, and construction of the Green Bank Telescope, a 100-m-diameter clear-aperture antenna, comprises the main part of Chapter 9. Again, NRAO provided an in-house design. In the execution of the project, there were several similarities to the wrong decisions made in the 140-ft and Sugar Grove 600-ft projects. The GBT was finally delivered in 2000, with a delay of several years and a significant cost overrun, most of it absorbed by the contractor. To reach the original specification, many additional measures in the area of metrology and structural engineering had to be taken. These activities are still ongoing. In the meantime, as in the case of the 140-ft, the first-class receiver systems and a flexible operation have kept Green Bank on the map as a powerful radio observatory, with the GBT functioning as specified.

Chapter 10 is devoted to NRAO's activities in the millimeter-wavelength regime. Already in 1963, Frank Low made first observations in Green Bank with a bolometer of his design on a five-foot searchlight reflector. Soon afterwards, the observatory submitted a proposal to the NSF for the construction of a dedicated mm-wavelength telescope of 36 ft diameter and a reflector precision of 0.05 mm, suitable for observations at 1 mm. Because atmospheric water vapor strongly absorbs such short-wavelength radiation, it was decided to locate the telescope at about 2000 m altitude at the Kitt Peak optical observatory near Tucson, AZ. As in the case of the 140-ft, the contractor was not up to the difficult task, and the telescope came into operation only in 1968, with a surface precision a factor two worse than the specification. Once Robert Wilson and Arno Penzias detected carbon-monoxide at 2.6 mm with the telescope and other molecules were rapidly found, the telescope became the most heavily subscribed instrument of NRAO. This led to initiatives within NRAO in the mid-1970s to build a truly powerful mm-telescope of 25 m diameter. Its design was taken up in the LFST group, but the proposal was not successful in becoming a first priority project at the NSF and the astronomy community. Under pressure from large mm-telescope projects abroad, notably in Japan, Germany, France, and the UK, the 36-ft was upgraded with a new reflector of 12 m diameter in 1983. In the same year, the 25 m project fell by the wayside, and the USA was not in the forefront of mm astronomy. Encouraged and supported by the university community, NRAO embarked on the design of a "millimeter wavelength VLA." In 1990, a proposal for the "MilliMeter Array" (MMA) was submitted to the NSF. The MMA consisted of 40 dish antennas of 8 m diameter that could be moved to form a variable baseline synthesis array at short mm-wavelengths. Only in 1995 did NRAO receive sizeable funding for the detailed design and construction of the MMA. Eventually, in about 1997, it became clear that Japan and Europe were also developing plans for a large mm-array. Both were aiming to site the arrays at a high plateau in the Atacama Desert of Northern Chile, a site that was by now also favored by NRAO. Discussions about collaboration and perhaps combining funds for a joint superior telescope led to an MOU between NSF and ESO (European Southern Observatory) in June 1999 for the joint development and design of a large array, to be named Atacama Large Millimeter Array (ALMA).

[It was in the context of the evaluation of two ALMA prototype antennas that I joined NRAO as a guest for the last two years before retirement. This time, it was not the loneliness of the lush valley at Green Bank, but that of the dry and empty vastness of the VLA site in New Mexico that constituted the working environment. In hindsight, both were worth their while.]

A few years later, Japan joined the collaboration at a level of 25%, and delivered so-called enhancements to the original ALMA layout of 50 highly precise dishes of 12 m diameter. Science observations started in late 2011, and the official dedication took place in March 2013. ALMA is the biggest astronomical project ever realized, and an example

of good international scientific collaboration, including its pitfalls and successes.

The last chapter, "NRAO and Radio Astronomy in the Twenty First Century," presents a discussion of the relations within the US with university observatories and optical astronomers. Despite the successful global collaboration in ALMA and in VLBI, NRAO and the US community decided to refrain from participation in the "Square Kilometre Array" (SKA), a gigantic radio telescope project with global participation that will be deployed in Southern Africa and Western Australia. It is an unsurprising outcome of the attitude over the lifetime of the NRAO in favor of "go it alone." This has resulted in a proposal for the "next generation VLA" (ngVLA), a telescope that is presented as bridging the gap between ALMA and the SKA.

Open Skies tells the "complete, unabridged saga" of NRAO. The amount of detail – in particular, of the political, administrative, and scientific discussions – is exhaustive, with hundreds of pointers to the original documents that are all accessible at NRAO. Occasionally, the reader gets tired or bored. However, often the authors insert little specs of humor, both critical and uplifting, that helps keep one attuned. Here are a few examples. Grote Reber, on the 140 foot project: "If such an affair had happened during the days of Elizabeth I, there would have been some public hangings." Dave Heeschen, on receiving the first money for the VLA construction in 1973: "We've wanted this thing so long, and now we are getting it from a crook" (US President Richard Nixon). Frank Drake, in the town of Cass, asking someone, "Do you know where the liquor store is?" and receiving an answer, "Yup, but I ain't gonna tell ya."

The reader can get all this for free, because the book is published as open access, which means that it is downloadable, per individual chapter if you wish, from the Springer Web site: https://www.springer.com/gp/book/9783030323448. A printed version can be had for about 55 dollars/euros.

Jacob Baars
Max-Planck-Institut für Radioastronomie (retired)
Bonn, Germany
E-mail: jacobbaars@arcor.de

INTERNATIONAL UNION OF RADIO SCIENCE
UNION RADIO-SCIENTIFIQUE INTERNATIONALE
info@ursi.org www.ursi.org

URSI YOUNG SCIENTISTS AWARDS

A limited number of awards are available to assist young scientists from both developed and developing countries to attend the General Assembly and Scientific Symposium of URSI in Rome, 28 August – 4 September 2021.

To qualify for an award, the applicant:

1. must be less than 35 years old on September 1, 2021;
2. should have a paper, of which he or she is the principal author, submitted and accepted for oral or poster presentation at a regular session of the General Assembly and Scientific Symposium.

Applicants should also be interested in promoting contacts between developed and developing countries. Applicants from all over the world are welcome, including from regions that do not (yet) belong to URSI. All successful applicants are expected to fully participate in the scientific activities of the General Assembly and Scientific Symposium. They will receive free registration, and in case of physical presence on site, financial support for board and lodging at the General Assembly and Scientific Symposium. Limited funds will also be available as a contribution to the travel costs of young scientists from developing countries, but this will also strongly depend on the situation with respect to the COVID-19 situation and the general format of the GASS 2021.

All Young Scientist applicants must submit a Summary Paper (2 to 4 pages) meeting the requirements of the Summary Paper Template, together with a CV and a list of publications in PDF format. The Summary Papers will be submitted to IEEE Xplore unless the author opts out. Please note that applicants to the 2020 GASS Young Scientist Program will not be eligible to participate with the same paper.

The application needs to be done electronically by going to the same Web site used for the submission of abstracts/papers via http://www.ursi2021.org/. After entering the author and submission details, authors will be asked if they want to apply for the Young Scientist Award. If they check the box "Yes," additional questions will pop up for them to answer. Submissions must use the following file naming convention, where "Lastnameauthor" text is replaced by the student's surname and "Firstnameauthor" text is replaced by the student's first name.:

- YSASummaryLastnameauthorFirstnameauthor.pdf
- YSACVLastnameauthorFirstnameauthor.pdf
- YSAPubListLastnameauthorFirstnameauthor.pdf

The deadline for paper submission is **31 January 2021**.

Applications will be assessed by the URSI Young Scientist Committee, taking account of the national ranking of the application and the technical evaluation of the Summary Paper by the relevant URSI Commission. Awards will be announced on 1 May 2021 on the URSI Web site.

For more information about URSI, the General Assembly and Scientific Symposium, and the activities of URSI Commissions, please look at the URSI Web site at: http://www.ursi.org/ and the GASS 2021 Web site at http://www.ursi2021.org/. We will also post updates on our Twitter account @URSI_Radio and on our Facebook page @internationalunionofradioscience.

If you need more information concerning the Young Scientist Program, please contact: **URSI Secretariat, E-mail: ingeursi@ugent.be**

Commission E
(Electromagnetic Environment and Interference)

Announcement of a Commission E corner in the Radio Science Bulletin

Commission E announces a corner in the Radio Science Bulletin (RSB) showcasing latest research, news, updates and announcements from different geographical regions. Concise reports, editorially in line with the RSB and subsequent to a review process, would appear in this corner. The details along with an approximate length (maximum) is provided below.

- Updates on activities and latest developments from different geographical regions: Up to 2 paragraphs
- Short report or concise article on recent research and development (novel ideas, implementation, results) – 1 page including figures and plot
- Activities supporting the URSI flagship conferences, collaborations, Commission E promotion-related information – 1 page

The scope of URSI Commission-E includes (but is not restricted to) the following topics:

- Terrestrial and planetary noise of natural origin, seismic associated electromagnetic fields
- Man-made electromagnetic environment
- The composite noise environment
- The effects of noise on system performance
- The effects of natural and intentional emissions on equipment performance
- The scientific basis of noise and interference control, electromagnetic compatibility
- Spectrum management

Contributions can be sent to the following members:

Articles on recent research and development - Kaushal Buch (kdbuch@gmrt.ncra.tifr.res.in)

Updates from different geographical regions - Virginie Deniau (virginie.deniau@ifsttar.fr)

Conferences, collaborations, Comm-E related - Frank Gronwald (frank.gronwald@uni-siegen.de)

Historical Corner Column

Giuseppe Pelosi
Department of Information Engineering
University of Florence
Via di S. Marta, 3, 50139 Florence, Italy
E-mail: giuseppe.pelosi@unifi.it

Foreword

For this issue, I chose to ask a colleague for a historical paper relative to biomedical applications, and hence within URSI Commission K: Electromagnetics in Biology and Medicine. However, two papers were submitted.

The first paper, titled "The Electrostatic Foundation of the Electrocardiogram," outlines the early development of electrocardiography. This is a fundamental diagnostic instrument, widely used nowadays. The first working prototype was presented in 1902 by Willem Einthoven (Figure 1a), but the origin of the instrument dates back to the discovery of the electrical phenomena linked to the heart by the Italian, Carlo Matteucci.

The second paper, titled "An Unexpected Mossotti: His Formula at the Basis of Dielectrophoresis in Modern Molecular Biology," returns to a scientist already the matter of a couple of papers on this *Bulletin*, but who is now viewed in terms of the modern applications of his theory to an important biomedical analysis technique, that is, dielectrophoresis (Figure 1b)

Figure 1a. Willem Einthoven (1860-1927), who received the Nobel Prize in 1924 in Physiology and Medicine, for his discovery of the mechanism of the electrocardiogram.

Picture removed due to copyright restrictions

Picture removed due to copyright restrictions

Figure 1b. Arne Wilhelm Kaurin Tiselius (1902-1971), who received the Nobel Prize in Chemistry in 1948, for his research on electrophoresis, which was the foundation for the later discovery of dielectrophoresis.

The Electrostatic Foundation of the Electrocardiogram

Stefano Maddio

Department of Information Engineering
University of Florence
Via di S. Marta, 3 – 50139
Florence, Italy
E-mail: stefano.maddio@unifi.it

Abstract

The electrocardiogram, or ECG, is the first diagnostic test for evaluating the health of the heart. Safe, fast, and noninvasive, it does not require previous preparation. The ECG is the graphic recording of the electrical activity of the heart and the variations that occur during cardiac contraction (systole) and relaxation (diastole) of the atria and ventricles during its operation, collected by means of electrodes placed above the body. It was introduced by Willem Einthoven and Étienne-Jules Marey at the beginning of the 20th century.

While it was already known since early in the 19th century that every contraction of the heart was due to an electrical activity, it was only with Einthoven and Marey that the electrical activity of the heart was recorded in a quantitative manner, using a modified string galvanometer. Many of the conventions established by Einthoven hold still in the modern era, and form the basis for interpreting many aspects of the modern ECG. In particular, the Einthoven Triangle, which is an imaginary inverted equilateral triangle with the heart at the center, is still the core of the electrode arrangement.

LEZIONI
SUI
FENOMENI FISICO-CHIMICI
DEI
CORPI VIVENTI
DEL CAV. PROFESSOR
CARLO MATTEUCCI
SECONDA EDIZIONE
CON MOLTE CORREZIONI ED AGGIUNTE
PISA 1846

Figure 1. First page and illustration of a "pile" of pigeon hearts from the second edition (in Italian) [4].

The electrocardiogram is a simple, safe, noninvasive medical exam used in countless clinical contexts. In its modern version, it allows not only the measurement of the heartbeat frequency, but also measures the dimensions and position of the heart chambers and spots possible myocardium faults or nerve faults, as well as verifying the correct functioning of a pacemaker.

That the heart had an electric behavior was discovered early in the 19th century. That muscles had a reaction to electric currents was discovered even earlier, in 1790, by Luigi Galvani (1737-1798). Indeed, the movements in a frog leg as a current was applied (in an earlier experiment just from electrostatic machines; then, thanks to Alessandro Volta (1745-1827), with the battery, invented 1799) was even used as a crude galvanometer. The discovery of the magnetic effects of the electric currents by Hans Christian Oersted (1777-1851) and the later refinement of the galvanometer by Leopoldo Nobili (1784-1835) most opportunely ended this slaughtering of frogs.

Nobili himself studied bioelectricity, with frogs and torpedoes [electric rays], to test his galvanometers. After his death in Florence, the experiments were taken over by Carlo Matteucci (1811-1868), who was invited in Florence in 1834 by Nobili himself. Matteucci studied torpedoes' electrical organs and the production of electricity from damaged or stressed muscles, again in particular those of frogs. Matteucci was an eminent Italian scientist who befriended Michael Faraday and who was awarded the Copley Medal of the Royal Society of London for his studies on animal electricity. Matteucci was visited by James Clerk Maxwell on the occasion of the journey of Maxwell to Florence [1].

Matteucci showed that electricity passed through the nerves, and not through the body, and that muscular action was the source of electricity. He was the first to observe the electric effect on a frog's heart. He was also the first to observe that the beating heart of a vivisected frog was a source of electrical stimuli he could measure [2], even if extremely faint [3]:

> J'ai tout à fait enlevé le coeur à des grenouilles, j'en ai fait couler le sang, et alors je les ai préparées de la manière

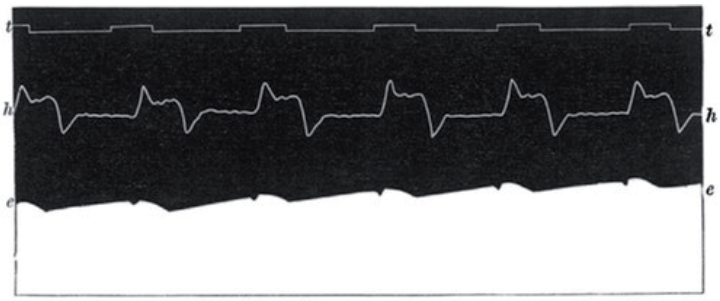

Figure 2. A comparison of the electrical cardiograph and mechanical cardiograph proposed by Waller (from [5]).

ordinaire. Les contractions propres étaient très-faibles dans ces grenouilles, et quelquefois manquaient tout à fait; aussi les signes du courant propre su galvanomètre sont dans ces grenouilles sensiblement diminués.

I have then taken the heart from some frogs, eliminated the blood, and prepared them as usual. The natural contractions were very faint in these frogs, and sometimes absent; and at the same time, the natural currents, measured by the galvanometer were much fainter in these frogs.

Matteucci built a sort of generator via stressed muscles, and in particular pigeon hearts (Figure 1 and [4]). He clearly recognized the relevance of the electric forces on a living heart. The first true electrocardiogram was due to Augustus Desiré Waller (1856-1865), who published in 1887 a comparison between an electrical measurement (on a man, with two electrodes on his chest, one on the front and one on the back – line e in Figure 2) and an ordinary mechanical cardiograph (line h in Figure 2) [5].

However, a true comprehension of the heart's electric functioning initiated with Willem Einthoven, who is universally regarded as the father of the electrocardiogram. Einthoven was born on 21 May 1860, in Java, in the former Dutch East Indies (now Indonesia). He received his medical degree from the University of Utrecht in 1885. In 1886, he was made a professor of physiology at the University of Leiden, in Holland, where he taught until his death in 1927 [6].

His curiosity brought him to study the mechanism regulating the heart, with a seminal 1902 paper [7]. In this paper, there is one of the first recordings of the electrocardiographic measurement made by Einthoven (Figure 3). In a famous paper published in 1906, he wrote [8]:

> We should first endeavor to better understand the working of the heart in all its details, and the cause of a large variety of abnormalities. This will enable us... to give relief to the suffering of our patients.

His research on cardiovascular activity lead to the invention of the first electrocardiogram. This astonishing discovery earned him the Nobel Prize in 1924 in Physiology and Medicine. The Nobel Prize citation was "for the discovery of the mechanism of the electrocardiogram" [9].

The principle on which the electrocardiogram is based is simple. It is known that the bioelectric potential of the

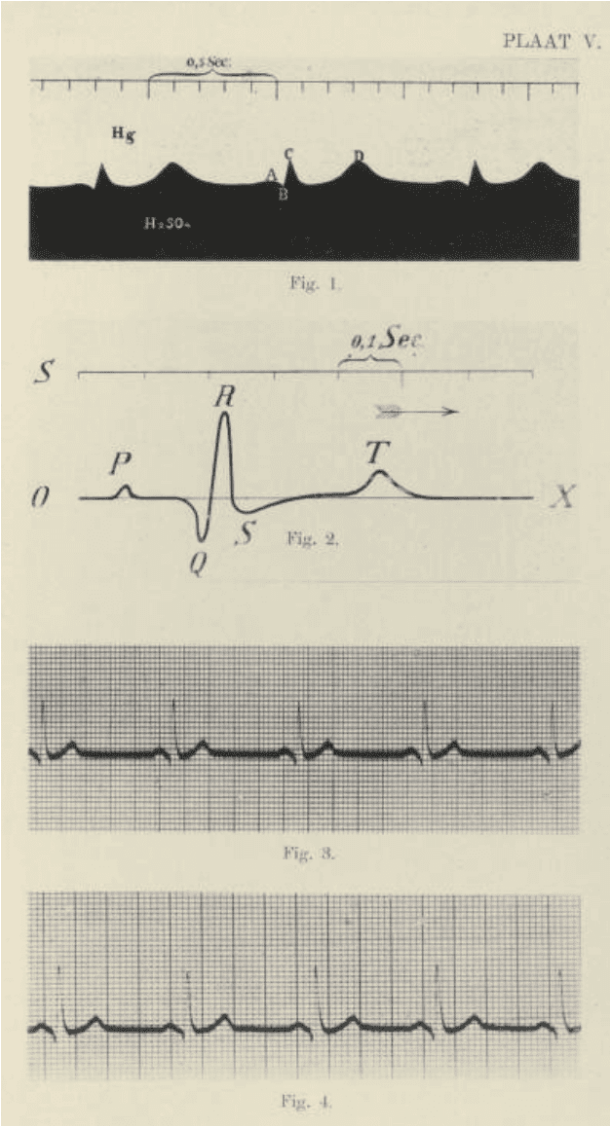

Figure 3. The electrocardiographic measurement by Einthoven (from [7]).

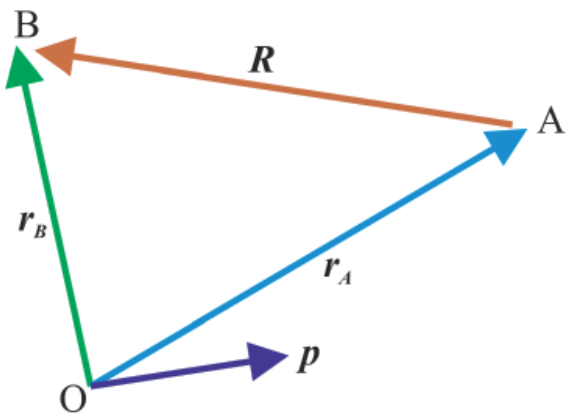

Figure 4a. A representation of the projection of the potential, p, over the vector difference $\mathbf{r}_B - \mathbf{r}_A$.

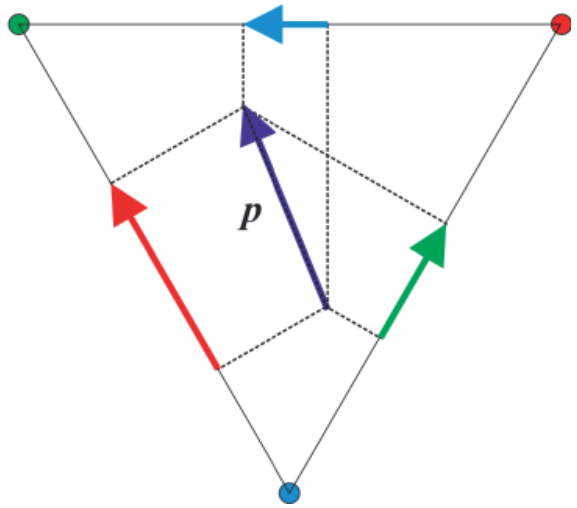

Figure 4b. A projection of the cardiac vector, p, on the sides of the triangle.

heart is generated by the activity of the myocardial cells. Indeed, the course of the action potential varies according to the muscular activity of the heart. The activity of myocardial cells can be divided into four phases:

1. Depolarization: an external electrical stimulus causes the voltage to rise across the cell membrane.

2. Overshoot: the increase in voltage across the cell membrane induces the exchange of sodium and potassium ions. Depolarization reaches a maximum value.

3. Re-polarization: having reached the maximum, the tension across the membrane undergoes a sudden reduction.

4. Hyper-polarization: the violent re-polarization phase causes a hyper-polarization of the membrane, the voltage of which drops temporarily below the equilibrium value, and then settles down.

From the electrical point of view, these changes are slow, and therefore the heart can be treated with an electrostatic approach. In this context, the electrical activity that characterizes the heart, as with any complex form of charge distribution, can be developed with a multipolar development:

$$\phi = \sum \phi_i = \phi_m + \phi_d + \ldots$$

where

$$\phi_m = \frac{1}{4\pi\varepsilon}\frac{q}{r},$$

$$\phi_d = \frac{1}{4\pi\varepsilon}\frac{p\cos\theta}{r^2} = \frac{1}{4\pi\varepsilon}\frac{\mathbf{p}\cdot\mathbf{r}}{r^3},$$

where the dielectric constant, ε, takes account of the human body characteristics. This is a rough model, but it is enough for describing the cardiac action from the phenomenological point of view. In this model, the behavior of the charge source can be approximated with the source of the first nonzero multipole in $\sum \phi_i$. In the case of the heart, it is the dipolar moment ϕ_d.

Einthoven therefore hypothesized that he could schematize cardiac activity as that of a dipole, which, as the activity of muscle activation varied, "*modify its orientation and strength*" over time. Based on this assumption, the instantaneous potential due to the heart can be described with the very simple model of a **p** dipole moment that rotates and over time, the so-called *cardiac vector*.

The electrocardiograph records the differences in electric potential due to the cardiac vector, **p**, between two suitably chosen points A and B. By applying the formula of the dipole potential to points A and B, making sure that the distances are similar, that is, $r_A \approx r_B \approx r$, the potential difference is trivially given by

$$\phi_A - \phi_B = \frac{1}{4\pi\varepsilon}\frac{\mathbf{p}\cdot\mathbf{r}_A}{r_A^3} - \frac{1}{4\pi\varepsilon}\frac{\mathbf{p}\cdot\mathbf{r}_B}{r_B^3} = \frac{1}{4\pi\varepsilon}\frac{\mathbf{p}\cdot\mathbf{R}}{r^3},$$

where **R** is the vector difference $\mathbf{r}_A - \mathbf{r}_B$.

We now observe that the scalar product $\mathbf{p}\cdot\mathbf{R}$ means projecting the vector p onto the vector R, and therefore $\phi_A - \phi_B$ is proportional to the component of p along the line joining points A and B (Figure 4a).

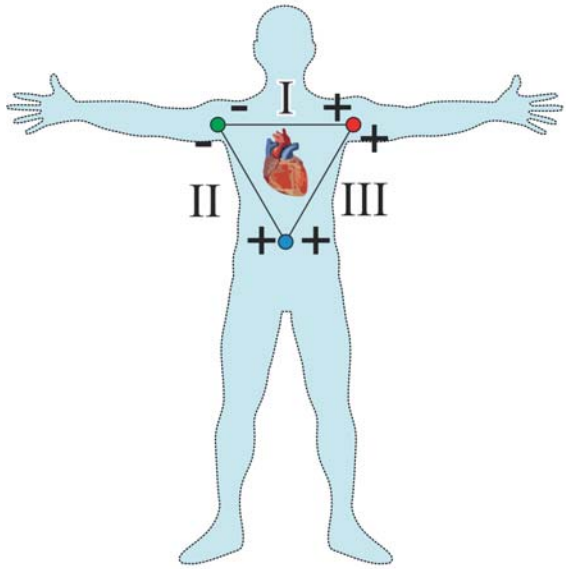

Figure 5a. Einthoven's triangle realized by the ends of the upper limbs.

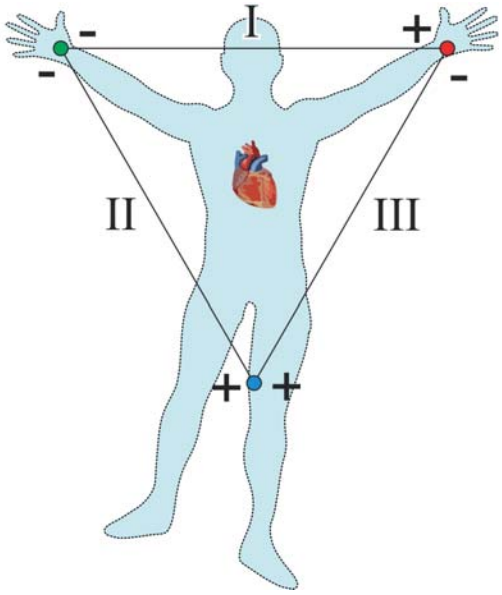

Figure 5b. Einthoven's triangle realized by one point in the left leg.

With three measures of the electric potential, corresponding to the projections of p on at least two linearly independent axes, it is therefore possible to reconstruct the total cardiac electric dipole moment vector in a two-dimensional space and study its variation in modulus, direction, and direction in time, (Figure 4b).

Einthoven's triangle is thus an imaginary formation of three limb leads formed by the two shoulders and the pubis. Another possible configuration consists of the two hands and the left leg as the position of the leads. In either case, the shapes form an inverted equilateral triangle with the heart at the center (Figure 5). If the triangle is equilateral, the same factor scales the dipole potential, hence the dipole behavior is successfully recorded without distortion. Indeed, the expression $\mathbf{R}/r^3$, which multiplies the cardiac vector **p**, is merely a scale factor.

With reference to Figure 5, by convention, "Lead I" is the configuration that measures the potential difference between the two arms, with the positive electrode on the left arm and the negative electrode on the right arm. In the "Lead II" configuration, the positive electrode is on the left leg and the negative electrode is on the right arm. Finally, "Lead III" has the positive electrode on the left leg and the negative electrode on the left arm.

With reference to Figure 6, the positive electrode for Lead I is at zero degrees relative to the heart, while the positive electrode for Lead II and the positive electrode for Lead III are +60° and +120° relative to the heart, respectively.

Einthoven used the measured points identified by the vertices of the triangle as the contacts for his string galvanometer. The actual tracks recorded by this device were confused and affected by noise, but nevertheless demonstrated the electrical behavior of the heart and the periodic electrical activity. In Figure 7, a pictorial representation of the cardiac activity is compared to the familiar trace of an ECG taken with standard axial reference.

It was Einthoven who assigned the letters of the alphabet "P, Q, R, S, T" to the various parts of the ECG traces. According to Snellen, Einthoven's official biographer [10], "The primary reason for changing the letters from ABCD to PQRST was to eliminate confusion.... I believe that Einthoven recognized, perhaps as an afterthought, that by choosing PQRST he allowed space to add letters before P and after T."

Indeed, the motion of the cardiac vector is more complex than the simple two-dimensional path estimated by Einthoven and his colleagues. The most important criticism is the fact that the motion of the heart's dipole is not constrained to a two-dimensional plane, but it describes a more-complex path.

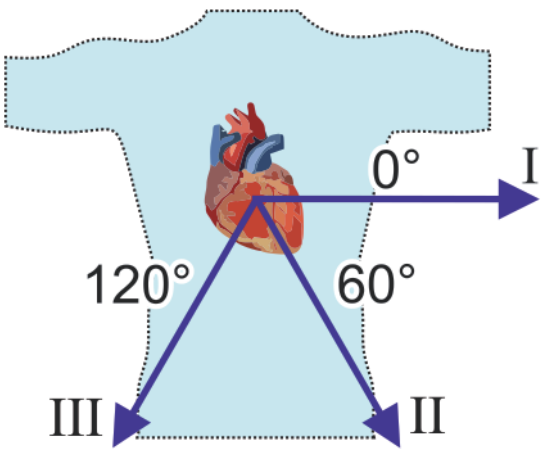

Figure 6. The axial reference system.

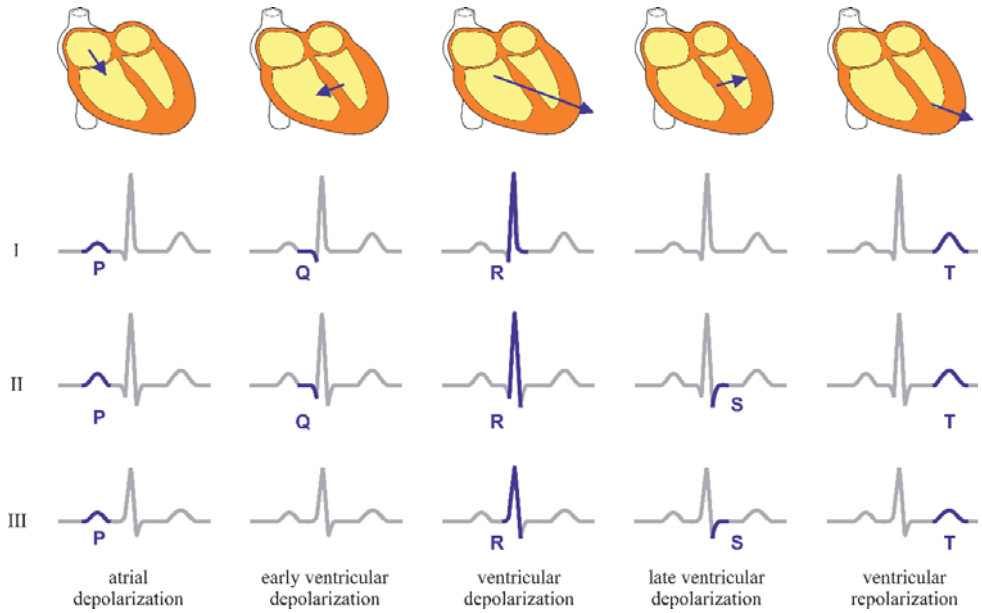

Figure 7. A characteristic cardiac activation sequence and corresponding electrocardiographic traces.

The modern electrocardiographic analysis is in fact based on more than three electrodes, and their placement is also dictated by other considerations. For example, the precordial leads are chest leads placed on the sternum to improve the capability of the ECG to sample the three-dimensional motion of the cardiac vector.

Further enhancements in the study of the heart demonstrated that a better evaluation of the electrical behavior of the cardiac activity should also take into account the next multipole terms, such the quadrupole.

In conclusion, even if Einthoven's triangle is no longer the fundamental configuration in modern electrocardiographic analysis, it can be helpful in the identification of incorrect placement of leads.

References

1. G. Pelosi and S. Selleri, "Michael Faraday and James Clerk Maxwell: The Florentine days," *Il Colle di Galileo*, **9**, 2, 2020, pp. 27-37, https://oajournals.fupress.net/index.php/cdg/article/view/12062.

2. W. J. Turkel, *Spark from the Deep, Baltimora*, The Johns Hopkins University Press, 2013, p. 152.

3. C. Matteucci, "Deuxième Mémoire sur le courant électrique proper de la grenouille et sur celui des animaux à sang chaud," *Annales de Chemie et Physique*, **Ser. III**, 6, 1842, p. 325.

4. C. Matteucci, *Traité des Phénomènes Électro-Physiologiques des Animaux, Parigi, Chez Fortin, Masson et C Libraires, 1844, p. 60.*

5. *A. D. Waller, "A Demonstration on Man of Electromotive Changes Accompanying the Heart's Beat," The Journal of Physiology,* **8**, *5, 1887, pp. 229- 34.*

6. T. Moukabary, "Willem Einthoven (1860-1927): Father of Electrocardiography," *Cardiology Journal*, **14**, 3, 2007, pp. 316-317.

7. W. Einthoven, "Galvanometrische registratie van het menschelijk electrocardiogram," *Herinneringsbudendedl Professor S. S. Rosenstein,* Leiden, Eduard Ijdo, 1902, pp. 101-107.

8. W. Einthoven, "Le TI cardiogramme." *Arch. internat. Physiol.*, **4**, 1906.

9. "Willem Einthoven – Facts," Nobel Media AB 2020, https://www.nobelprize.org/prizes/medicine/1924/einthoven/facts/.

10. H. A. Snellen, *Willem Einthoven (1860-1927): Father of Electrocardiography. Life and Work, Ancestors and Contemporaries*, Dordrecht, Kluwer Academic Publishers, 1995.

An Unexpected Mossotti: His Formula at the Basis of Dielectrophoresis in Modern Molecular Biology

Federico Carpi[1], Stefano Maddio[2], and Benedetta Pelosi[3]

[1]Department of Industrial Engineering
University of Florence
Via di S. Marta, 3 – 50139
Florence, Italy
E-mail: federico.carpi@unifi.it

[2]Department of Information Engineering
University of Florence
Via di S. Marta, 3 – 50139
Florence, Italy
E-mail: stefano.maddio@unifi.it

[3] Department of Molecular Biosciences
The Wenner-Gren Institute
University of Stockholm
SE-106 91 Stockholm
E-mail: benedetta.pelosi@su.se

Abstract

The Clausius-Mossotti formula finds an unexpected application in modern molecular biology: it is in fact the foundation of dielectrophoresis, one of the most widely used chromatographic techniques for isolating biomolecules. In fact, dielectrophoresis overcomes some limitations of electrophoresis, also allowing the analysis and separation of neutral particles, such as individual cells. In this contribution, we briefly retrace some of the significant milestones in the history of dielectrophoresis, starting from its connection with Mossotti's studies.

Biomolecular separation techniques, also called "chromatography," have always been widely applied in the field of clinical analyses, of which they have always been one of the foundations, in order to isolate specific constituents within a heterogeneous sample. As the observation scale moves towards single cells, it is widely recognized how these techniques are increasingly important. A classic method of separating biological components is to exploit their different densities.

Another approach to develop separation techniques is based on the use of electric and magnetic fields. The evolution of these techniques has gone hand in hand with the evolution of knowledge of electrical and magnetic phenomena.

Electrophoresis was the first of these techniques. It is based on the application of a uniform electrostatic field to a sample to be analyzed. Biomolecules having a net charge – for example, due to ionizable groups – migrate within the sample. Based on the charge and mobility – that is, the coefficient that links the speed of a particle to the field to which it is subjected – the electrophoretic technique allows for separating the charged biomolecules. To improve performance, a gelatinous substance (agarose gel) is usually used as a sieve.

This approach is typically used to analyze and separate DNA nucleic acids, hence the great importance of the technique.

The electrophoresis phenomenon was first described in 1807 by Ferdinand Friedrich Reuss [1], who observed the migration of clay particles immersed in water in the presence of an external electric field. However, the first device to implement modern electrophoresis was made in 1937 by the Swedish biochemist Arne Wilhelm Kaurin Tiselius (Stockholm, Sweden, 1902 – Uppsala, Sweden, 1971) [2]. Thanks to his research on electrophoresis, Tiselius won the Nobel Prize in Chemistry in 1948, with the following citation: "for his research on electrophoresis and adsorption analysis, especially for his discoveries concerning the complex nature of the serum proteins."

Figure 1. A commercial apparatus for electrophoresis (from [3]).

Although electrophoresis is a technique that has been known for two centuries and in use for more than a century [4], and is routinely employed in biomedical labs (Figure 1), it has a significant limitation: it cannot be applied to neutral particles, which are instead of increasing interest in modern molecular biology.

This is where the Mossotti formula comes into play. His formula, or rather the Clausius-Mossotti formula, was developed in 1846, but published 1850. If the particle of interest is neutral, but it is at least polarizable, there is still a possibility to exert on it a force similar to the electrophoretic force, ultimately allowing for separations of molecules as in the case of electrophoresis.

To that aim, let us consider a polarizable particle, describable as a uniform sphere of radius *r* and dielectric permittivity ε_p, immersed in a uniform medium of permittivity ε_m. If subjected to an electric field, $\mathbf{e}$, the particle is polarized. The dipole moment, **p**, envisaged by the Clausius-Mossotti formula is as follows:

$$\mathbf{p} = 4\pi\varepsilon_m r^3 K\mathbf{e}$$

$$= 4\pi\varepsilon_m r^3 \frac{\varepsilon_p - \varepsilon_m}{\varepsilon_p + 2\varepsilon_m}\mathbf{e},$$

where the term

$$K = \frac{\varepsilon_p - \varepsilon_m}{\varepsilon_p + 2\varepsilon_m}$$

is known as the Clausus-Mossotti factor. It is therefore sufficient that the electric field, **e**, is nonuniform so that the dipole moment induced on the particle can undergo a non-null force. In fact, an elementary dipole moment is sensitive to the gradient of the square of the electric field,

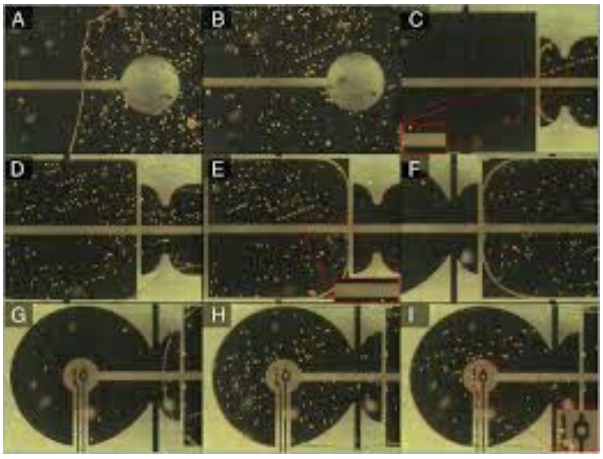

Figure 2. An example of an experimental dielectrophoretic device (from [9]).

$\nabla|\mathbf{e}|^2$. The force generated between the dipole moment and the nonuniform applied field is exerted on the polarized bioparticle of interest. This mechanism is the foundation of "dielectrophoresis," a phenomenon by which a neutral but polarizable particle is subjected to a force when immersed in a nonuniform electric field.

The intensity of the dielectrophoretic force exerted on the biomolecule is therefore dependent on its dielectric properties and on those of the medium. This force also depends on the molecule's size and the configuration of the electric field, in particular, its gradient.

Strictly speaking, the history of dielectrophoresis begins as early as in the 1920s: Hatschek and Thorne had described something similar to the dielectrophoretic mechanism already in 1923 [5], and a patent filed in the United States in 1924 can actually be considered an electrophoretic technique [6].

However, it was Herbert Pohl, a professor at Princeton University and a pioneer of the dielectrophoretic technique in the 1960s, who gave to dielectrophoresis its current form. In 1966, Pohl and Hawk published the first demonstration of electrophoresis on yeast cells. That was the first case where dielectrophoresis was applied to living structures. The apparatus used was very simple. A signal generator was connected to a pair of electrodes in the "point and plane" configuration, that is, one of the two electrodes was needle-like whilst the other one was a classical planar plate. With their rudimentary apparatus, Pohl and Hawk showed that live cells were attracted by the electrodes, whilst dead, non-polarizable cells remained in solution. Pohl called this technique "the natural motion of neutral matter caused by polarization effects in a non-uniform electric field" [7].

However, the new technique was not immediately accepted, and indeed, many of Pohl's later works were refused for publication. Only in 1978, with the publication of his paper, "Dielectrophoresis: The Behavior of Neutral Matter in Nonuniform Electric Fields" [8], did the popularity

of the technique began to grow, although still remaining a niche topic.

Fortunately, a new generation of researchers appeared in the limelight later on, including Ronald Pethig, who was among the protagonists of a further refinement of the technique [9]. Pethig would later become one of the world's greatest experts on the subject [10].

It is interesting to note that in the current form developed by the generation following Pethig, many tricks have been introduced, such as the use of specific gels such agar-agar. Furthermore, various configurations/shapes of the electrodes (Figure 2) have been described [11].

One of the interesting features of the Clausius-Mossotti factor is the fact that it can change according to the actual combination of the particle's and medium's permittivities.

In recent times, the use of a wide range of frequencies has emerged more and more. In fact, depending on the frequency, the Clausius-Mossotti factor can significantly vary, and in particular, the magnitude and sign of the dielectrophoretic force depends on the difference between the polarizability of the particle and of the medium, as is apparent considering the term $\varepsilon_p - \varepsilon_m$ [12].

Using fields characterized by specific frequencies, it is therefore possible to manipulate particles of interest with high selectivity, obtaining very specific effects: cellular filtering with high specificity and without marking, and entrapment and identification of the electrical characteristics of unknown particles. Such results are difficult to obtain with traditional non-electrical chromatographic techniques, and are also even more interesting than the results of classical electrophoresis.

These properties are typically used to identify cancer cells camouflaged between healthy cells, allowing for rapid and minimally invasive diagnoses.

It is worth mentioning that there exists an effect similar to dieletrophoresis for magnetizable molecules, such as some blood constituents. The effect is known as "diamagnetophoresis," as the driving source is a magnetic field. The development of this recent approach allows for directly operating on red blood cells, which are sensitive to the magnetic fields thanks to the susceptibility of hemoglobin [13].

Finally, it is also worth noting that the two techniques can be used in combination. In this case, the technique is referred to as "dielectro-magnetophoresis." This strategy promises to be a harbinger of even more interesting developments in the field of molecular biology.

This is really an unexpected consequence of the work pioneered by Ottaviano Fabrizio Mossotti.

References

1. F. F. Reuss, *Memoires de la Société Imperiale des Naturalistes de Moskou*, **2**, 1809, pp. 327-47.

2. R. A. Kyle and M. A. Shampo, "Arne Tiselius – Father of Electrophoresis," *Mayo Clinic Proceedings*, **80**, 3, 2005, p. 302.

3. http://it.vwr.com/store

4. P. G. Righetti, "Happy Bicentennial, Electrophoresis!," *Journal of Proteomics*, **73**, 2, 2009, pp. 181-187.

5. E. Hatschek and P. C. L. Thorne, "Metal Sols in Non-Dissociating Liquids. I. – Nickel in Toluene and Benzene," *Proc. R. Soc. A*, **103**, 1923, p. 276.

6. H. S. Hatfield, "Means and Process of Separating Substances One from Another," US Patent 1498911A, 1924.

7. H. A. Pohl, "The Motion and Precipitation of Suspensoids in Divergent Electric Fields," *Journal of Applied Physics*, **22**, 7, 1951, pp. 869-871.

8. H. A. Pohl, *Dielectrophoresis: the Behavior of Neutral Matter in Nonuniform Electric Fields*, Cambridge, Cambridge University Press, 1978.

9. J. A. R. Price, J. P. H. Burt, and R. Pethig, "An Optical Technique for Measurement of Cell Dielectrophoresis," *Inst. Phys. Conf. Ser.*, **85**, 1987, pp. 75-79.

10. R. R. Pethig, *Dielectrophoresis: Theory, Methodology and Biological Applications*, New York, John Wiley & Sons, 2017.

11. S. L. Tsai, J. L. Hong, M. K. Chen, L. S. Jang, "Experimental Study of Dielectrophoresis and Liquid Dielectrophoresis Mechanisms for Particle Capture in a Droplet," *Electrophoresis*, **32**, 11, 2011, pp. 1337-1347.

12. N. G. Green and M. Hywel, "Dielectrophoretic Separation of Nano-Particles," *Journal of Physics D: Applied Physics*, 3011, 1997.

13. Z. Maciej, et al., "Red Blood Cell Magnetophoresis," *Biophysical Journal*, **84**, 4, 2003, pp. 2638-2645.

James C. Lin
University of Illinois at Chicago
851 South Morgan Street, M/C 154
Chicago, IL 60607 USA
E-mail: lin@uic.edu

Fighter Pilot Disorientation and Pulsed Microwave Radiation from Radars

The US Defense Advanced Research Projects Agency (DARPA) announced in August 2020 a bidding for submission of innovative research proposals for concepts that would lead to better understanding of the Impact of Cockpit Electro-Magnetics on Aircrew Neurology (ICEMAN: "Iceman" also happens to be the call sign of a fighter pilot portrayed in the movie *Top Gun*). In its request for proposal (RFP) [1], DARPA stated that "Current cockpits are flooded with radiofrequency (RF) noise from on-board emissions, communication links, and navigation electronics, including strong electromagnetics (EM) fields from audio headsets and helmet tracking technologies."

The stated objectives are to determine if the current air-combat cockpit EM environment may impact cognitive performance and/or physiological sensor performance, quantify the effects, and demonstrate potential mitigation strategies.

Military pilots often report cognitive performance challenges during flight operations. Many have reported experiences with spatial disorientation (SD), in which the pilot's perception of aircraft position, motion, altitude, or attitude does not correspond to reality [2-5]. Spatial disorientation has posed a significant problem for military pilots and continues to be a challenge today. These reports indicate that spatial disorientation mishaps occur in fighter/attack aircraft at more than five times the rate of non-fighter/attack, fixed-wing aircraft. Indeed, the rate of spatial-disorientation-related accidents has been estimated to be 11%-12% of military aircraft crashes [3, 4].

The number of spatial-disorientation accidents at night are higher than in daytime. Visual illusions at night because of the degraded visual environment are well documented. During night flights, pilots sometimes confuse ground lights with stars, and unlighted areas of the Earth as night sky.

From 1993 to 2013, spatial disorientation accounted for 72 Class A mishaps, 101 deaths, and 65 aircraft lost in US Air Force pilots [5]. Mishaps are defined as Class A if they result in death or permanent total disability, or destruction of aircraft. It is noteworthy that mishap rates for F-16 fighter/attack aircraft were found to be marginally higher than for other fighter/attack aircraft.

Spatial disorientation may be caused by several human factors, such as the visual, vestibular, and thesomatosensory systems involved in cognitive performance. Aside from potential effects on cognitive functions and human brainwaves already mentioned in the DARPA announcement, there may be potential responses of more abrupt and distractive nature resulting from exposure to high-power pulsed RF and microwave radiation.

The DARPA RFP mentions that the cockpits are flooded with RF signals from onboard emissions, communication links, and navigation electronics, including strong EM fields from audio headsets and helmet-tracking technologies.

It has been hypothesized that the cockpit RF and EM fields, especially the frequencies between 9 kHz and 1 GHz, may influence cognitive performance including spatial disorientation, task saturation, and mis-prioritization. However, RF and EM fields in cockpits are not currently monitored. Little effort has been made to shield pilots from these fields, and the potential impacts of these fields on a pilot's cognition have not been assessed.

It is reasonable to assume that fighter cockpits are subjected to strong impinging RF and/or microwave radar pulses under some operational conditions. Common characteristics of these radar pulses are high peak power (GW), short pulse widths (μs), and fast pulse risetimes (ns). Depending on specific materials and designs of the helmets, the RF and microwave radiation could penetrate and reverberate inside the pilot's helmet and head to generate even higher RF and EM fields inside the pilot's head under these circumstances.

The resulting exposure to high-power pulsed RF radiation and associated microwave energy deposition in head tissues may not produce overt tissue heating, but could elicit sensitive biological responses. The prime examples include microwave-pulse-induced acoustic pressure waves in the head (microwave auditory effect) [6, 7], and the startle reflex and motor-reaction behaviors observed in laboratory animals [8-10]. Indeed, there may be similarities between these pulsed microwave-induced responses. The microwave auditory effect has been implicated in the Cuba sonic attacks on diplomats [7]. However, as discussed below, the microwave power threshold needed for startle reflex and motor reaction is higher than that required to induce the microwave auditory effect. Indeed, the microwave auditory effect may be the cause for the startle reaction resulting from a much louder microwave-induced sound.

It is thus plausible that an unexpected, sudden, and intense auditory stimulus inside the head from a high-power radar could elicit a classic acoustic startle reflex that could cause abrupt changes in a pilot's head position, orientation, or attention.

The startle-reflex and motor-reaction behaviors are innate responses of mammals to an unexpected and sudden occurrence such as intense auditory, visual, or somatosensory (tactile) stimulus that interrupts ongoing behavior, distracts from attentional function, initiates actions, and prepares the individual against a potential threat. Concurrently, it activates a protective stance to prevent injury and may alert the person or animal to instigate evasive behaviors [11, 12].

For 1.25 GHz microwave radar pulses (10 μs, 80 Hz), the threshold for startle reflex was found to be 0.29 kJ/kg. The microwave energy was associated with less than 0.1°C potential rise in the bulk tissue temperature in mice [8]. Clearly, the response is not associated with microwave-induced tissue heating. Furthermore, it has been shown that a single 1.25 GHz microwave pulse (0.8 μs to 1.0 μs) to the head of rats at 22 mJ/kg to 43 mJ/kg per pulse (peak SAR, 23 kW/kg to 48 kW/kg) could modify the acoustic startle response [13]. In another investigation, 1.25 GHz microwave pulses averaging 0.96 μs wide and 35.5 kW/kg to 86.0 kW/kg peak SAR (66.6 mJ/kg to 141.8 mJ/kg of absorbed energy) were reported to modify the startle response in rats [9].

In summary, the ambient RF-EM field levels in a typical fighter/attack aircraft's cockpit are now unclear. Quantitative surveys and measurements are necessary to allow proper assessment of the RF-EM field's potential effects on a pilot's brain activity, neurophysiology, and behavioral responses. Noticeably, the fighter cockpits are subjected to strong impinging RF and/or microwave radar pulses under some operational conditions.

There are two pulsed-microwave-induced auditory responses from humans and mammals when the head is exposed to high-power microwave pulses that could impact a pilot's cognitive performance and response. These are microwave-pulse-induced acoustic pressure waves in the head: the microwave auditory effect and the acoustically induced startle reflex and motor reaction from a sudden, unexpected, and intense auditory stimulus inside the pilot's head. The startle reaction from a sudden unexpected auditory stimulus may cause the pilot to experience spatial disorientation, in which the pilot's perception of aircraft position, motion, altitude, or attitude does not correspond to actuality.

Note that the above supposition is derived from theoretical consideration along with available but limited experimental evidence. The kind of confirming studies that would be useful are neurophysiological and psychophysical investigations of pulsed-microwave-exposed animals including observations of subhuman primate's behavioral and performance responses.

References

1. "STTR Opportunity: Impact of Cockpit Electro-Magnetics on Aircrew Neurology (ICEMAN)," Notice ID HR001120S0019-18, August, 19, 2020, https://beta.sam.gov/opp/45cf0a26208f441db092e9a2653bddd6/view#general.

2. A. Bellenkes, R. Bason, and D. W. Yacavone, "Spatial Disorientation in Naval Aviation Mishaps: A Review of Class A Incidents from 1980 Through 1989," *Aviat. Space Environ. Med.*, **63**, 2, 1992, pp. 128-131.

3. Y. Takada, T. Hisada, N. Kuwada, M. Sakai, and T. Akamatsu, "Survey of Severe Spatial Disorientation Episodes in Japan Air Self-Defense Force Fighter Pilots Showing Increased Severity in Night Flight," *Mil. Med.*, **174**, 6, 2009, pp. 626-630.

4. T. J. Lyons, W. Ercoline, K. O'Toole, and K. Grayson, "Aircraft and Related Factors in Crashes Involving Spatial Disorientation: 15 Years of U.S. Air Force Data," *Aviat. Space Environ. Med.*, **77**, 7, 2006, pp. 720-723.

5. R. J. Poisson III and M. E. Miller, "Spatial Disorientation Mishap Trends in the U.S. Air Force 1993-2013," *Aviat. Space Environ. Med.*, **85**, 9, 2014, pp. 919-924.

6. J. C. Lin and Z. W. Wang, "Hearing of Microwave Pulses by Humans and Animals: Effects, Mechanism, and Thresholds," *Health Physics*, **92**, 6, 2007, pp. 621-628.

7. J. C. Lin, "Strange Reports of Weaponized Sound in Cuba," *IEEE Microwave Magazine*, **19**, 1, 2018, pp. 18-19.

8. D. O. Brown, S. T. Lu, and E. C. Elson, "Characteristics of Microwave Evoked Body Movements in Mice," *Bioelectromagnetics*, **15**, 1994, pp. 143-161.

9. R. L. Seaman, D. A. Beblo, and T. G. Raslear, "Modification of Acoustic and Tactile Startle by Single Microwave Pulses," *Physiol. Behav.*, **55**, 3, 1994, pp. 587-595.

10. S. T. Lu and J. O. DeLorge, "Biological Effects of High Peak Power Radiofrequency Pulses," in J. Lin (ed.) *Advances in Electromagnetic Fields in Living Systems*, New York, Kluwer Academic/Plenum Publishers, 2000, pp. 207-264.

11. R. Gómez-Nieto, S. Hormigo, and D. E. López, "Prepulse Inhibition of the Auditory Startle Reflex Assessment as a Hallmark of Brainstem Sensorimotor Gating Mechanisms, *Brain Sci.*, **10**, 2020, pp. 639-654.

12. M. Fleshler, "Adequate Acoustic Stimulus for Startle Reaction in the Rat," *J. Comp. Physiol. Psychol.*, **60**, 1965, pp. 200-207.

13. R. L. Seaman and D. A. Beblo, "Modification of Acoustic Startle by Microwave Pulses in the Rat: A Preliminary Report, *Bioelectromagnetics*, **13**, 4, 1992, pp. 323-328.

European School of Antennas 2021

ESoA Board

ESoA Coordinator Prof. Stefano Maci
Dept. of Information Engineering and Mathematics
University of Siena, 53100 - Siena (Italy)
E-mail: macis@ing.unisi.it

www.esoa-web.org

http://www.facebook.com/europeanschoolofantennas

MICROWAVE IMAGING AND DIAGNOSTICS,
UMED-UNITN, Naples, February 1-5
Coordinators: A. Massa, T. Isernia, L. Crocco

ALL DIGITAL RADAR SYSTEM ENGINEERING,
KIT- Karlsruhe March 16-19, 2021
Coordinators: T. Zwick, M. Younis

COMPRESSIVE SENSING AS APPLIED TO ELECTROMAGNETICS
UNITN, Riva del Garda, March 22-26
Coordinators: A. Massa, G. Oliveri

LEAKY WAVES AND PERIODIC STRUCTURES FOR ANTENNA APPLICATIONS,
La Sapienza, Rome April 26-30 2021
Coordinator: F. Frezza

ADVANCED MATHEMATICS FOR ANTENNA ANALYSIS,
UNIZG Dubrovnik, 17-21 May
Coordinators: Z. Sipus, S. Maci

CHARACTERISTIC MODES: THEORY AND APPLICATIONS,
CTU, Prague 24-28 May,
Coordinators: M. Ferrando, P Hazdra

COMPACT ANTENNAS FOR SENSOR SYSTEMS, UPC – Barcelona, May 31-June 4, Coordinators : L. Jofre, A. Skrivervik

MOBILE RADIO PROPAGATION FOR 5G AND BEYOND
UNIBO, Cesenatico, June 7-11
Coordinators: , V. Degli Esposti, C. Oestges,T. Kürner

ANTENNA MEASUREMENTS,
UPM-MVG, Madrid, 14-18 June
Coordinators: M. Sierra, L. Foged

TERAHERTZ ANTENNA AND IMAGING SYSTEMS TuDelft – Delft, 21-25 June,
Coordinators : A. Neto, N. Llombart . L. Jofre,

MILLIMETER WAVE ANTENNAS,
UR1 - Rennes, 28 June - 2 July
Coordinator: O. Lafond

Exploiting Symmetries in Artificial Materials for Antenna Applications
La Sorbonne, Paris, 13-16 September
G Valerio, E Martini, O Quevedo

ADVANCED COMPUTATIONAL EM,
POLITO, Torino, 20-24 September
Coordinators: F. Andriulli, G. Vecchi

ANTENNA SYNTHESIS,
UNINA, Capri, 11-15 October
Coordinator: A. Capozzoli

ACTIVE ANTENNAS
ESA-ESTEC , Nordwijk , 4-8 October
Coordinator: G. Toso, P. Angeletti

DISRUPTIVE ANTENNAS BASED ON EMERGING TECHNOLOGIES FOR NOVEL SATELLITE TELECOMMUNICATION SCHEME (REVOLVE)
TAS, Rennes, November 15-19
Coordinators: M. Ettorre, H. Legay

Asta Pellinen-Wannberg
Umeå University, Department of Physics and
Swedish Institute of Space Physics
S-90187 Umeå, Sweden
Tel: +46 90 786 7492
E-mail: asta.pellinen-wannberg@umu.se

Introduction from the Associate Editor

It must have been in the late 1980s that I heard for the first time from my colleagues at the Swedish Institute of Space Physics about an extremely smart and competent Russian female plasma physicist with whom everybody wanted to collaborate. Her name was Nataly Blagoveshchenskaya and she was from Leningrad. I met sympathetic Nataly for the first time at the 12th EISCAT International Workshop that we organized in Kiruna in 2005. I especially remember the discussions we had in the sauna, to which I invited all the participating female scientists after the meeting. We were sweating inside the dark sauna on the high benches, hitting ourselves with the soft birch whisks, meanwhile dipping in the cold lake, and then sitting outside in a wooden-fired hot tub admiring the twilight sun for hours. All these rituals were very familiar for Nataly from the banya at her own dacha, outside Sankt Petersburg.

Nataly had a broad experience and unique knowledge of the stimulated plasma processes that she had acquired from the SURA Heating facility in Nizhnii Novgorod. In Nataly the profound theoretical plasma physics competence is united with the ability to do controlled experiments and interpret results from such experiments in our largest plasma laboratory – even though all-the-time variable – the ionosphere. We are greatly thankful for all the results she has contributed to with the work at the EISCAT Heating facility in Northern Scandinavia. A review paper on her scientific work on features in the artificially perturbed ionosphere appears in this issue.

Reflections on a Career in Radio Science

Nataly Blagoveshchenskaya

Arctic and Antarctic Research Institute
Bering 38 str., 199397 St. Petersburg
Russian Federation
Tel: +7 812 337 3191
E-mail: nataly@aari.nw.ru

My way into radio science started in the 1970s at the Polar Space Physic Observatory (PSPO) in Norilsk, a town in northern Siberia beyond the Arctic Circle. After graduating from the Electrotechnical University of Communication in Sankt Petersburg (at that time, Leningrad), I took a position as a junior researcher at the PSPO. I actually followed my husband, Dr. Donat Blagoveshchensky, to Norilsk. He was invited to the PSPO to lead the newly organized radio wave propagation group. At that time, a brilliant and enthusiastic young scientist, Dr. Gelii Zherebtsov, was the head of the PSPO. He organized and led the scientific research in various fields, including the ionosphere, the Earth's magnetic field, visible aurora, and radio wave propagation. The PSPO was a division

of the Institute of Solar Terrestrial Physics, ISTP (former Institute of Earth Magnetism, Ionosphere, and Radio Wave Propagation) of the Siberian Branch of the Russian Academy of Sciences (SB RAS) in Irkutsk. Dr. Zherebtsov later became the Director of ISTP.

I have been fortunate in my career. In the 1970s, my main scientific interest was the propagation of HF radio waves at high latitudes. The main attention was focused on the features and behavior of the HF radio signals depending on the length and the orientation of the radio path, the operating frequency, and the geophysical conditions. Gelii Zherebtsov was my supervisor. My first large conference was the All Russian Conference of radio wave propagation, which was held in 1978 at the Tomsk State University. I defended my PhD thesis in radio physics at the same university in 1979.

From the 1980s, my scientific interest moved to a new field, ionospheric modification by powerful HF radio waves. The heating facility SURA had recently been built in Nizhnii Novgorod (in that time, Gorkii). I was involved in the SURA experiments and was greatly impressed by them. At that time, we returned to Leningrad, and I started to work at the Department of Geophysics at the Arctic and Antarctic Research Institute (AARI) as a senior scientist.

The early 1990s was a hard time for Russian science. We lost many scientists, but managed to maintain the core of our department at AARI. At the same time, the scientists had a new opportunity to join international collaborations, have personal contacts with foreign scientists, and attend conferences and meetings abroad. My first conferences abroad were the COSPAR meeting in Hamburg in 1994, the Heating seminar in Tromsø in 1994, and the EISCAT Workshop in Corsica in 1995. These conferences came to play a key role in my further research, closely related with the EISCAT Scientific Association for the coming 25 years.

Starting out the investigations at EISCAT, I found that there was a lot of potential to improve the use of the HF Heating facility to study the ionosphere-magnetosphere interactions, and I was able to contribute to that field. Studies were carried out at the EISCAT Heating facility (Tromsø, Norway) in the collaboration and with the help of funding support from the Uppsala Division of the Swedish Institute of Space Physics (Prof. Bo Thidé), the Tromsø University (Prof. Asgeir Brekke), and various grants from EISCAT, INTAS, RFBR (Russian Foundation for Basic Research), etc. In the framework of these investigations, it was found that a controlled injection of powerful HF radio waves from the ground into the nightside auroral ionosphere towards the magnetic-field line can produce a modification of the ionosphere-magnetosphere coupling, a generation of the local field-aligned current system, and can trigger local auroral activation. With warm feelings, I remember fruitful discussions and collaboration with Bo Thidé, A. Brekke, M. Rietveld, and M. Kosch regarding the results obtained and newly planned experiments. I received the DSci (the highest Russian scientific degree, corresponding to Research Professor) in Space Physics at the Sankt Petersburg State University in 2002.

My activity at EISCAT was greatly intensified in the 2000s. After more than 10 years of collaboration with the EISCAT facility, I worked hard at getting an agreement between the EISCAT Scientific Association and the Arctic and Antarctic Research Institute (AARI). In 2008, the agreement was signed. That allowed Russia to become an associate member of the EISCAT on the basis of the AARI. Scientists from AARI got the possibility of carrying out regular experiments (two campaigns per year) at EISCAT. A large number of various EISCAT/Heating experiments were carried out from 2009 to 2016. In the course of these experiments, it was found for the first time that extraordinary-polarized powerful HF radio waves radiated into the F region towards the magnetic field are able to generate extremely strong artificial ionospheric disturbances. Their features and conditions of excitation were investigated. In this step, I am greatly thankful to Prof. T. Yeoman (Leicester University, UK) for support by the CUTLASS radar observations in the course of our EISCAT experiments, and Dr. I. Häggström for help in the spectral processing of the EISCAT UHF incoherent-scatter measurements.

How should I summarize my career after many years in science? I have been happy to do research in fields that are extremely important and interesting for me. I have been lucky to work at the Department of Geophysics at the AARI for more than 30 years with Prof. Oleg Troshichev, who was the Head of Department from 1983 up to 2018. I have been happy to work with clever scientists from my laboratory who have supported me during many years. Actually, we are a team carrying out successful scientific research related to the modification of the high-latitude ionosphere by powerful HF radio waves. I am thankful to my team members, especially to Dr. T. D. Borisova, Dr. A. S. Kalishin, D. D. Rogov, and V. A. Kornienko. Since I became the Head of the Laboratory, I have been able to give several young scientists a chance to try research as a lifestyle. I have been able to attend geographically distributed scientific meetings, workshops, and conferences, kept contact with my colleagues abroad, and to live and work in St. Petersburg, which is the most beautiful city in Russia.

Report on Italian URSI Annual Meeting 2019 and IEEE RFID-TA 2019

The annual meeting of the Italian URSI Committee was held September 26, 2019, in Pisa, Italy. The event was organized during the 10th edition of the IEEE RFID Technology and Application (IEEE RFID-TA 2019), a flagship conference in the area of RFID, which provides a platform to share research and experience in wide aspects of RFID technology and applications.

IEEE RFID-TA 2019 Conference

The focus of the 10th edition of the IEEE RFID-TA conference was on reinforcing the collaboration between industry and academia for developing future RFID systems. The Conference venue, "Le Benedettine," was located in a very suggestive and peaceful context, near the church of S. Paolo a Ripa d'Arno, overlooking the Arno river in downtown Pisa. It is an old monastery of S. Benedetto that originally arose in the early twelfth century on the Pisan coast as a hermit community.

Figure 1. The Leaning Tower through a fish-bowl.

The city of Pisa is located near the Tyrrhenian Sea (11 km) in northwestern Tuscany, along the banks of the Arno river, and approximately 80 km west of Florence. Known worldwide for the extraordinary monument of the Leaning Tower (Figure 1), Pisa is a place of artistic treasures, with a heritage of millenary history the point of highest splendor of which that dates back to the age of the Maritime Republics (12th century). Visitors to this eminent university city discover not only art, culture, and history, but also an evocative environment (natural parks, seacoast, and mountains), folklore, excellent restaurants, and fancy shops.

Numbers

124 papers were submitted to the conference by researchers coming from 35 different countries. Among these, 108 papers were accepted and included in the conference proceedings, which corresponded to an acceptance rate of 87%. Such a great result was possible thanks to the hard work of 27 session organizers, who convened 13 special sessions, inviting experts in the fields of novel antenna design, localization systems, sensing, biomedical applications, wireless power transfer and energy harvesting, and RFID emerging applications. Each paper was reviewed by at least two members of the Technical Program Committee, composed by more than 50 esteemed researchers and experts in the RFID sector.

The Conference Program

The program of IEEE RFID-TA 2019 was tight but lively, and some novelties were introduced to make the event more attractive for both academia and industry representatives. In the first day, a workshop, entitled "News from the RFID Industry," was scheduled before the opening ceremony. This gave the participants the opportunity to meet industrial exponents and share their vision on the future of RFID technology. In particular, RFID experts presented their activities and projects in which RFID represented a key enabling technology.

A special session dedicated to "RFID for the Made in Italy" was organized in the same day. In the special session, well-known Italian brands discussed RFID applications in the vinery, fashion, and food sectors (Valentino S.p.A., Ca' del Bosco, ID-Solutions s.r.l.). During the other two days, thirteen special and regular sessions were scheduled. Among others, the first edition of the session entitled "RFID Ladies: Spotlight on Recent Scientific and Industrial Advances of Women in Engineering" was organized, aimed

Figure 2. Dr. Angelo De Santis during the presentation of his tutorial.

to pay homage to the female contribution that was from the very beginning one of the most distinctive features of the RFID community.

Keynote Speakers

Two outstanding Keynote speakers delivered a plenary talk during the second and third days of the conference. The keynote speech of Prof. Smail Tedjini was organized in collaboration with the Italian National Committee of URSI.

In particular, on September 26, 2019, Prof. Smail Tedjini (Université Grenoble Alpes, Grenoble-iNP/LCIS Lab, Valence, France) gave a talk entitled "Advances in RFIDs" focusing on recent development of such technology.

On the following day, Prof. Nuno Borges Carvalho (University of Aveiro, Aveiro, Portugal) presented a talk entitled "A Wireless World Without Batteries," discussing future wireless paradigms that will be changing soon with 5G and beyond.

Awards

Competitions for the Best Paper Award and the Best Student Paper Award were also organized. The list of awardees was as follows:

Figure 3. Dr. Lorenzo Crocco during the presentation of his tutorial.

Best Paper Award

Alice Buffi, Bernardo Tellini, Andrea Motroni, and Paolo Nepa, "A Phase-Based Method for UHF RFID Gate Access Control"

Best Paper Award – Honorary Mention

Davide Dardari, Nicolò Decarli, Davide Fabbri, Anna Guerra, Marco Fantuzzi, Diego Masotti, Alessandra Costanzo, Aldo Romani, Maxime Drouguet, Thomas Feuillen, Christophe Craeye, Christophe Raucy, and Luc Vanderdorpe, "An Ultra-Wideband Batteryless Positioning System for Space Applications"

Ferran Paredes, Cristian Herrojo, and Ferran Martìn, "An Approach for Synchronous Reading of Near-Field Chipless-RFID Tags"

Best Student Paper Competition

First Place: **Sai Nithin Reddy Kantareddy**, Yongbin Sun, and Rahul Bhattacharyya, "Learning Gestures Using a Passive Data Glove with RFID Tags"

Second Place: **Rui Chen**, Shuai Yang, Ajeck M. Ndifon, Ian White, Richard Penty, and Michael J. Crisp, "Beam Scanning UHF RFID Reader Antenna with High Gain and Wide Axial Ratio Beamwidth"

Third Place: **Andrea Motroni**, Paolo Nepa, Alice Buffi and Bernardo Tellini, "A Phase-Based Method for Mobile Node Localization Through UHF-RFID Passive Tags"

Italian URSI Committee Annual Meeting

The Italian National URSI Committee Meeting was organized in parallel with the IEEE RFID-TA Conference on September 26, 2019. It was attended by more than thirty researchers working in universities and research institutes.

The meeting offered a joint plenary session co-organized with the parallel conference IEEE RFID-TA, and an URSI special session with two tutorials exemplifying scientific activities in the framework of two specific URSI Commissions. Moreover, another URSI session was organized as the finale of the 2019 Best Paper Young Scientist Award, delivered by the URSI Italian National Committee. The finale was centered on the presentations of the selected three best papers submitted to the Italian URSI National Committee 2019 Best Paper Young Scientist Award.

The joint plenary session with the IEEE RFID-TA Conference was delivered by Prof. Smail Tedjini, Université Grenoble Alpes, Grenoble-iNP/LCIS Laboratory, Valence, France. This joint plenary session was chaired by Prof. Paolo Nepa (University of Pisa), General Chair of IEEE RFID-TA, and by Prof. Giuliano Manara (University of Pisa), Chair of the IEEE RFID-TA Technical Program Committee and Member of the Italian URSI National Committee.

The URSI Special Session, composed of a couple of tutorials contributed by two specific URSI Commissions, was chaired by Prof. Carlo Carobbi (University of Florence), Secretary of the URSI Italian Committee, which briefly illustrated URSI activities in Italy and worldwide as an introduction to the session. The first tutorial was a contribution from Commission G (Ionospheric Radio and Propagation), titled "Pre-Earthquake Signatures in Ionosphere as Detected by Swarm Satellites." The tutorial was presented by Dr. Angelo De Santis (Istituto Nazionale di Geofisica e Vulcanologia, Italy). The presentation described electron density and magnetic data observed by a swarm of three satellites for almost five years after their launch. The objective was to look for possible earthquake-related ionospheric anomalies. These anomalies were statistically defined and their search was undertaken in the whole space-time interval of interest, avoiding high magnetic latitudes ($|\text{geomagnetic latitude}| \leq 50°$) and geospatially disturbed periods. A worldwide statistical correlation analysis with earthquakes by means of a superposed epoch approach was then performed, finding a few clear concentrations of satellite-data anomalies some days before the occurrences of earthquakes. In order to assess the robustness of the results obtained from observations, the latter results were compared with those obtained from other analyses with random anomalies. In general, our results pointed to a significant statistical correlation of both the electron density and the magnetic-field signal with earthquakes, much above random chance, supporting a lithosphere-atmosphere-ionosphere coupling during the preparation phase of earthquakes. Performing the analysis for different ranges of magnitude, the Rikitake empirical law between ionospheric-anomaly precursor time and earthquake magnitude was confirmed. Finally, this relationship in terms of a diffusion process in the lithosphere was explained.

The second tutorial was a contribution from Commission K (Electromagnetics in Biology and Medicine). The title of the presentation was "A Portable Microwave Imaging Device for Brain Stroke Monitoring." It was given by Dr. Lorenzo Crocco (Istituto per il Rilevamento Elettromagnetico dell'Ambiente, CNR-IREA, Italy). Brain stroke is one of the most common cerebrovascular diseases, with an incidence of about 15 million cases every year worldwide, causing death or permanent injuries. A brain stroke can be either ischemic or hemorrhagic, and the required treatment is completely different depending on the kind of disease. As such, diagnostic imaging methodologies are necessary to support clinicians and to monitor the effectiveness of the therapy. Currently adopted

modalities are magnetic resonance imaging (MRI) and X-ray computerized tomography (CT). They have greatly contributed to the mitigation of brain-stroke effects and social impact. Nevertheless, there is still an interest in developing new modalities, because MRI and CT are not viable for addressing emerging clinical requirements such as early diagnosis (possibly in the ambulance) and continuous bedside monitoring in the post-acute stage. In such a framework, microwave imaging (MWI) may represent an interesting alternative, due to being low cost, not harmful in nature, and its portability. This presentation reviewed the recent efforts carried out by the author and his colleagues in the development of an innovative microwave imaging device properly designed for brain-stroke monitoring with the requirement of making the system architecture as simple as possible. The talk described the overall development, from the design stage to the realization of the system components and the prototype, as well as the initial controlled experiments demonstrating the device capabilities.

The three finalists of the Italian URSI National Committee 2019 Young Scientist Best Paper Award presented their papers on September 26, 2019, during the Italian URSI Annual Meeting. The judging committee was composed of Dr. Giorgiana De Franceschi (URSI Commission G), Dr. Simonetta Paloscia (URSI Commission F), Prof. Giuliano Manara (URSI Commission B), and Prof. Carlo Carobbi (URSI Commission E).

In particular, the 2019 Italian URSI Committee Young Scientist Best Paper Award was assigned to Dr. Valentina Palazzi (University of Perugia), for the paper "Phase-Controlled Beamforming Network Intended for Conformal Arrays." Honorary mentions were given to the other two finalists: Dr. Giuseppe Torrisi, for the paper "RF Design and Experimental Test for a Quadrupole-Free X-Band TM01 Mode Launcher," and Dr. Davide Comite, for the paper "Electromagnetic Modeling of Scattered Signals of Opportunity."

All of the participants, including those registered in the parallel conference (2019 IEEE RFID-TA), strongly appreciated the variety of topics and applications presented at the Italian URSI National Meeting, and in particular the distinctive feature of URSI, its organization into ten scientific Commissions, and its special consideration for Young Scientist activities.

Roberto Sorrentino (deceased)
President of the Italian National Committee of URSI

Carlo Carobbi
Secretary of URSI Italian Committee
E-mail: carlo.carobbi@unifi.it

Giuliano Manara
URSI representative at IEEE RFID-TA 2019
and IEEE RFID-TA 2019 TPC Chair
E-mail: giuliano.manara@unipi.it

Andrea Michel
URSI Commission B ECR
and IEEE RFID-TA 2019 TPC Vice-Chair
E-mail: giuliano.manara@unipi.it

Paolo Nepa
IEEE RFID-TA General Chair
E-mail: paolo.nepa@unipi.it

URSI Conference Calendar

A detailed list of meetings is available on the URSI website at http://www.ursi.org/events.php

January 2021

USNC-URSI NRSM 2021
USNC-URSI National Radio Science Meeting
Virtual meeting on 4-9 January 2021
Contact: Dr. Sembiam R. Rengarajan, Department of ECE, California State University, Northridge, CA 91330-8346, USA, Fax: 818-677-7062, E-mail: srengarajan@csun.ed u; Logistics: Christina Patarino, E-mail: christina.patarino@colorado.edu, Fax: 303-492-5959, Website: https://www.nrsmboulder.org/

EuMW 2021
European Microwave Week 2020
Utrecht, the Netherlands, 10-15 January 2021
Contact: E-mail: headquarters@eumwa.org, https://www.eumweek.com/

ISAP 2021
International Symposium on Antennas and Propagation
Osaka, Japan, 25-28 January 2021
Contact : Prof. Hiroyuki Arai: General Chair of ISAP 2020 Yokohama National University, Japan, ap_ac-isap2020@mail.ieice.org, Website: http://isap2020.org/

COSPAR 2021
43rd Scientific Assembly of the Committee on Space Research (COSPAR) and Associated Events
Sydney, Australia, 28 January – 4 February 2021
Contact : COSPAR Secretariat, 2 place Maurice Quentin, 75039 Paris Cedex 01, France, Tel: +33 1 44 76 75 10, Fax: +33 1 44 76 74 37, E-mail: cospar@cosparhq.cnes.fr http://www.cospar2021.org March

March 2021

EuCAP 2021
15th European Conference on Antennas and Propagation
Düsseldorf, Germany, 22 - 26 March 2021
Contact : Thomas Kürner, info@eucap2021.org, Website: https://www.eucap.org/conference/news-23092019

August 2021

URSI GASS 2021
Rome, Italy, August 28 -September 4, 2021
Contact: URSI Secretariat, Ghent University – INTEC, Technologiepark-Zwijnaarde 126, B-9052 Gent, Belgium, E-mail gass@ursi.org, Website: http://www.ursi2021.org/

October 2021

ISAP 2021
International Symposium on Antennas and Propagation
Taipei, Taiwan, 19-22 October 2021
Contact : http://www.isap2021.org/

May 2022

AT-RASC 2022
Third URSI Atlantic Radio Science Conference
Gran Canaria, Spain, 30 May - 4 June 2022
Contact: Prof. Peter Van Daele, URSI Secretariat, Ghent University – INTEC, Technologiepark-Zwijnaarde 126, B-9052 Gent, Belgium, E-mail: peter.vandaele@ugent.be http://www.at-rasc.com

August 2022

AP-RASC 2022
Asia-Pacific Radio Science Conference 2022
Sydney, Australia, 21-25 August 2022
Contact: URSI Secretariat, Ghent University – INTEC, Technologiepark-Zwijnaarde 126, B-9052 Gent, Belgium, E-mail: info@ursi.org

Information for Authors

Content

The *Radio Science Bulletin* is published four times per year by the Radio Science Press on behalf of URSI, the International Union of Radio Science. The content of the *Bulletin* falls into three categories: peer-reviewed scientific papers, correspondence items (short technical notes, letters to the editor, reports on meetings, and reviews), and general and administrative information issued by the URSI Secretariat. Scientific papers may be invited (such as papers in the *Reviews of Radio Science* series, from the Commissions of URSI) or contributed. Papers may include original contributions, but should preferably also be of a sufficiently tutorial or review nature to be of interest to a wide range of radio scientists. The *Radio Science Bulletin* is indexed and abstracted by INSPEC.

Scientific papers are subjected to peer review. The content should be original and should not duplicate information or material that has been previously published (if use is made of previously published material, this must be identified to the Editor at the time of submission). Submission of a manuscript constitutes an implicit statement by the author(s) that it has not been submitted, accepted for publication, published, or copyrighted elsewhere, unless stated differently by the author(s) at time of submission. Accepted material will not be returned unless requested by the author(s) at time of submission.

Submissions

Material submitted for publication in the scientific section of the *Bulletin* should be addressed to the Editor, whereas administrative material is handled directly with the Secretariat. Submission in electronic format according to the instructions below is preferred. There are typically no page charges for contributions following the guidelines. No free reprints are provided.

Style and Format

There are no set limits on the length of papers, but they typically range from three to 15 published pages including figures. The official languages of URSI are French and English: contributions in either language are acceptable. No specific style for the manuscript is required as the final layout of the material is done by the URSI Secretariat. Manuscripts should generally be prepared in one column for printing on one side of the paper, with as little use of automatic formatting features of word processors as possible. A complete style guide for the *Reviews of Radio Science* can be downloaded from http://www.ips.gov.au/IPSHosted/NCRS/reviews/. The style instructions in this can be followed for all other *Bulletin* contributions, as well. The name, affiliation, address, telephone and fax numbers, and e-mail address for all authors must be included with

All papers accepted for publication are subject to editing to provide uniformity of style and clarity of language. The publication schedule does not usually permit providing galleys to the author.

Figure captions should be on a separate page in proper style; see the above guide or any issue for examples. All lettering on figures must be of sufficient size to be at least 9 pt in size after reduction to column width. Each illustration should be identified on the back or at the bottom of the sheet with the figure number and name of author(s). If possible, the figures should also be provided in electronic format. TIF is preferred, although other formats are possible as well: please contact the Editor. Electronic versions of figures *must* be of sufficient resolution to permit good quality in print. As a rough guideline, when sized to column width, line art should have a minimum resolution of 300 dpi; color photographs should have a minimum resolution of 150 dpi with a color depth of 24 bits. 72 dpi images intended for the Web are generally *not* acceptable. Contact the Editor for further information.

Electronic Submission

A version of Microsoft *Word* is the preferred format for submissions. Submissions in versions of T_EX can be accepted in some circumstances: please contact the Editor before submitting. *A paper copy of all electronic submissions must be mailed to the Editor, including originals of all figures.* Please do *not* include figures in the same file as the text of a contribution. Electronic files can be send to the Editor in three ways: (1) By sending a floppy diskette or CD-R; (2) By attachment to an e-mail message to the Editor (the maximum size for attachments *after* MIME encoding is about 7 MB); (3) By e-mailing the Editor instructions for downloading the material from an ftp site.

Review Process

The review process usually requires about three months. Authors may be asked to modify the manuscript if it is not accepted in its original form. The elapsed time between receipt of a manuscript and publication is usually less than twelve months.

Copyright

Submission of a contribution to the *Radio Science Bulletin* will be interpreted as assignment and release of copyright and any and all other rights to the Radio Science Press, acting as agent and trustee for URSI. Submission for publication implicitly indicates the author(s) agreement with such assignment, and certification that publication will not violate any other copyrights or other rights associated with the submitted material.

Become An Individual Member of URSI

The URSI Board of Officers is pleased to announce the establishment of categories of individual membership of URSI. The purpose of individual membership of URSI is to secure professional recognition of individual radio scientists and to establish their better connection with the URSI Board of Officers, Scientific Commissions, and URSI Member Committees. Three categories of individual membership (URSI Corresponding Member, URSI Senior Member and URSI Fellow) have been established.

URSI Corresponding Membership is the first step into the URSI community and provides:

- Access to the proceedings of URSI Flagship Conferences via the Web site
- Notifications of new editions of URSI publications.

In addition, URSI Senior Members and URSI Fellows benefit from the following:

- Reduced registration fees at URSI Flagship Meetings.
- Reduced registration fees at some meetings organized by partnering organizations such as (but not limited to) IEEE AP-S and EuCAP.
- A page charge reduction from 175 USD to 150 USD for papers published in the URSI journal, *Radio Science Letters*.
- An invitation to receive their individual membership certificate at an URSI Flagship meeting.

Fellowship is by invitation only; Senior Membership can be by invitation or application. Corresponding Membership is a streamlined, instant process. Details, and an online application for URSI Senior Membership, are available at http://www.ursi.org/membership.php#tab-sectionA1.